

Distribution of Sea Ice Thickness in the Beaufort Sea

R.O. RAMSEIER, M.R. VANT, L.D. ARSENAULT,
L. GRAY, R.B. GRAY and W.J. CHUDOBIAK

Technical Report No. 30

✓
2



DISTRIBUTION OF THE ICE THICKNESS
IN THE BEAUFORT SEA

Rene O. Ramseier, Malcolm R. Vant and Lyn D. Arsenault

Ocean and Aquatic Sciences
Department of the Environment
580 Booth Street
Ottawa, Ontario K1A 0H3

Lawrence Gray
Department of Energy, Mines & Resources
Canada Centre for Remote Sensing

Robert B. Gray
Department of Communications
Communications Research Centre

Walter J. Chudobiak
Carleton University, Department of Electronics
Applied Instrumentation Laboratory

Beaufort Sea Technical Report #30

Beaufort Sea Project
Dept. of the Environment
512 Federal Building
1230 Government St.
Victoria, B.C. V8W 1Y4

December 1975

CONTENTS

	Page
1. SUMMARY	1
2. INTRODUCTION.....	1
3. RESUMÉ OF CURRENT STATE OF KNOWLEDGE	
3.1 Dielectric Properties of Sea Ice	2
3.2 Radar Probes	4
3.3 Scatterometer	5
3.4 Active Microwave Mapping	5
3.5 Passive Microwave Mapping	6
3.6 Ice Type Distribution in the Beaufort Sea	7
4. STUDY AREAS	
4.1 Offshore Program	8
4.2 Arctic Ice Dynamics Joint Experiment Site	8
4.3 Beaufort Sea.....	8
5. METHODS AND SOURCES OF DATA	
5.1 Dielectric Measurements.....	8
5.2 UHF Impulse Radar	9
5.3 Scatterometer	10
5.4 Side-Looking Radar	12
5.5 Electronically-Scanned Microwave Radiometer	13
6. RESULTS	
6.1 Dielectric Properties of Sea Ice	14
6.2 Active and Passive Microwave Mapping.....	14
6.2.1 Scatterometer results	14
6.2.2 Side-Looking Radar results	18
6.2.3 Electronically-Scanned Microwave Radiometer Results	19
7. CONCLUSIONS AND RECOMMENDATIONS.....	21
8. ACKNOWLEDGEMENTS.....	23
9. GLOSSARY	23
10. REFERENCES.....	24

11.	FIGURE CAPTIONS.....	28
12.	APPENDIX	72

1. SUMMARY

Although it was not possible to measure sea ice thickness directly, monthly maps indicating the distribution of first-year and multiyear ice for the entire Beaufort Sea region were prepared from Nimbus 5 passive microwave imagery. Detailed investigation of the shear zone was performed using 13.4 GHz scatterometer and X-band SLR imagery for April 1975. A description of the various sensors employed and an outline of the development of a UHF radar for direct measurement of sea ice thickness are included.

2. INTRODUCTION

The purpose of this study was to obtain ice thickness distribution in the Beaufort Sea. To achieve this goal direct and indirect methods were required, such as measuring the ice thickness directly by UHF radar or inferring the ice thickness from surface or near-surface data. Because of the large area under study and the general nature of the problem, remote sensing techniques offer the only means of obtaining the necessary data. Of the remote sensing techniques available, microwave sensors (both of the active and passive type) were used to generate the bulk of the data.

The study has two objectives:

- a) to overfly a predetermined grid to obtain ice thickness data using a yet-to-be-developed UHF impulse radar, and
- b) to map the distribution of ice types and open water with the use of satellite and aircraft remote sensing data.

The first objective was not fully achieved. However, a UHF impulse radar has been built which has the potential for measuring the transit time of the impulse through ice. From these measurements, based on the understanding of the dielectric properties, an ice thickness can be determined. A great effort is still necessary to design an airborne system which can be used for mapping ice thickness.

The second objective was accomplished using passive microwave data obtained from the NIMBUS 5 satellite. Monthly maps showing the relative distribution of ice types and open water were prepared. In addition active remote sensor data from an X-band SLR (Side-Looking Radar), and a 13.4 GHz scatterometer was used to identify detailed ice features in the shear zone of the Beaufort Sea.

Because of the magnitude of this program, the number of agencies participating, the dependence on field work in the Beaufort Sea, as well as the severe time constraint, the data presented here has not yet been analyzed to its fullest potential.

3. RESUMÉ OF CURRENT STATE OF KNOWLEDGE

3.1 Dielectric Properties of Sea Ice

An accurate knowledge of the dielectric properties of sea ice forms the basis for any measurement of sea ice thickness using microwave techniques. It is important to know the dielectric constant (ϵ') to determine transit time or the velocity of propagation through the ice, so that the transit time measurements obtained with a pulsed radar can be converted to range measurements. It is equally important to know the dielectric loss (ϵ'') in the medium under investigation. The dielectric loss determines the absorption of power and thus can be used to predict the maximum possible penetration through the ice of a given radar system.

It was both for these reasons and in support of other microwave remote sensing missions, that a study program of dielectric measurements of sea ice was included as part of the Beaufort Sea Project.

The study was composed of two phases. Phase one consisted of a literature survey of previous dielectric measurements over the frequency range of interest. Phase two consisted of a dielectric measurement program over the frequency range 100 MHz - 8 GHz, which was directed towards obtaining empirical models for sea ice dielectric behaviour.

Table 1 presents a comprehensive survey of all the dielectric measurements performed on sea ice, both natural and a laboratory prepared facsimile. Most of the measurements cited have been done at only a few individual frequencies and selected salinities and temperatures, so that a complete overview of the properties of sea ice does not exist. Certain results should be treated with caution since they were not performed on natural sea ice, but only on laboratory artifacts of sea ice. Included in this category is the work of: Addison and Pounder (1964, 1967); Addison, Stalinski and Pounder (1974); Cook (1960); Hoekstra (1969); and Hoekstra and Cappillino (1971). The remaining work, that of: Bogorodsky and Tripol'nikov (1973); Finkelstein, Goloshnev, and Petrov (1970); Morozov and Khokhlov (in press); Fujino (1967); Ragle, Blair and Persson (1964); Wentworth and Cohn (1964); Sackinger and Byrd (1972); and Vant, Gray, Ramseier and Makios (1974), lack a basis of comparison. Either they were performed at differing select values of salinity, or differing select values of temperature, or on different ice types.

Table 1

SUMMARY OF PUBLISHED RESULTS FOR SEA ICE

Author	Frequency	Salinity (‰)	Temperature (° C)	Comments
Addison & Pounder (1964, 1967)	20 Hz-100 MHz	7-20	22	Special cell used, artificial sea ice.
Addison (1969, 1970)	20 Hz-100 MHz	4-20	12.5-35	Special cell used, artificial sea ice.
Addison, Stalinski & Pounder (1974)	1 KHz	From saline water 35	25-150	Special cell used, artificial sea ice.
Cook (1960)	100 MHz	3.5, 7, 35	10-70	Synthetic sea ice
Hoekstra (1969)	10 GHz	10-60	0-25	NaCl ice
Hoekstra & Cappillino (1971)	100 MHz-10GHz	8	10	Flash frozen sea water, poor facsimile
Bogorodsky & Tripol'nikov (1973)	30 MHz, 60 MHz 100 MHz, 200 MHz	.56, 4.4, 8.6, 17.0	10-40	Sea water frozen in coax
Finkelstein, Goloshnev & Petrov (1970)	10 GHz	-	-	Inadequate temp., salinity data
Morozov, Khokl'hov (in press)	10 GHz	2.5-7.5	1-13	Good survey of ice types
Fujino (1967)	100 Hz-50 KHz	11, 13, 15	5-70	Natural sea ice
Ragle, Blair & Persson (1964)	150 MHz, 300 MHz 500 MHz, 1000 MHz	-	1-60	Very low salinity
Wentworth & Cohn (1964)	.1 MHz-30 MHz	.067-23	5-40	Possibly severe brine drainage
Sackinger & Byrd (1972)	26 GHz-40 GHz	2.85, 3.40, 7.20	7, 16.5, 21.5 25, 32	Natural sea ice
Vant, Gray, Ramseier & Makios (1974)	10 GHz, 30 GHz	.60-4.4, 7-8	0-60, 7	Natural sea ice, differentiation of ice types; artificial sea ice

It should also be noted that Hoekstra and Cappillino (1971) have performed the only measurements in the 1 GHz to 10 GHz range. The values plotted in Figure 1 are based on measurements performed on flash-frozen sea water. The rise and fall of absorption between 100 MHz and 10 GHz is somewhat suspect since there is no mechanism which would explain it, i.e. the absorption peak which starts at 8 GHz, approximately, is easily explained by the presence of brine in the ice, but at this time there is no reason to suspect a second peak of the magnitude which Hoekstra and Cappillino (1971) obtained.

The solid line in Figure 1 represents the "best" fit to the data available before the study on absorption in sea ice. The rapid rise at 20 GHz and subsequent fall at approximately 35 GHz may be misleading since the curve peak is due to the high values obtained by Hoekstra and Cappillino (1971) at 20 GHz. An alternative shape would be a continuous, monotonic somewhat more gradual rise commencing at 8 GHz and continuing up to the limit of the frequency axis. It should be noted however, that all the data contained on this graph was obtained over a range of temperature of -7 to -12° C, and a range of salinities of 5 to 10 ‰ and, therefore, the apparent scatter in the points is magnified.

It is obvious from the data that there was a tremendous gap in the understanding of the dielectric behaviour of sea ice in the 100 MHz to 10 GHz frequency range prior to the study, and it was with the aim of filling this gap that the study was performed.

3.2 Radar Probes

The significant advances in radar electronics over the past decade make it possible to attain a very high resolution for accurate depth sensing systems. These advances have been in the development of wide-band radar techniques, such as very short time duration and impulse systems. Vickers et al. (1974) and Chudobiak et al. (1974) with a pulsed radar system at S- and X-bands respectively, successfully measured the thickness of fresh water floating ice from various surface and airborne platforms.

Experiments with a much lower frequency pulsed radar have been reported by Bogorodsky and Tripol'nikov (1973). These concerned the sounding of sea ice thickness from an altitude of 100 m. A pulse length of 50 nanoseconds was used with a carrier frequency of 100 MHz. Good upper and bottom ice surface returns were obtained with first-year ice up to about 1.5 metres thick and multiyear ice up to several metres thick. Despite the relatively long pulse length, which undoubtedly limited the resolution of the thickness measurements, the feasibility of using airborne radar to obtain both upper and lower surface returns from sea ice was demonstrated. However, the problem of interpreting such sea ice thickness measurements without accurate knowledge of the temperature and classification of the ice being sounded was also illustrated.

Ground based systems developed by Geophysical Service Incorporated and Geophysical Surveys Systems Incorporated using an FM/CW system and impulse system (time domain radar), respectively, are well known in the oil industry and have been described

by Goodman (1974). A more complete survey of radar techniques is given by Page and Ramseier (1974).

3.3 Scatterometer

The microwave scatterometer is emerging as a powerful tool for determining ice type. The scatterometer is a calibrated, down-looking airborne radar which can be used to measure the backscatter coefficient σ^0 , as a function of aspect angle along a strip of terrain under an aircraft or spacecraft. Most scatterometers in existence today operate at roughly 13 GHz. Earlier work by Rouse (1969) and Parashar et al., (1975) demonstrated the potential of scatterometry for use in determining different ice types. They report the ability, in 85% of cases tried, to classify ice correctly into one of four gross thickness categories.

Recent, preliminary analysis of scatterometer data from the AIDJEX experiment has confirmed these earlier findings. In fact, the discrimination between first-year and multiyear ice is much greater than previously reported.

3.4 Active Microwave Mapping

Both passive and active microwave sensors offer the capability of an all-time, all-weather means of observing floating ice. One of the principal active sensors exploiting this capability is the side-looking radar (SLR). In its typical ice reconnaissance configuration the SLR is aircraft mounted, with the antenna, mounted beneath the aircraft, illuminating a narrow strip in a fixed sideways direction.

There are two fundamental types of SLR: real aperture and synthetic aperture. The real aperture system requires an extremely long antenna (~ 5 m) and has an along-track resolution which varies as $\lambda L/R$ where λ is the wavelength, R the range and L the aperture length. The synthetic aperture system has the capability of achieving a much higher resolution, L , when the system is focused (i.e. when the curvature of the reflected wave front is compensated for). In the unfocused mode of operation the resolution is approximately λR . The cross-track resolution in all types of SLR is determined by the system bandwidth and is constant across the illuminated area.

The SLR data product is in the form of a map. The coordinate perpendicular to the aircraft axis is a measure of radar backscatter as a function of range; the coordinate along the track is produced by the scanning action of the aircraft's forward motion.

Reflected in this backscatter are properties of the substance being sensed, in this case: the dielectric properties; volume distribution of scattering centres such as air bubbles and brine pockets; and the surface roughness of the ice.

Several studies of the application of such radars to sea ice have been reported, Anderson (1966), Guinard (1970), Johnson and Farmer (1971), Biache et al. (1971), Ketchum and Tooma (1973), Glushkov and Komarov (1971). Bogorodsky and Tripol'nikov

(1973, 1974) and Gorbunov and Losev (1974) have used SLR to observe a wide variety of ice types. Bogorodsky and Loshchilov (personal communication) have made, during the spring of 1973, an SLR map of the sea ice along the entire shipping lane north of the Eurasian continent. This map was made with the TOROZ 16 GHz real-aperture system, and it appears that this system is now being used operationally for ship routing along the northern sea route.

3.5 Passive Microwave Mapping

Perhaps the most rapidly evolving area of remote sensing research in floating ice has been in passive microwave applications. Both aircraft- and satellite-borne microwave radiometers have been used during the last five years to observe a wide variety of ice types. Although the time span is short, sufficient data now exists to enable us to conclude that such measurements will be a fundamental part of future ice observation programs.

Two of the most important series of aircraft flights which demonstrated the feasibility and usefulness of ice observations by means of passive microwave sensors were those that occurred during the AIDJEX (Arctic Ice Dynamics Joint Experiment) program and the U.S./U.S.S.R. BESEX (Bering Sea Experiment) joint program. A series of three AIDJEX pilot field experiments was performed during the springs of 1970, 1971, and 1972 in the southern Beaufort Sea. A wide variety of visual and infrared sensors were operated on a NASA aircraft at altitudes from 150 m to 11 km, in addition to a 19.4 GHz imaging radiometer and 1.42 GHz, 4.99 GHz, 10.7 GHz and 37.0 GHz radiometers.

The 1970 flights were made in June, north of Point Barrow. The microwave data (Wilheit et al. 1972) showed that it was possible to distinguish sea ice from liquid water both through the clouds and in the dark. This finding was of great interest because it pointed the way to an "all-time" ability to observe leads and polynii in the ice pack. The 1970 data also showed that strong microwave emissivity differences occur on the ice surface itself, but lack of sufficient ground-truth observations prevented a determination of the reason for these differences.

During the 1971 AIDJEX-NASA (National Aeronautics and Space Administration) experiments, a ground-truth program was carried out in conjunction with five overflights. The installation of an inertial guidance navigational system in the aircraft made it possible to fly high-level mosaicing missions with the 19.4 GHz imaging radiometer in which brightness temperature maps were made of a large area of sea ice (10,000 km²). Gloersen et al. (1973) found that the microwave emissivity differences of the sea-ice surface are associated with the age of the ice, the multiyear sea ice having cold brightness temperatures (≈ 210 K) and first-year ice having warm brightness temperatures (≈ 235 K). This was an important break-through, because it pointed the way to an all-time, all-weather means of distinguishing between old and new ice and tracking ice motion as well as lead and polynya development.

Microwave mosaic maps of the AIDJEX area and of the nearshore marginal ice zone showed that both morphological and dynamical ice features can be observed at all times in any weather. It has even proved possible to make a time sequence of the microwave mosaic maps showing the sea ice extending from Harrison Bay north into the Beaufort Sea for approximately 350 km from 4 to 23 April 1972.

AIDJEX-NASA flights in April, August, and October, 1975, performed a variety of missions during the main AIDJEX experiment. They will continue in April, 1976. The microwave and other data from these missions in conjunction with ground truth data, is being used to help interpret satellite microwave imagery of the ice pack and as input to numerical models of the pack.

The first passive microwave imager in space was the ESMR (electronically-scanned microwave radiometer) mounted on the NIMBUS 5 satellite which was launched on 11 December 1972. The microwave brightness temperature maps of the Arctic observed by ESMR provide the first synoptic maps of large-scale sea ice distribution. Used in combination with other imagery, Campbell et al. (1974) have shown that the ice cover of the Beaufort Sea is by no means heterogeneous, the size and type of floe distribution varies considerably in both east-west and north-south directions.

3.6 Ice Type Distribution in the Beaufort Sea

The ice cover of the Beaufort Sea is highly heterogeneous, its eastern sector being made up of large multiyear floes and its western sector a mixture of small, fragmented first-year and multiyear floes. Several studies have shown that along a constant latitude line the mean flow diameter decreases from 25 - 100 km in the east to 1 - 2 km in the west. Also, the average roundness of the floes decreases from east to west, (Campbell et al., 1974, Ramseier et al., 1975). Further, there is an increase in roundness in early summer from the more angular floe shapes of winter and spring.

In addition to the gross east-west trends there are recognizable differences across the shear zone. Gloersen et al. (1975), during spring flights northwards from Harrison Bay, Alaska, found a zone sequence from south to north of Zone 1) shorefast first-year sea ice, Zone 2) shear zone mixture of first-year sea ice, medium-size multiyear floes, thin ice and open water, Zone 3) first-year ice and small multiyear floes, Zone 4) first-year ice and medium to large multiyear floes and Zone 5) multiyear ice zone extending northwards to the Pole. In the summer, Zone 1 melts and Zones 2 and 3 suffer melting and reorganization. The location and width of the shear zone may vary from year to year and is a more constricted feature in the Canadian offshore areas, compared to the above zones which occurred over a 300 km distance.

4. STUDY AREAS

4.1 Offshore Program

During April 1975 a series of flights was made in the south Beaufort Sea and Mackenzie Bay. Four flights with 40 km offsets were run parallel to the Canadian coast (see Figure 13) from the Yukon coast in the southwest to Cape Bathurst in the northeast (refer to Section 6.2.2) by the DND (Department of National Defence) Argus with SLR on board.

A series of transects across this grid were flown by the CCRS (Canada Centre for Remote Sensing) C-47 with black and white photography, scatterometer and infrared line scanner on board (refer to Section 6.2.1).

4.2 Arctic Ice Dynamics Joint Experiment Site

Further offshore the AIDJEX Field area was used to ground truth (see glossary) the instruments flown in the offshore program. The area was centred on Big Bear, the main station on the drifting sea ice, with three satellite stations forming the apexes of a rough triangle. In April Big Bear was deployed at $76^{\circ} 20' \text{ N } 140^{\circ} 50' \text{ W}$, during the spring it drifted westwards to approximately 149° W , then in late summer returned to $137^{\circ} 44' \text{ W}$, and south to $73^{\circ} 41' \text{ N}$ (positions as of 6 October 1975).

4.3 Beaufort Sea

The analysis of NIMBUS 5 ESMR data (refer to Section 6.2.3) covers an area somewhat larger than a strictly defined Beaufort Sea would allow, but the nature of the data permitted a wider perspective which must be understood, eventually, in order to predict local ice conditions. The area is shown in Appendix Figure A1, from the mainland coast northwards to 80° N , and from the Chukchi Sea in the west to the Canadian archipelago islands margin in the east.

5. METHODS AND SOURCES OF DATA

5.1 Dielectric Measurements

The dielectric measurement program posed a considerable challenge to the available techniques. A novel transmission line-type sample holder had to be designed to allow measurement of the sea ice specimens over a broad frequency range.

The constraints placed on the device were that: it must be broadband in the extreme, i.e. 100 MHz - 8 GHz; it should be TEM (Transverse Electromagnetic Field) mode; it should be possible to place the ice specimen in the holder with a minimum of deformation of the ice; and it should also allow the measurement of the transmission coefficient of ice samples within $\pm 0.5 \text{ db}$, and $\pm 3^{\circ}$, which are the accuracies quoted for the measurement instrument (a Hewlett-Packard Network Analyzer). These constraints were met by a

coaxial-cage type design. The outer conductor of a special coaxial air line was replaced by four equally spaced rods. The correct ratios of spacing and inner to outer conductor diameter yields the required device. A similar device is described in Addison, Stalinski and Pounder (1974), and Addison (1975).

The final measurement scheme only required the drilling of five parallel holes, four on a concentric circle about a hole drilled along the central axis of a 3 inch (7.62 cm) ice core. This preparation generally required only 10 minutes at most and was performed at the ambient temperature (approximately -20°C). In this way representative ice samples were obtained.

Once the samples were prepared and mounted the specimens were measured at eight distinct frequencies; 100 MHz, 200 MHz, 400 MHz, 800 MHz, 1000 MHz, 2000 MHz, 4000 MHz, and 8000 MHz; as they were stepped through progressively warmer temperatures; -40°C , -30°C , -25°C , -15°C , -10°C and -5°C . All the ice specimens were columnar, first-year sea ice.

5.2 UHF Impulse Radar

The UHF impulse radar developed as part of the project, by the Communications Research Centre (CRC) in Ottawa and Carleton University, is a fundamental system, wherein a pulse is transmitted and the time separation of return pulses from various reflecting interfaces is measured. In the case of sea ice, where the ice forms a finite layer between the air above and the sea below, the principal reflections are from the air-ice interface and the ice-water interface with the time separation between the return pulses being a measure of the ice thickness.

The frequency range chosen (100-1000 MHz) is a compromise between the requirements for depth of penetration in the ice (lower frequencies desired due to the lower dielectric loss) and for vertical resolution in the ice (for which large bandwidths are necessary). The technical difficulties present in a radar of this type increase greatly whenever the ratio of the system bandwidth to the centre frequency increases. For the measurement of sea ice thickness these ratios are extreme, since the required pulse width of 1 nanosecond, occupies an enormous bandwidth, which in turn must be centered about such a low frequency as to achieve maximum penetration. These difficulties manifest themselves in the design of an antenna to radiate such a short pulse.

A travelling wave antenna structure was developed to meet these requirements, but as a result of the severe restraints imposed on the design its gain is necessarily low and it is rather bulky in appearance. However, it was estimated that a system employing these antennas could measure return signals with intensity 30 db lower than the output signal power. A preliminary ground-based UHF radar system was assembled for the AIDJEX experiment in the spring of 1975. The tests, however, were unsuccessful due to damage suffered by the prototype antennas en route to the ice camp. It was not possible to rectify the situation on the ice and repairs had to be made in Ottawa.

Since that time the Applied Instrumentation Laboratory of Carleton University has developed the antennas further. The analytical and experimental effort has been devoted to the development of a second generation antenna suitable for fitting to the existing UHF radar. The following two aspects have been considered:

- a) The form of the excitation waveform (i.e. baseband nanosecond impulses or other waveforms)
- b) The addition of resistive termination elements on the ends of the parallel plate V-type antenna structure.

Results obtained in the laboratory to date indicate that, by employing both appropriate resistive terminating elements and an excitation signal having a center carrier frequency of about 400 MHz (rather than a baseband impulse), radar sensitivity was improved by about 10 db relative to results obtained prior to May 1975. These preliminary results were obtained using simulated sea ice targets, such as moist sand (1 - 2 metres thick) and fresh water (1 - 2 metres deep). For these tests the antennas were excited by an experimental short pulse UHF radar (for which the excitation waveform is a single cycle of energy centred at 400 MHz).

In the near future under separate funding the development effort will be devoted to the refinement of the resistive termination technology for the antennas and to the performance of additional laboratory based moist sand, fresh water, and fresh-water-ice tests. Also planned is the modification of the existing impulse type UHF radar to a short pulse (monocycle) UHF radar with the short pulse centered at 400 MHz.

Although the system was not employed successfully for the measurement of sea ice thickness as part of the Beaufort Sea Project, due to the short duration of the project and delays in development, it is felt that the system will be used successfully for the measurement of sea ice thickness at least in the ground based mode, in the near future.

5.3 Scatterometer

The Ryan Scatterometer, owned by the Canada Centre for Remote Sensing (CCRS), measures quantitatively the back-scattering of microwave radiation, over a range of incidence angles from approximately 5° to 60° from nadir. The system operates at 13.3 GHz (2.25 cm wavelength in free space) and is similar to the NASA 13.3 GHz scatterometer which has been used in airborne remote sensing studies of sea ice. Either horizontally or vertically polarized continuous wave, CW, signals can be transmitted with the CCRS instrument, also both the like- and cross-polarized returns are received simultaneously. This is in contrast to the NASA scatterometer which transmits and receives only vertically polarized radiation. The slotted waveguide array antennas radiate a fan beam in the fore-aft direction, with an along-track beamwidth of 120° and a cross-track beamwidth of 3° (Figure 2). The two transmit and two receive antennas have approximately the same gain patterns.

The ground return signal is frequency broadened about the transmitted frequency due to the Doppler effect, arising from the relative motion of the aircraft and the ground. Since the Doppler frequency shift depends on the angle of incidence, computation of the back-scattering coefficient λ° as a function of angle is possible. Details of the quantitative data reduction are given in reports by Royer (1975) and Bradley (1971). The microwave receiver operates in a homodyne or zero (Intermediate Frequency) mode, consequently, the fore and aft return signals are folded into the same audio frequency range. In order to resolve the ambiguity between the returns at a particular angle fore and aft of nadir, two outputs are generated in phase quadrature to one another. These outputs, referred to as the cosine and sine signals, can be recorded using a tape recorder and processed subsequent to the flight.

Alternately the fore-aft ambiguity can be removed in real time, on board, using an instrument referred to as the combiner. The combiner used in this work was designed and built at the Communications Research Centre by G.M. Royer and P. Xhignesse. The scatterometer cosine and sine signals are combined to generate one output signal which has a spectrum centered at 10 kHz, with the fore returns upshifted by their Doppler shift frequency with respect to 10 kHz and the aft returns downshifted with respect to 10 kHz. Figure 3 illustrates the operation of the system in block diagram form. Internally generated signals are used to calibrate the return spectra so that absolute values for the scattering coefficients can be calculated. The calibration signals appear at 7 kHz in the horizontally polarized cosine and sine channels and at 3 and 17 kHz in the combiner output. Figure 4 shows an actual power spectrum of the combiner output obtained during one flight over a region of predominantly first-year ice. In principle it is possible to generate quantitative scattering coefficients, as a function of angle, by comparing the magnitude of the power spectra density at particular frequencies with the magnitude of the calibration signal. Corrections due to the antenna gain patterns, spectrum analyser bandwidth and variation in system gain with frequency must be included in the calculation of $\sigma^\circ(\theta)$. This procedure is valuable when flying over isotropic terrain (e.g. sea surfaces) for which the returns are statistically stationary but is of no quantitative value when flying over anisotropic terrain. The procedure followed in this case is to select a suitable angle, set the spectrum analyser to the appropriate frequency and monitor the back-scattering in real time at that angle.

More complete data processing is possible, subsequent to the flight, and can be performed either by digital or analog methods. Using the digital processing method scattering coefficients as a function of angle can be generated for successive ground footprints (see glossary). This method is very flexible, powerful and one can obtain a detailed picture of the scattering of ground footprints as small as approximately 15 by 15 metres. Unfortunately, the digital method is both time consuming and inefficient. The original recorded analog data must be digitized onto computer compatible tapes and then successive records from the digital tapes must be transformed, using fast Fourier transform techniques, into the frequency domain. Corrections due to antenna patterns and system gain variations can be made easily using the computer processing technique. Because it takes approximately 20-60 minutes of computer processing time to process one minute of raw data it was unrealistic to attempt digital processing of all the data collected for the Beaufort

Sea Project. Analog processing, while giving less detailed results, can be performed more readily by playing back the recorded data through a spectrum analyser. This method has been used to generate the results contained in this report, although reference has been made to results obtained by digital processing of data obtained over the AIDJEX site. Sufficient detail and information can be obtained with the analog technique to aid in the identification of ice types and to help in obtaining a distribution map in the area of interest.

Most of the scatterometer results contained in this report have been obtained by playing back the recorded combiner data through an Hewlett-Packard 3580A Spectrum Analyser used as illustrated in Figure 5. The relationship between the centre frequency of the spectrum analyser and the aft scatterometer look-angle is given by:

$$\nu = 10,000 - \frac{2 V \sin \theta}{\lambda}$$

where V is the ground speed, θ is the incidence angle and λ is the wavelength of the microwave radiation. The filter bandwidth of the spectrum analyser was set to either 300 Hz or 100 Hz. The instantaneous ground footprint length is related approximately to the bandpass filter bandwidth Δf by:

$$L = \frac{H \lambda \Delta f}{2 V \cos^3 \theta}$$

where H is the aircraft altitude above the ground. Consequently, the returns at any instant of one of the plots of $\sigma^\circ(\theta)$ are integrated over a ground footprint dependent strongly on θ (the incidence angle). At 45° to nadir the length of the window is approximately 20 metres for the 100 Hz bandwidth and 60 metres for the 300 Hz bandwidth. In interpreting the analog results the time constant on the output of the spectrum analyser should be considered also. It is appropriate to select an RC filter with a time constant approximately equal to the time required by the aircraft to traverse the distance L . Time constants of 0.25 and 0.7 seconds have been used in generating the scattering results. The small scale noise in all the scatterometer plots does not represent instrumental noise, rather this reflects variation in terrain scattering and the statistical nature of the returns.

5.4 Side-Looking Radar

The program was carried out using a Motorola AN/APS 94D, X-band, real aperture side-looking radar. The system was flown aboard an Argus of the Canadian Forces, Maritime Proving and Evaluation Unit with imaging on either, or both, sides of the aircraft and range swaths of 25, 50 or 100 km per side. All the imagery contains a nonimaged blind strip down the center of the track, which is outside the field of view of the antenna and is about twice as wide as the altitude of the aircraft. Cross-track resolution is constant at about 30 m and along-track resolution is approximately 8 m per kilometre of range.

The azimuthal, or along-track, resolution is determined by the along-track beamwidth of the antenna. The longest possible antenna is carried under the aircraft to obtain the narrowest possible along-track beamwidth. As in conventional radars, the range resolution, or cross-track resolution, is determined by the modulation (bandwidth) applied to the transmitted energy (usually narrow pulses). Although it is relatively easy to achieve high cross-track resolution, the transmitter modulation is usually chosen so that this resolution approximates the more limited along-track resolution. This is determined by the angular spread of the antenna beam in the along-track direction. The along-track resolution of the resulting imagery is degraded linearly with increasing range from the transmitter.

The SLR was flown in April 1975 over the Beaufort Sea area, imaging the AIDJEX field area, the offshore zone and the Mackenzie Delta. A repeat mission scheduled for October 1975 unfortunately had to be cancelled due to instrument malfunction; it is now rescheduled for February 1976.

5.5 Electronically-Scanned Microwave Radiometer

Information for this part of the study was obtained through NASA Goddard Space Flight Centre from the ESMR instrument on board the Nimbus-5 satellite launched in December 1972. The imaging radiometer system has been described by Wilheit (1972) and Allison et al. (1974). The maps of brightness temperature emanating from the surface of the Earth, provide the first synoptic maps of large-scale sea ice distribution.

Data was obtained initially in the form of numerical computer printouts for the whole of the polar region north of 60° N on a once per month basis. More recently an enhanced false-colour photographic product has been devised for the same polar projection. The brightness temperatures at any location result from a three-day averaging of the satellite data in order to provide complete earth coverage. Both the computer plots and photographs have been used to contour areas of similar brightness temperature.

The plots have 5° Kelvin increments in the range 135° K to 285° K; open water is usually less than 140° K and sea ice registers 200 - 260° K according to its type and thickness. The principally multiyear ice is indicated by brightness temperatures between 209 and 223° K, while first-year ice emits 232 - 250° K and ice mixtures register temperatures in between. Mixtures of water and ice at an ice edge result in intermediate temperatures of 145° K to 200° K in rapid succession.

A zoom transfer-scope was used to draw the contour maps, directly from the false-colour photography, over the area of the Beaufort Sea and adjacent Arctic Ocean shown in Appendix Figure 1. These maps (Appendix Figures A2-26), were considered in the light of the discussions by Gloersen et al. (1975), to infer the percentages of multiyear ice, first-year ice and open water in the pack.

6. RESULTS

6.1 Dielectric Properties of Sea Ice

A summary of the measurements of absorption in (db/m) is shown as the dashed line labelled AIDJEX data in Figure 1. Note the gradual rise from values near those obtained by Finkelstein et al. (1970), and Bogorodsky and Tripol'nikov (1973), to those obtained by Vant et al. (1974), and Morozov and Khokhlov (1975). This contrasts with, and is much lower in magnitude than, the results of Hoekstra and Cappillino (1971). It is felt that, because of the techniques used in this study to preserve the in-situ properties of the sea ice specimens, this curve more clearly represents the true behaviour of sea ice than the data previously obtained in this frequency range.

Since the main purpose of this project was to determine sea ice thickness and not the dielectric properties, the presentation of the results will consist solely of Figures 6-11 and a brief explanation. These figures are empirical curves prepared using the experimental data. It is felt that all bumps in the curves are significant in that they are based on statistical estimates of the properties at the stated temperature and salinity and as such reflect a large number of data points. The dashed lines from 4-10 GHz are meant to represent an increase in statistical uncertainty in the empirical model. It was felt that a solid line could not be justified here.

Some basic trends in the data are obvious. The dielectric constant (ϵ') decreases with frequency and temperature and increases with salinity, while the loss in (db/m) increases with frequency and salinity, but decreases with temperature. The spacing between the curves is determined by the brine volume relations, i.e. as the various salts precipitate out of solution the spacing changes. The bumps in the curves, it is felt, may be attributed both to dipole interaction between the brine inclusions and brine relaxation.

What is clear from the study is that the dielectric properties of sea ice vary greatly with frequency, temperature, salinity and these factors must be taken into account when evaluating radar performance.

6.2 Active and Passive Microwave Mapping

6.2.1 Scatterometer Results

The Canada Centre for Remote Sensing mission over the AIDJEX field area, 13 April 1974, flew the Ryan scatterometer in addition to an Aerojet 37 GHz dual-polarized radiometer, Daedalus infrared line scanner and an RC-10 surveying camera. The same sensors, excluding the 37 GHz radiometer, were flown during the Beaufort Sea missions of 18-20 April 1975.

All the instruments were annotated with a time code signal so that good registration of the visible, infrared and microwave results was possible. In the present report relative scatterometer measurements are given to aid in the ice-type classification and distribution mapping based on the SLAR imagery.

For the AIDJEX site ground truth was obtained by the authors, whereas ground truth for the offshore program was provided by L.G. Spedding, Imperial Oil, Calgary.

Preliminary analog and digital processing of the scatterometer data taken over the AIDJEX site has shown that there is significant contrast in the microwave backscatter between multiyear and first-year ice, particularly for the cross-polarized components $\sigma_{\perp}^{\text{VH}}(\theta)$. Figure 12 includes three analog traces of results obtained from one of the flight lines at the AIDJEX site. The top two traces illustrate relative variation in the backscatter at 45° fore of nadir, while the lower trace illustrates, qualitatively, the variation in microwave brightness temperature as measured concurrently by the Aerojet 37 GHz radiometer. The ground footprint observed by the microwave radiometer corresponds approximately to the footprint as measured by the scatterometer in traces one and two. The plot of the horizontally polarized radiometer has been drawn to emphasize the correspondence between the results obtained by the passive radiometer operating at 37 GHz and the active scatterometer operating at 13.3 GHz. Regions A and B in the results illustrated in Figure 12 correspond in time to observations made over two regions of first-year ice in a refrozen polynya. Region A represents an area of grey ice which was thinner than Region B and which shows significantly higher thermal infrared emission and good detail in the line scanner imagery. The snow-covered first-year ice in Region B was thicker and the infrared imagery showed negligible contrast between the first-year ice at B and the multiyear ice beginning after the Region B. The 37 GHz radiometer appears to be insensitive to the different thicknesses of sea-ice in the refrozen polynya. It is interesting to note also that the lower frequency scatterometer indicates a higher backscatter at 45° to nadir than the thinner grey ice in the middle of the polynya.

In the regions of predominantly multiyear ice (C and F in Figure 12) the backscatter increases significantly in relation to the relatively thick first-year ice observed at B, D or E. The difference in backscatter at 45° between these regions increased to approximately 20 db for the cross-polarized results $\sigma_{\perp}^{\text{VH}}$ in trace one and approximately 13 db for the like-polarized results $\sigma_{\parallel}^{\text{VV}}$ in trace two. The microwave brightness temperature decreased by approximately 60° for the regions of predominantly multiyear ice as seen in trace three. The first-year ice feature, labelled E in Figure 12, corresponds to the intersection of the flight line with the first-year ice used as the runway at the AIDJEX site. The feature labelled D corresponds to snow-covered, first-year ice in a region of predominantly multiyear ice. Identification of this region as being first-year ice would have been very difficult, if not impossible, on the basis of the visible or thermal infrared imagery alone. More detailed analog and digital data processing, on the quantitative variation of the scattering coefficients with angle, is currently being done.

Microwave scattering from sea ice is relatively complicated due to the variations that can exist in both the age of the ice and in the conditions which occurred during its formation and weathering. In the Beaufort Sea area the problem is compounded due to the variations in salinity of the water close to the Mackenzie Delta. Water close to the southern end of line 3 (in Figure 13) has a lower salinity than normal for sea water. Consequently, the microwave scattering by the ice may vary due to changes in its surface conductivity and dielectric constant. Normally, there is a high attenuation of 13.3 GHz radiation internally in sea ice, therefore at most, the top few centimetres of multiyear ice and only a few millimetres of first-year ice are sensed.

The work on processing the scatterometer data has concentrated on Line 3 in Figure 13 because more detailed ground truth has been obtained for this line. The shorefast ice, the extent of which is shown approximately in Figure 13, contained multiyear ice floes, (L.G. Spedding, personal communication) verified by ice sampling and aerial surveying of the flight lines by Imperial Oil in November, 1974. Figures 14 and 15 illustrate the variation in microwave scattering (logarithmic scale) measured at 45° to nadir over the southern half of Line 3 in Figure 13. The contrast between the snow-covered, shorefast ice and the first-year ice north of the shear zone can be seen clearly in both the black and white photography and infrared imagery. Using the time code signal annotated onto the visible and infrared imagery, point C in the scatterometer results (Figure 14) can be aligned quite accurately with the shear zone (see also Figure 20 in 6.2.2). The region north of the shear zone was predominantly young ice formed subsequent to the opening, in March, of a large lead of water up to 112 km wide and extending across the mouth of Mackenzie Bay. The assessment that ice in the region D to C included a high density of multiyear ice floes can be made confidently on the basis of results in Figures 15, 16 and 17 and by comparison with the AIDJEX results. Similarly the features labelled as E, G, can be identified as multiyear ice floes trapped in the first-year ice, with the feature labelled as F probably fitting this identification also.

A further interesting feature observable in the scatterometer results, contained in Figure 15, is the gradual decrease in the cross-polarized scattering $\sigma_{HV}(\theta)$ from the shorefast ice with increasing distance from the shore. Figure 15 includes a comparison between the like-polarized, Trace A, and cross-polarized, Trace B, component and shows that the effect is more pronounced in the latter. Consequently, the possibility exists that the variation is related, either directly or indirectly, to salinity changes, near the surface of the ice, with age. The increase in microwave scattering and decrease in microwave radiometric brightness temperature (Meeks et al. 1974) between first-year and multiyear ice is associated, in part, with changes in surface dielectric constant and concentration of scattering centres.

The relative scale, in db, between the two plots in Figure 15 is unchanged and shows that at 45° to nadir, the contrast between the multiyear ice and first-year ice is greater in the cross-polarized component than in the like-polarized component. Differences in the scatterometer horizontal and vertical receivers, antenna patterns and gain variations with frequency can be included in the calculations so that comparisons can be made between the

magnitude of the like- and cross-polarized returns. Using the multiyear ice floe labelled as G in Figure 13 and 14 as an example, the contrast between the first-year ice and the multiyear ice is approximately 19 db in the cross-polarized (lower) trace and approximately 13 db in the like-polarized (upper) trace. Further, it has been estimated that the magnitude of the cross-polarized component of the backscattering is approximately 3-6 db less than the magnitude of the like-polarized component for multiyear ice and approximately 9-12 db less than the like-polarized component for first-year ice.

Figures 16 and 17 illustrate the variation in backscattering as a function of angle for part of Line 3. The plots were obtained with the spectrum analyser, centre frequency adjusted so that scattering from angles of 5°, 15°, 25°, 35°, 45° and 55° to nadir was obtained. Throughout these plots the bandwidth of the spectrum analyser filter was set at 300 Hz and a time constant of 0.25 seconds was used on the output of the spectrum analyser. Due to the constant bandwidth the returns are integrated over a ground cell length which is longer for the higher incidence angle values. As a consequence the results for 55° appear to be smoother than the other plots, essentially because more spatial averaging has been performed. Significantly higher contrast between multiyear and first-year ice is observed for the cross-polarized results in Figure 15 at all angles than with the like-polarized results. Also, the contrast between the multiyear and first-year ice is particularly interesting at 5° to nadir (Figure 18). In this case, the like-polarized results do not distinguish ice types, however, there remains useful information in the cross-polarized results. With angles from 15° to 55° to nadir there is little change in the relative scattering between different ice types, particularly for the cross-polarized results in Figure 15.

Some of the features observed in the scatterometer results can be correlated with features in the visible and thermal infrared results. The time code signal enables some of the multiyear ice floes in the shorefast ice, identified in the scatterometer results, to be correlated with the visible and infrared imagery. Although the entire shorefast ice region was covered with approximately 40 cm of snow, nevertheless, there is some indication in the black and white photography of an increase in the surface roughness compared with the multiyear ice floes. Dry snow leads to a small attenuation of 13 GHz microwave radiation and the relatively low scattering observed from Features J and H in the scatterometer results may indicate different surface textures in the first-year ice and possibly different ice thicknesses. Feature J is clearly visible in the black and white photography and the pressure ridging visible in the photograph probably has caused the peaks in the scattering on either side of the minimum. Feature H in the scatterometer returns has no obvious counterpart in the visible photography but there is a feature in the infrared imagery which appears as a slightly darker (hotter) band. Exact ice and snow thickness measurements were not made in the area but L.G. Spedding confirmed that refrozen leads (which had opened in February) could correspond to Features J and H. These results attest to the high sensitivity of the Daedalus line scanner.

In the flight lines flown by the C-47, isolated multiyear ice floes were observed near Herschel Island in the shorefast ice and more frequently in the shorefast ice adjacent to the shear zone. With the exception of the multiyear ice near Herschel Island the other

regions have been identified in the SLR mosaic. No multiyear ice floes in the young ice north of the shear zone have been identified in the scatterometer results.

6.2.2 Side-Looking Radar Results

In the AIDJEX area the Motorola AN/APS 94D real aperture SLR was flown aboard the DND Argus aircraft in April 1975 and produced excellent imagery. An example near the Big Bear camp is shown in Figure 19, with many features resolved in detail.

The camp can be identified as the black area near the centre of the image. Rough features appear dark in this image while smooth areas are light. The light linear features represent refrozen leads. All leads are covered with varying thicknesses of grey ice. Just north of and adjacent to the camp, the white linear feature running east-west represents the runway, consisting of 1.6 m thick first-year ice. The camp is located on a small multiyear ice floe having an average thickness of 3.5 m. The dark lines within this floe represent ridges having a height of approximately 2 m and a width of 3 m. The large lead which runs from northwest to southeast consists of grey ice with a thickness of 0.7 m. One aspect which is striking in this image concerns the backscattering coefficient σ . For example, the radar returns (grey scale) for the multiyear ice on which the camp is located and the large lead to the west of the camp are very much alike. If it were not for the geometry of the ice, one could not distinguish first-year from multiyear ice. This is of great concern, since one of the future goals is to be able to process automatically digitized SLR data to obtain percentages of first-year and multiyear ice. The wavelike pattern on the east side of the camp running north-south is due to the aircraft motion. There is no question, however, that the information content of the SLR image is significant. The geometrical features of ice floes, leads, ridges, rubble ice fields, rafting in grey ice, are very distinct.

Figure 20 shows imagery in the Beaufort Sea from four almost parallel tracks, the most southerly of which includes the Mackenzie Delta coastline, from Mackenzie Bay to Cape Dalhousie. The shorefast ice appears palest grey and smooth, with man-made structures clearly visible. The northeastern portion of shorefast ice had incorporated floes of multiyear ice, some of which were grounded, with particularly high concentration close to the shear zone.

The major lead (also noted in 6.2.1) in the shorefast ice is a very prominent feature, refrozen with smooth-surfaced, young ice. It is known that the lead opened in March 1975. Although discontinuous the feature can be seen again off Richards Island but does not exist in the southwestern portion of the imagery in the shear zone off Mackenzie Bay.

The SLR gives good definition to the shape and surface form of ice floes in the pack north of the shear zone lead. Notable are very large, probably first-year, ice floes near the centre of the area shown, with fractures clearly visible across them. In conjunction with the scatterometer results a good assessment of age for individual floes can be made; superimposed on the figure is the scatterometer trace of Figure 14 described in 6.2.1.

Figure 21 shows a SLR image of the Mackenzie Delta area. The light tone on the south side represents shorefast ice, followed in the north with the distinct shorefast ice-pack ice boundary. The darker, rounded areas within the shorefast ice represent stranded pieces of multiyear ice which are snow-covered. These pieces of multiyear ice are not visible in the aerial photographs taken over the same area. The large floe in the centre of the image is multiyear ice. A lead running from the southwest to the northeast contains some grey-white ice (the darker area) and newly formed thin grey ice (light area) both of which are of varying thicknesses due to rafting. The northern part of the pack ice consists almost entirely of ridged first-year ice.

Within the Mackenzie Delta area, Figures 22(a) and (b) show similar results to those obtained by Sellman et al (1975). It represents two SLR images taken at 90° to each other showing the channels and lakes in the Delta. The dark areas in the main channel in Figure 22a represent high backscatter, meaning the channel is not frozen to the bottom as compared to the lighter areas which are. Where the channel meanders, the ice on the shallow, inside portion of the meander freezes all the way to the bottom, whereas on the outside of the curve where the water is much deeper, an ice-water interface exists. The thickness of the ice is of the order of 2 m. The high backscatter from the central part of the river does not vary much since the incidence angle stays nearly constant. However, in Figure 22b which shows part of the same portion of the channel, the backscatter varies considerably as a function of incidence angle. This becomes even more pronounced if one compares the backscatter of the river with the one of the lakes located at high incidence angles. It should also be noted that the large lake in Figure 22b shows variations in backscatter of the floating part of the ice cover which presently cannot be explained.

6.2.3 Electronically-Scanned Microwave Radiometer Results

The maps of brightness temperature contours are shown in the Appendix, Figures 2-26. Contours were drawn initially at 25° K intervals (145, 170, 195, 220 and 240° K). In order to elucidate sea ice features additional contours were drawn at 210, 215 and 230° K. (In the final drafting the 170° K contour was omitted to assist clarity; it was close to, and sub-parallel to the ice-water interface.)

The monthly maps cover the time period from December 1972 to April 1975. Exceptions are March, April, May and August, 1973 when the instrument was down; August 1974 was also missing but was replaced by an extra three-day coverage for late July. Certain maps have restricted areas of no data close to the Alaska tracking station.

It should be mentioned that the brightness temperatures in any one area, for different months, cannot be compared absolutely due to seasonal fluctuations of the ambient air/ice temperatures. This study has incomplete analysis due to time constraints, but will be reviewed in the future with reference to meteorological charts.

Gloersen et al. (1975) drew a linear interpolation, the heavy dashed line in Figure 23 between cases of completely open water (brightness temperature T_B of 131° K)

and completely first-year ice (T_B 250° K) in order to infer the compactness of the sea ice, and percentages of open water and first-year ice. Surface temperature differences, of 240 to 260° K, and uncertainty of brightness temperature measurement are indicated by the finely dashed lines. The present authors made similar interpolations for the case of open water and multiyear ice (T_B 215° K), solid line in Figure 23, and multiyear ice (T_B 215° K) and first-year ice (T_B 250° K) shown in Figure 24.

It was assumed that by September in any year the melt season had ended and the ice remaining was second-year or older. Figures 25 to 28 show the results of interpreting the September and October brightness temperature maps, in order to obtain the percentages of open water and multiyear ice, using Figure 23.

The September 1973 map shows a broad belt of high percentage open water from Amundsen Gulf to the Alaska/Yukon border, then a steady widening northwards of this zone across the Chukchi Sea. Ice growth in October had constricted this belt particularly the 80-100% open water areas which remained only in Amundsen Gulf and the Chukchi Sea. The northern boundary of the belt across the Chukchi Sea had moved south and the triangular shape is less pronounced. To the northeast of this boundary the area of nil open water had brightness temperatures of 230° K (Appendix Figure 8). If first-year ice predominated in this area, according to the Gloersen et al. (1974) linear interpolation a maximum of 15% open water could be expected; if there was indeed 0% open water then Figure 24 indicates a mixture of almost equal proportions of multiyear and first-year ice.

Figures 25 and 26 contrast with the ice conditions for 1974, when the offshore open water belt was narrower and the 80-100% open water condition was not present (Figure 27). The Chukchi Sea triangle had a similar northwards extent but was a much stronger feature and was still well maintained in October (Figure 28). By October also the Canadian offshore areas had a high percentage of new ice growth with warm brightness temperatures (Appendix Figure 20, 245 and 232° K) indicating only 0-15% open water.

A map to summarize the minimum ice conditions (Figure 29) contrasts the areal extent of the pack ice in September 1973 and 74. The 10% open water contour is shown to define the remaining area of compact ice after summer melting. Both years follow the same trends but the pack ice in 1973 was more restricted than 1974, further north by roughly 100 km in the Beaufort Sea and almost 200 km in the Chukchi Sea.

A similar reinterpretation of Gloersen et al. (1975) was performed for winter conditions. In this case open water was assumed minimal and the linear interpolation was between cases of completely multiyear ice (T_B 215° K) and completely first-year ice (T_B 250° K) in order to resolve the percentage of first-year ice in the area of sea ice, (Figure 24). All the available brightness temperature maps for December, January, February and March were used to compile Figures 30-40.

In 1972-73 (Figure 30-32) the Chukchi Sea triangle is visible in January and February and the offshore belt showed decreases in first-year ice proportions from 45-65% in December to 15-45% in February. The area of entirely multiyear ice steadily increased from the northeast, south to 75° N off Banks Island in February.

The ice conditions were generally similar in 1973-74, (Figures 33-36), except that the Chukchi Sea triangle was less apparent and had 15-45% first-year ice in February compared to 45-65% in February of 1973, Figure 32. The southward growth of the multiyear ice area extends to approximately the same location as, but a month later than, the previous winter.

A much different situation developed during the 1974-75 winter season, (Figures 37-40). A large area of exclusively multiyear ice covered the Arctic Ocean in December, increasing by January to reach within 50-150 km of the Alaska/Canada coastline. The narrow coastal belt had only 0-45% first-year ice.

The trend then reversed, in February 1975 (Figure 39), when from the southwest increasing amounts of first-year ice occupied the Chukchi Sea and by March the map is fairly comparable to March 1974 (Figure 35) conditions.

It is interesting to note that Figure 40 is just a little earlier than the SLR imagery flown parallel to the Mackenzie Delta coast. The offshore area shows 45-65% first-year ice. Referring to the brightness temperature map for April 11-13 (Appendix Figure 27) first-year ice brightness temperatures of 245° K, in the same area, give 85% first-year ice which compares favourably with the interpretation of the SLR imagery, Figure 21.

The preceding figures show that maximum extent of multiyear ice occurs in February for 1973 and 1974. The ice situation was somewhat unique in early 1975 but again February may be used for comparison. The percentage contour for the extreme case of 0% first-year ice was drawn for each winter and Figure 41 shows the comparison. The lines all follow the same trend, with, as expected, more multiyear ice in 1975 in southerly and westerly extent. The March contours for 1974 and 1975 both approximate fairly closely to the February 1973 boundary.

Although not displayed, the late-winter positions of the 45% first-year ice contour are also quite comparable, and generally define the northern limit of the Chukchi Sea triangle, but do not occur along the coastal belt.

7. CONCLUSIONS AND RECOMMENDATIONS

Although the study was not completely satisfactory in that direct thickness measurements on sea ice were not performed there were several significant advances made. The dielectric properties of sea ice were studied over a comprehensive range of frequencies and salinities for the first time, enabling an attempt to be made at interpretation of direct radar thickness measurements when the need arises. Also, a UHF impulse radar was

developed to the stage that it is now ready for testing on the surface of the ice. This radar represents a significant breakthrough in the technology necessary for direct ice thickness measurements. It is recommended that the UHF radar development be pursued further until an operational system is ready for use.

The scatterometer results represent remote sensing work done over a relatively short period of time during one spring season. The applicability of the results from year to year or even throughout one winter is not known. It is encouraging, however, that the scatterometer results observed at the AIDJEX site are comparable with the results obtained in the Beaufort Sea Project. (One exception, however, is the scattering behaviour in the regions close to the Mackenzie Delta where the salinity is not typical of sea-ice.) The contrast observed by the NASA scatterometer between multiyear and first-year ice is less than that observed during the CCRS C-47 missions. Consequently, there may be changes from year to year which could affect the generality of the results reported in this work.

The following tentative conclusions can be drawn from the scatterometer results obtained from both the AIDJEX and Beaufort Sea flight lines.

(i) In the identification of different sea-ice types using the dual-polarized scatterometer, the detection of the cross-polarized component of the back-scattered radiation leads to a greater contrast between multiyear and first-year ice types.

(ii) The contrast and detail in the results illustrated in Figures 9 and 10 for both the like- and cross-polarized returns do not vary significantly with incidence angle in the range of approximately $15-60^\circ$ to nadir. Consequently, a calibrated, side-looking imaging radar system with a wavelength of a few centimetres and operating with a relatively high depression angle mode (as is envisaged for satellite operation), would provide grey scale information of use in ice-type classification mapping. An appropriate roll-off with angle due to the back-scattering coefficient variation would have to be included in the processing. Possible ambiguities still may exist between the returns from water, at certain wind speeds, and smooth first-year ice but it is possible that spatial information and relative grey scale differences across the swath may help resolve this problem. A high dynamic range would have to be preserved throughout the data processing, particularly if a cross-polarized channel were incorporated in the SLAR System.

(iii) With similar conditions to those encountered during these missions the scatterometer could be used in real time to detect and monitor changes in ice type along a flight line. On the basis of the results in Figure 9 the study of the cross-polarized back-scattering at one angle in the range $20^\circ - 60^\circ$ should be sufficient for the determination of ice type particularly if the results could be correlated with visible or infrared observations.

(iv) At near-nadir angles the cross-polarized returns contain information on the ice type while the like-polarized returns do not. This has significance in the actual scattering mechanisms involved.

Both the SLR and scatterometer results were of demonstrative nature, i.e. they illustrate some of the things it is possible to achieve with this type of imagery. It was easily possible to distinguish the shear zone, the shorefast ice, and first-year ice, as well as identify multiyear floes. The SLR imagery offers the potential for determining the concentration of: open water; multiyear ice; shorefast ice; and first-year ice; as well as delineating floe size, leads, and ridge frequency in all types of weather. Time did not permit complete analysis of the offshore imagery but it was useful as a method of ground truth for the ESMR imagery.

Recommendations have been made above on how an operational SLR or scatterometer system could be used to monitor ice types.

The Nimbus-5 imagery enabled detailed analysis of the ice cover, and percentages of first-year ice, multiyear ice, and open water to be determined. The results are naturally averaged over an area due to the large resolution cell size of the instrument. It is instructive to note however that this imagery if combined with detailed, more extensive SLR coverage can give a much more complete synopsis of ice cover, under all weather conditions, and over larger areas than presently possible with the visual observation system.

8. ACKNOWLEDGEMENTS

The authors would like to acknowledge: the very active support, by both logistical and financial means, given by the Polar Continental Shelf Project; the practical support of the Airborne Sensing Unit (C-47) and Maritime Proving and Evaluation Unit (Argus) staff; the interaction with Imperial Oil Ltd., particularly L.G. Spedding; the supply of ESMR data by NASA Goddard, in particular the assistance of Drs. P. Gloersen and H.J. Zwally. We would like to mention especially the superior technical assistance of R.J. Weaver and M. Holtz.

The authors are grateful for the monetary support from the Beaufort Sea Project Office. The ultimate goal of measuring sea ice thickness directly was not accomplished, but the support has gone a long way towards assuring success in the near future.

9. GLOSSARY

AIDJEX - Arctic Ice Dynamics Joint Experiment

CCRS - Canada Centre for Remote Sensing

DND - Department of National Defence

ESMR - Electronically-Scanned Microwave Radiometer

ground footprint - the effective area on the ground illuminated or sensed by an airborne antenna.

ground truth - independent information acquired by a field party, on the ground, about an area being sensed. Usually this information supplies clues as to the interpretation of the data acquired using remote sensing techniques.

SLR - Side-Looking Radar.

10. REFERENCES

- Addison, J.R. (1969). Electrical properties of saline ice. *Journal of Applied Physics*, 40(8), p. 3105-14.
- Addison, J.R. (1970). Electrical relaxation in saline ice. *Journal of Applied Physics*, 41(1), p. 54-63.
- Addison, J.R. (1975). An open sample holder for electrical measurements between 0.1 and 6.0 GHz. *Review of Scientific Instrumentation*, 46(1), p. 101-102.
- Addison, J.R. and Pounder, E.R. (1964). USAF Report. AFCRL-64-52.
- Addison, J.R. and Pounder, E.R. (1967). The electrical properties of saline ice. In: *International Conference on Low Temperature Science*, Hokkaido University, Sapporo, Japan, p. 663.
- Addison, J.R., Stalinski, P. and Pounder, E.R. (1974). Studies on the electrical properties of saline ice. Office of Naval Research, U.S. Navy Department, N00014-7-00312 69pp.
- Allison, L.J., Rodgers, E.B., Wilheit, T.T. and Wexler, R. (1974). A multi-sensor analysis of Nimbus-5 data on 22 January 1973. NASA X-910-74-20, Goddard Space Flight Centre, 55pp.
- Anderson, V.H. (1966). High altitude side-looking radar images of sea ice in the Arctic. *Proceedings of the fourth Symposium on Remote Sensing of Environment 1966*, Ann Arbor, Willow Run Laboratories, Institute of Science and Technology, University of Michigan, p. 845-47.
- Biache, A., Jr., Bay, C.A. and Bradie, R. (1971). Remote sensing of the Arctic ice environment, *Proceedings of the seventh International Symposium on Remote Sensing of Environment, 1971*, Ann Arbor, Willow Run Laboratories, Institute of Science and Technology, University of Michigan, Vol. 1, p. 523-61.

- Bogorodsky, V.V., and Tripol'nikov, V.P. (1973). Electromagnetic characteristics of sea ice in the range of 30-400 MHz. *Doklady Akademii Nauk SSSR*, Tom 213, No. 3, p. 577-579.
- Bogorodsky, V.V. and Tripol'nikov, V.P. (1974). Radar sounding of sea ice. *Zhurnal Tekhnicheskoy Fiziki* 44(3), p. 660-662.
- Bradley, G.A. (1971). Remote sensing of ocean winds using a radar scatterometer. University of Kansas, CRES Technical Report, No. 177-22, 201pp.
- Campbell, W.J., Gloersen, P., Nordberg, W. and Wilheit T.T. (1974). Dynamics and morphology of Beaufort Sea ice determined from satellites, aircraft, and drifting stations. In: Bock, P., et. al., ed. *COSPAR. Approaches to Earth survey problems through use of space techniques. Proceedings of the symposium held in Constance, F.R.G., 23-25 May 1973.* Berlin, Akademie-Verlag, p. 311-27.
- Campbell, W.J., Ramseier, R.O., Weeks, W.F. and Gloersen, P. (in press). An integrated approach to the Remote Sensing of Floating Ice. *Proceedings Third Canadian Symposium on Remote Sensing.* (Edmonton, Alberta) October, 1975.
- Campbell, W.J., Weeks, W.F., Ramseier, R.O. and Gloersen, P. (1975). Geophysical studies of floating ice by remote sensing. *Journal of Glaciology* 15(73), p. 305-328.
- Chudobiak, W.J., Gray, R.B., Ramseier, R.O., Makios, V., Vant, M., Davies, J.L. and Katsube, J. (1974). Radar remote sensors for ice thickness and soil moisture measurements. *Proceedings Second Canadian Symposium on Remote Sensing*, (Guelph, Ontario). p. 418-424.
- Cook, J.C. (1960). RF electrical properties of salty ice and frozen earth. *Journal of Geophysical Research* 65(6), p. 1767-1771.
- Finkelstein, M.I., Goloshnev, B.J. and Petrov, A.H. (1970). On the anisotropy of radiowave attenuation of sea ice. *Fizika Atmosfery i Okeana*, 6(3), p. 311-313.
- Fujino, K. (1967). Electrical properties of sea ice. *Physics of Snow and Ice, International Conference on Low Temperature Science*, Sapporo, Japan, p. 633.
- Gloersen, P., Nordberg, W., Schmugge, T.J., Wilheit, T.T. and Campbell, W.J. (1973). Microwave signatures of first-year and multiyear sea ice. *Journal of Geophysical Research* 78(18), p. 3564-72.
- Gloersen, P., Campbell, W.J., Ramseier, R.O., Webster, W.J. and Wilheit, T.T. (1975). Beaufort Sea ice zones by means of microwave imagery. *NASA Technical Report*, X910-75-80 Goddard Space Flight Centre. 17pp.

- Glushkov, V.M. and Komarov, V.B. (1971). Side-looking imaging radar system TOROZ and its application to the study of ice conditions and geological explorations. Proceedings of the seventh International Symposium on Remote Sensing of Environment, 1971, Ann Arbor, Willow Run Laboratories, Institute of Science and Technology, University of Michigan, 1, p. 317.
- Goodman, R.H. (1974). Offshore exploration in the Arctic enhanced by ice measuring techniques. Oilweek, 25(6), p. 10-12.
- Gorbunov, Yu.A. and Losev, S.M. (1974). Use of side-looking radar TOROZ to investigate ice drift. Trudy Arkticheskogo i Antarkticheskogo Nauchno-Issledovatel'skogo Instituta, Tom 316, p. 153-62.
- Guinard, N.W. (1970). The remote sensing of the sea and sea ice. Proceedings of the sixth International Symposium on Remote Sensing of Environment, 1969, Ann Arbor, Willow Run Laboratories, Institute of Science and Technology, University of Michigan, 2, p. 737-54.
- Hibler, W.D. (1975). Characterization of cold regions terrain using airborne laser profilometry. Journal of Glaciology 15(73), p. 329-347.
- Gloersen, P., Chang, T.C., Wilheit, T.T. and Campbell, W.J. (1974). Polar sea ice observations by means of microwave radiometry.
- Hoekstra, P. (1969). Dielectric behaviour of sea ice at X-band frequencies. USA Cold Regions Research and Engineering Laboratory (CRREL), Contract No. MIPRR69-10-G2306, 16pp.
- Hoekstra, P. and Capillino, P. (1971). Dielectric properties of sea and sodium chloride ice at UHF and microwave frequencies. Journal of Geophysical Research, 76(20), p. 4922-4931.
- Johnson, J.D. and Farmer, L.D. (1971). Use of side-looking air-borne radar for sea ice identification. Journal of Geophysical Research, 76(9), p. 2138-55.
- Ketchum, R.D., Jr. and Tooma, S.G., Jr. (1973). Analysis and interpretation of air-borne multifrequency - Side Looking Radar sea ice imagery. Journal of Geophysical Research, 78(3), p. 520-538.
- Morozov, P.T. and Khokhlov, G.P. (in press). Physico-chemical and electrical properties of near edge ice in the Bering Sea, Proceedings U.S.-U.S.S.R. Bering Sea experiment symposium, Leningrad, May 1974.
- Page, D.F. and Ramseier, R.O. (1975). Application of active radar techniques to the study of ice and snow. Journal of Glaciology 15(73), p. 171-191.

- Parashar, S.K. (1973). 13.3 GHz and 400 MHz scatterometer data analysis, mission 126, Point Barrow, Alaska. University of Kansas, CRES Technical Memorandum, No. 177-37, 30pp.
- Parashar, S.K., Biggs, A.W., Fung, A.K. and Moore, R.K. (1975). Investigation of radar discrimination of sea ice. Proceedings of the Ninth International Symposium on Remote Sensing of Environment, 1973, Ann Arbor, Willow Run Laboratories, Environmental Research Institute of Michigan, University of Michigan.
- Ragle, R.H., Blair, R.G. and Persson, L.E. (1964). Ice core studies of Ward Hunt Ice Shelf 1960. *Journal of Glaciology*, 5(37), p. 39-59.
- Ramseier, R.O., Campbell, W.J., Weeks, W.F., Arsenault, L.D. and Wilson, K.L. (1975). Ice dynamics in the Canadian Archipelago and adjacent Arctic Basin as determined by ERTS-1 observations. In: International Symposium on Canada's Continental Margins and Offshore Petroleum Exploration, Calgary, Sept. 1974. Canadian Society of Petroleum Geologists, Mem. 4, p. 853-877.
- Rouse, J.W., Jr. (1969). Arctic ice type identification by radar. *Proceedings of the IEEE*, 57(4), p. 605-611.
- Royer, G.M. (1975). Computer analysis of CW scatterometer data with particular reference to Ryan model 720 system. CRC Report No. 1265, Department of Communications, Ottawa, 65pp.
- Sackinger, W. and Byrd, R. (1972). The dielectric properties of sea ice in the range from 26-40 GHz. IAEE Report 7203, University of Alaska, Fairbanks, Alaska, 88pp.
- Sellmann, P., Weeks, W.F. and Campbell, W.J. (1975). Use of side-looking air-borne radar to determine lake depth on the Alaskan North Slope. Cold Regions Research and Engineering Laboratory Special Report 230, 6pp.
- Vant, M.R., Gray, R.B., Ramseier, R.O. and Makios, V. (1974). Dielectric properties of fresh and sea ice at 10 GHz. *Journal of Applied Physics*, 45(11), p. 4712-4717 and 46(5), p. 2339 (1975).
- Vickers, R.S., Heighway, J. and Gedney, R. (1973). Airborne profiling of ice thickness using a short pulse radar. In "Advanced Concepts and Techniques in the Study of Snow and Ice Resources". (H.S. Santeford and J.L. Smith, eds.). National Academy of Sciences, p. 422-431.
- Wentworth, F.L. and Cohn, M. (1964). Electrical properties of sea ice at .1 to 30 Mc/s. *Radio Science Journal of Research, NBS/USNC-URSI*, 680(6), p. 681-691.

Wilheit, T.T. (1972). The electronically scanning microwave radiometer (ESMR). The Nimbus-5 Users Guide, U.S. Government Printing Office, 1972-735-963/259, p. 59-104.

Wilheit, T.T., Nordberg, W., Blinn, J., Campbell, W.J. and Edgerton, A. (1972). Aircraft measurements of microwave emission from Arctic sea ice. Remote Sensing of Environment 2(3), p. 129-139.

11. FIGURE CAPTIONS

- Figure 1 Summary of dielectric loss data on sea ice.
- Figure 2 The fan beam geometry of the scatterometer antennas. The across-track beamwidth is 3° and the along track beamwidth is 120° .
- Figure 3 Block diagram of the scatterometer system and spectral nature of the signals, into and out of, the scatterometer and combiner.
- Figure 4 Power Spectrum obtained by playing back a cross-polarized signal through a spectrum analyser.
- Figure 5 Block diagram of the system used for analog processing of the scatterometer data.
- Figure 6 Empirical model for ice dielectric constant first-year sea ice, of salinity = 5.0‰ and density = 0.92 g cm^{-3} .
- Figure 7 Empirical model for the dielectric constant of first-year sea ice, of salinity = 10.0‰ and density = 0.92 g cm^{-3} .
- Figure 8 Empirical model for the dielectric constant of first-year sea ice, of salinity = 15.0‰ density = 0.92 g cm^{-3} .
- Figure 9 Empirical model of the dielectric loss in db/m of first-year sea ice, of salinity = 5‰ and density = 0.92 g cm^{-3} .
- Figure 10 Empirical model for the dielectric loss in db/m of first-year sea ice, of salinity = 10‰ and density = 0.92 g cm^{-3} .
- Figure 11 Empirical model for the dielectric loss in db/m of first-year sea ice, of salinity = 15‰ and density = 0.92 g cm^{-3} .
- Figure 12 13.3 GHz scatterometer and 37 GHz radiometer results at the AIDJEX site. Trace 1 is cross-polarized and Trace 2 is like-polarized

- backscattering observed at 45° fore of nadir. Trace 3 is variation in radiometer brightness temperatures.
- Figure 13 Beaufort Sea offshore region showing flight lines of CCRS C-47 and SLR mosaic lines of DND Argus. The approximate limit of shorefast ice is shown.
- Figure 14 Variation in microwave backscatter measured at 45° to nadir for the southern part of line 3.
- Figure 15 Comparison of like-polarized (A) and cross-polarized (B) backscatter from the southern part of line 3, at 45° to nadir.
- Figure 16 Variation in cross-polarized backscatter for angles between 15° and 55° to nadir.
- Figure 17 Variation in like-polarized backscatter for angles between 5° and 55° to nadir.
- Figure 18 Comparison of like- and cross-polarized returns measured at 5° to nadir.
- Figure 19 SLR image of AIDJEX area, April 1975. Light area indicate low returns and dark areas indicate high returns.
- Figure 20 SLR image of Beaufort Sea, April 1975, with scatterometer track A - B (shown in Figure 14) superimposed.
- Figure 21 SLR image of Beaufort Sea offshore area near Mackenzie Delta, April 1975.
- Figure 22 SLR images of Mackenzie Delta channels, April 1975, taken at 90° to each other.
- Figure 23 Linear interpolation to resolve percentage of open water in areas of first-year sea ice (dashed lines after Gloersen et al 1975) and in areas of multiyear sea ice (solid line, crosses denote mapped percentage classes).
- Figure 24 Linear interpolation to resolve percentages of multiyear ice and first-year ice (crosses denote mapped percentage classes).
- Figure 25 Percentage of open water, remainder is multi-year ice, 9 - 11 September 1973.

- Figure 26 Percentage of open water, remainder is multi-year ice,
7 - 9 October 1975.
- Figure 27 Percentage of open water, remainder is multi-year ice,
7 - 9 September 1974.
- Figure 28 Percentage of open water, remainder is multi-year ice,
7 - 9 October 1974.
- Figure 29 Minimum extent of pack ice in September, 1973 and 1974.
- Figure 30 Percentage of first-year ice, remainder is multi-year ice,
20 - 22 December 1972.
- Figure 31 Percentage of first-year ice, remainder is multi-year ice,
15 - 17 January 1973.
- Figure 32 Percentage of first-year ice, remainder is multi-year ice,
14 - 16 February 1973.
- Figure 33 Percentage of first-year ice, remainder is multi-year ice,
10 - 12 December, 1973.
- Figure 34 Percentage of first-year ice, remainder is multi-year ice,
10 - 12 January 1974.
- Figure 35 Percentage of first-year ice, remainder is multi-year ice,
6 - 8 February 1974.
- Figure 36 Percentage of first-year ice, remainder is multi-year ice,
11 - 13 March 1974.
- Figure 37 Percentage of first-year ice, remainder is multi-year ice,
6 - 8 December 1974.
- Figure 38 Percentage of first-year ice, remainder is multi-year ice,
5 - 7 January 1975.
- Figure 39 Percentage of first-year ice, remainder is multi-year ice,
4 - 6 February 1975.
- Figure 40 Percentage of first-year ice, remainder is multi-year ice,
6 - 8 March 1975.
- Figure 41 Maximum extent of multi-year ice in February 1973 - 1975.

APPENDIX

- Figure A1 Study area for ESMR data.
- Figure A2-A26 Monthly maps of brightness temperature contours, December 1972
to April 1975.

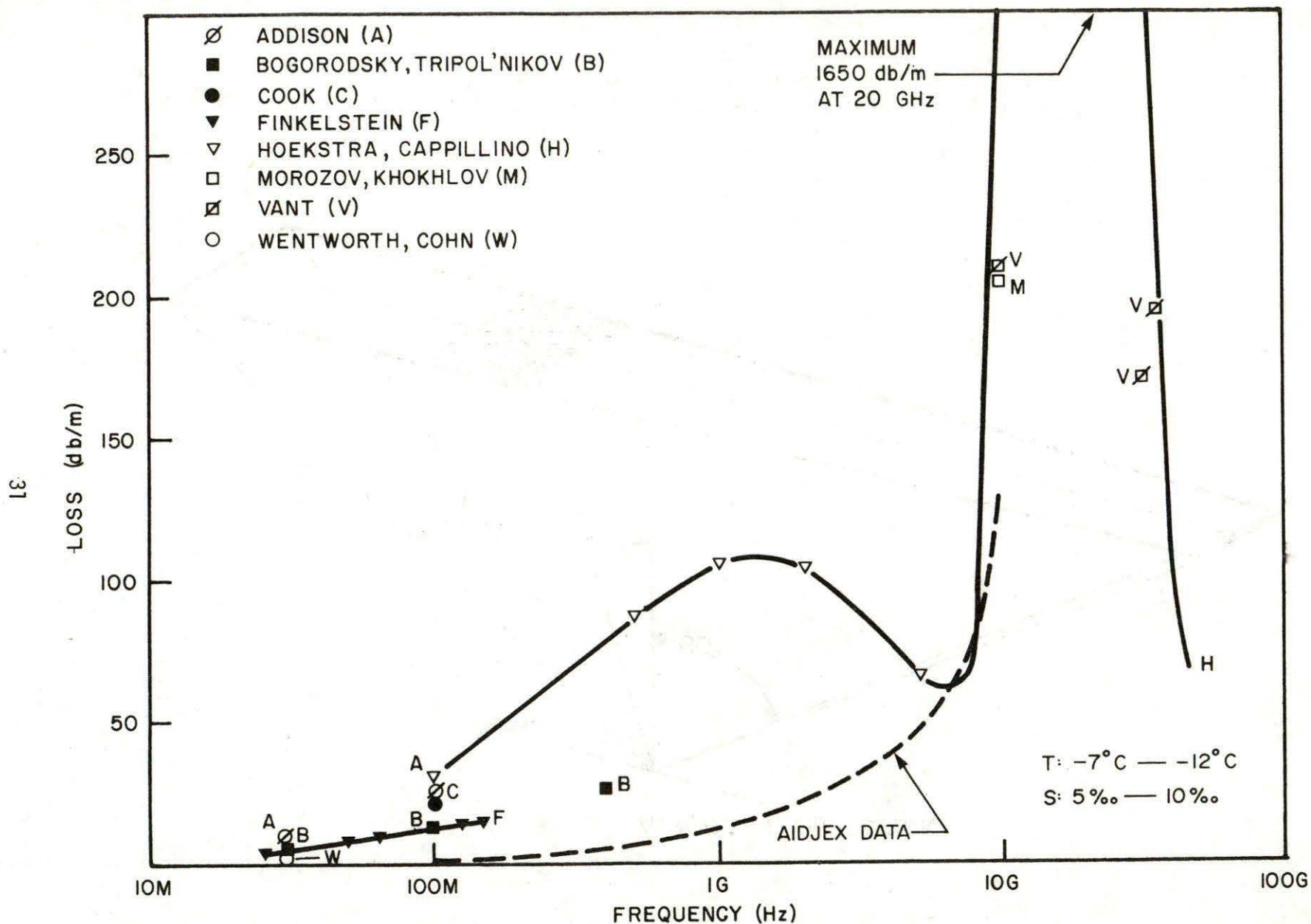


Figure 1. Summary of dielectric loss data on sea ice.

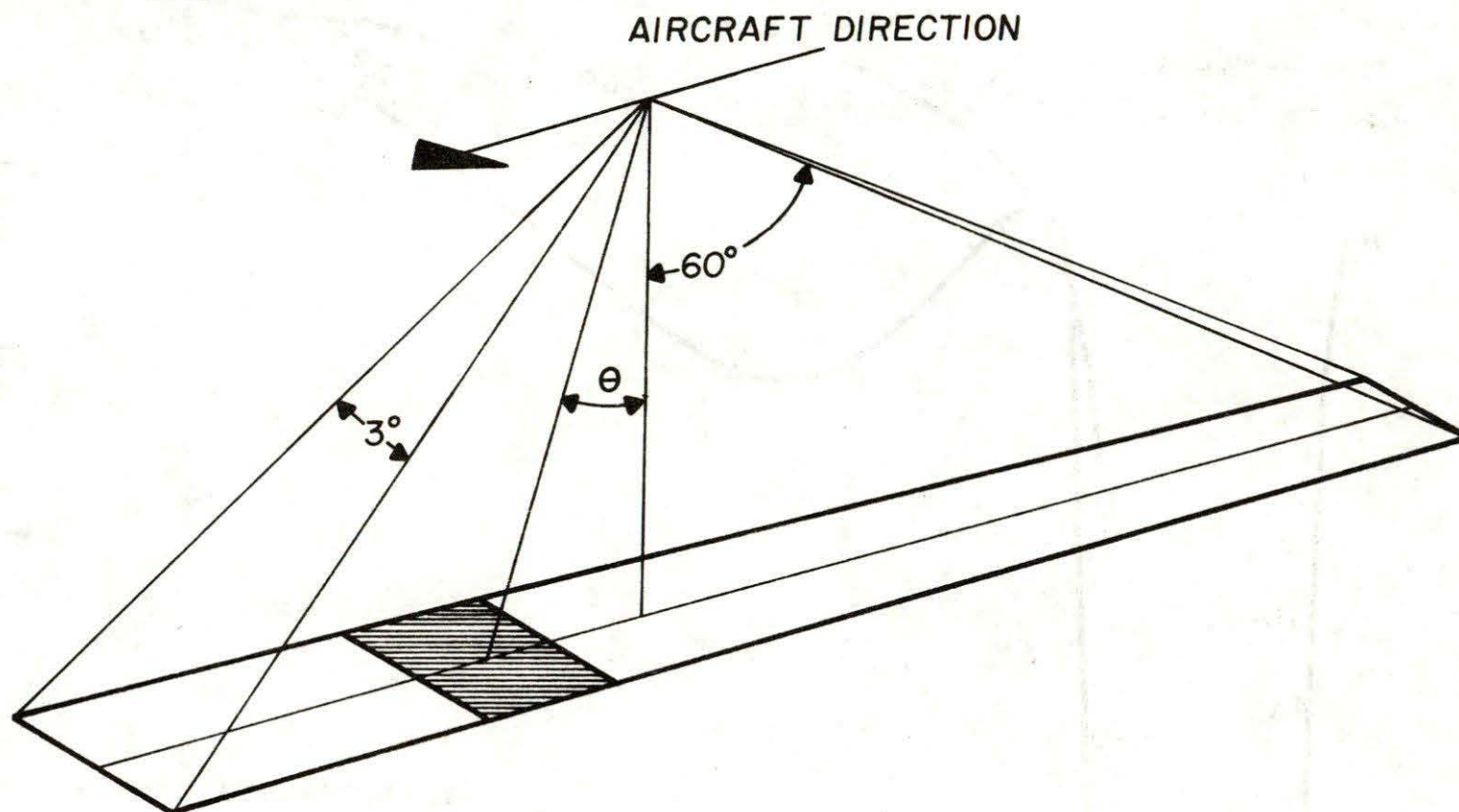


Figure 2. The fan beam geometry of the scatterometer antennas. The across-track beamwidth is 3° and the along track beamwidth is 120° .

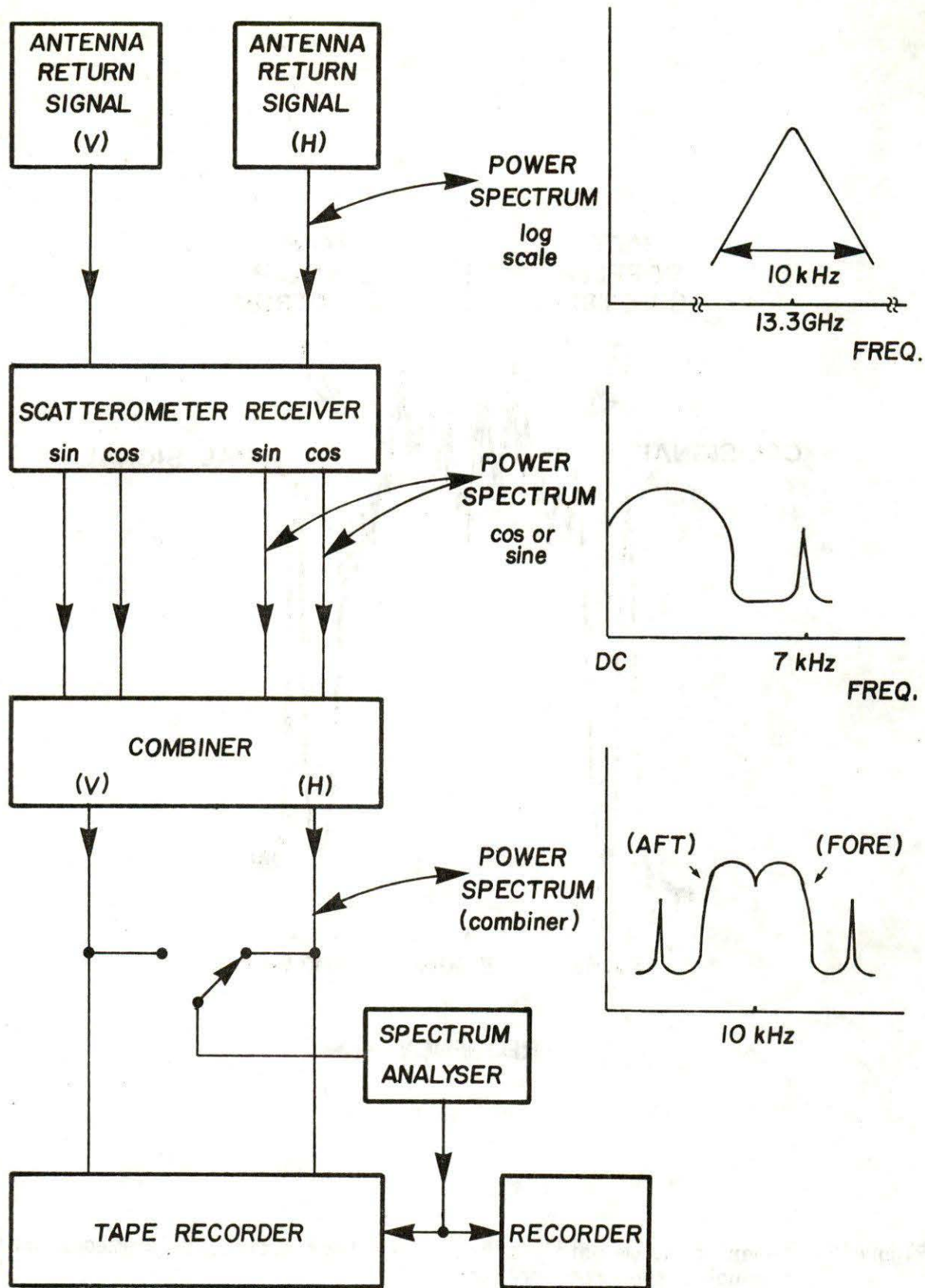


Figure 3. Block diagram of the scatterometer system and spectral nature of the signals, into and out of, the scatterometer and combiner.

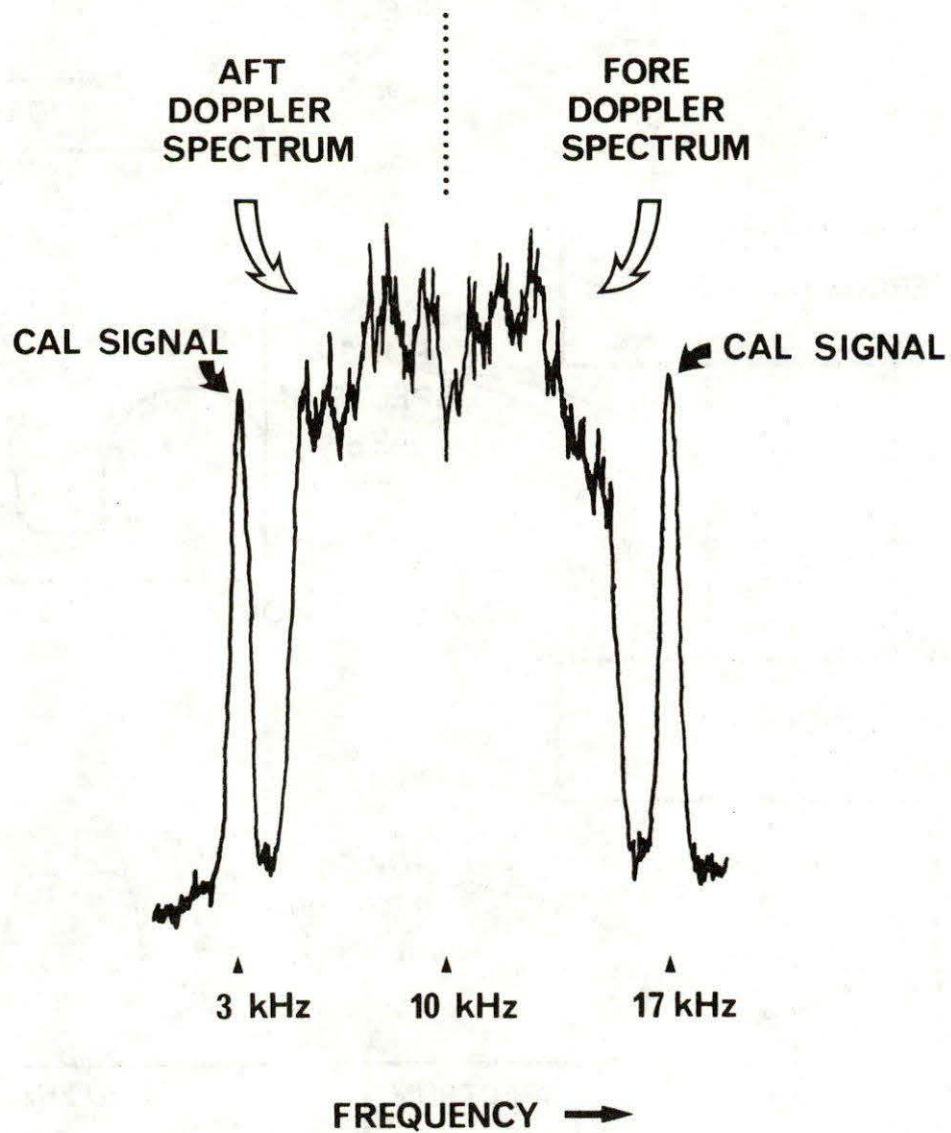


Figure 4. Power Spectrum obtained by playing back a cross-polarized signal through a spectrum analyser.

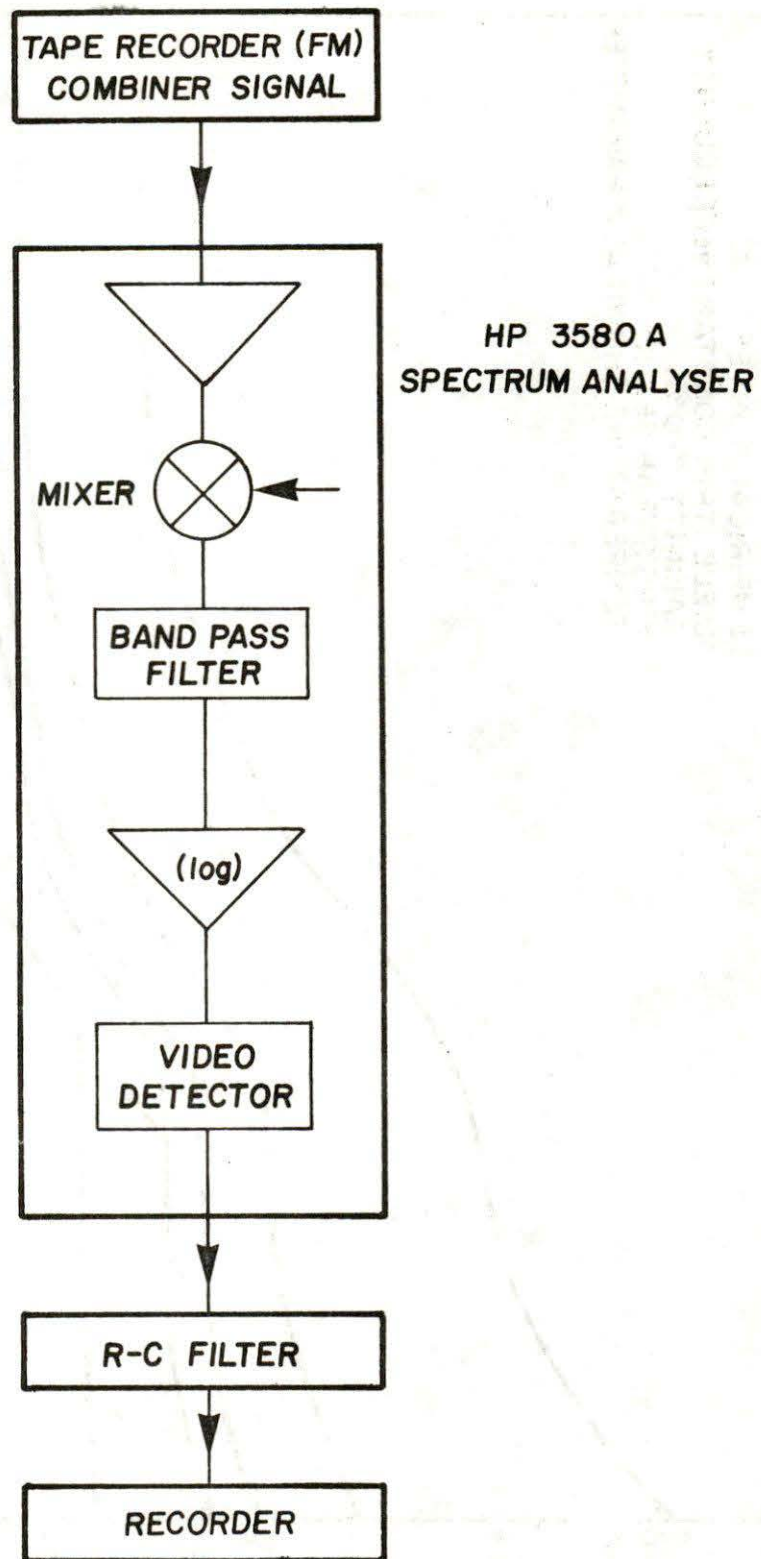


Figure 5. Block diagram of the system used for analog processing of the scatterometer data.

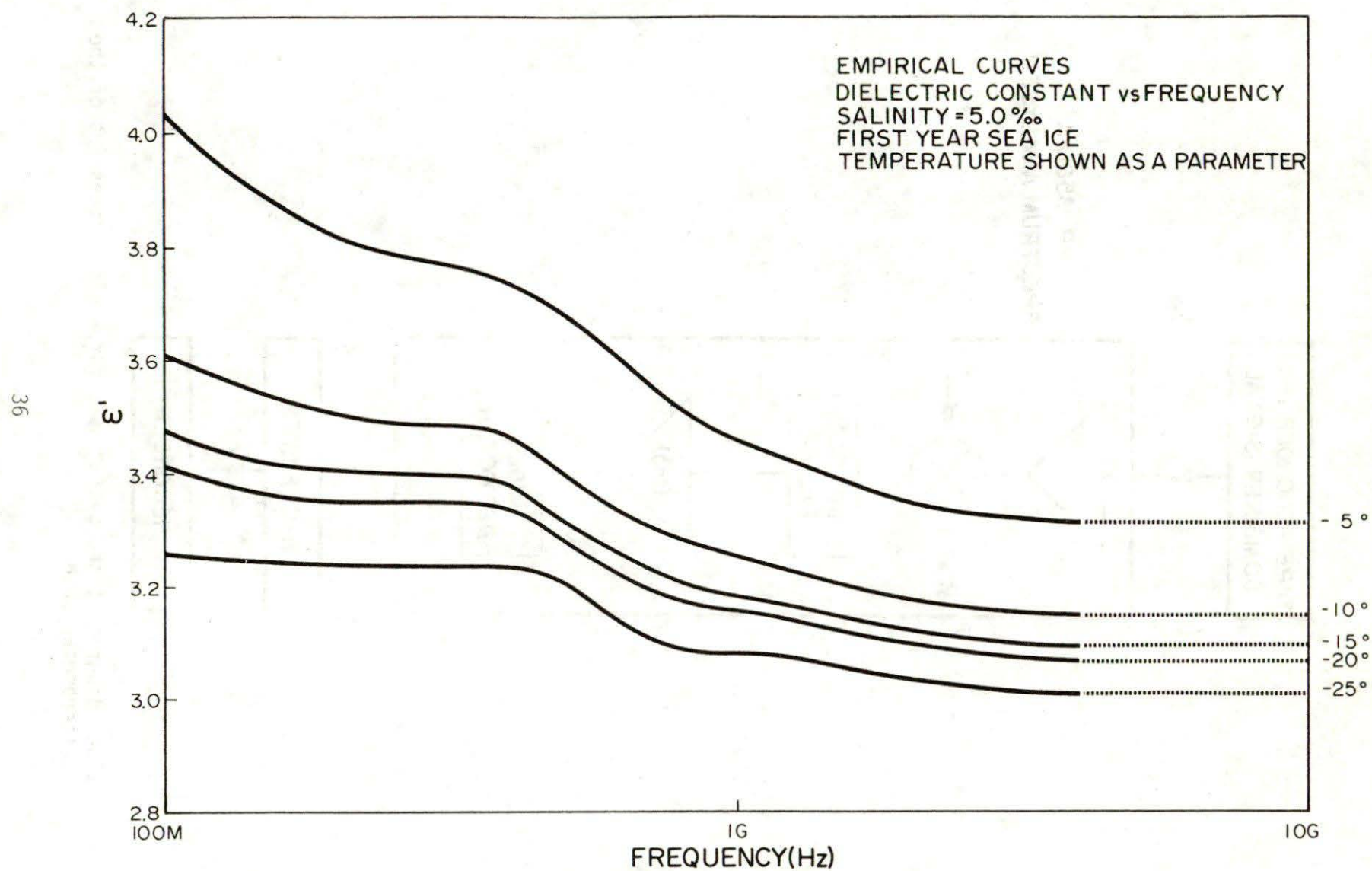


Figure 6. Empirical model for ice dielectric constant; first-year sea ice, of salinity = 5.0‰ and density = 0.92 g cm⁻³.

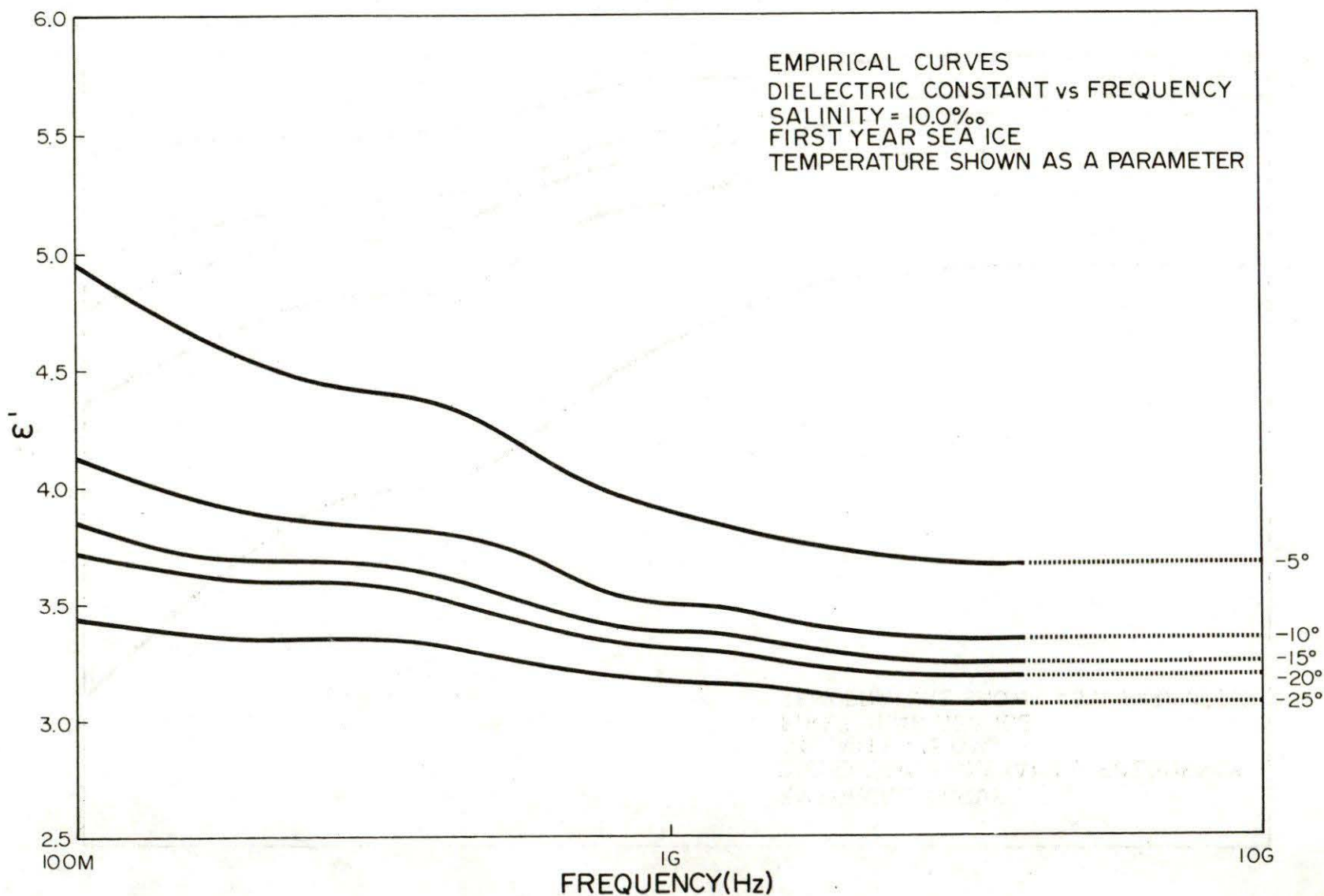


Figure 7. Empirical model for the dielectric constant of first-year sea ice, of salinity = 10.0‰ and density = 0.92 g cm^{-3} .

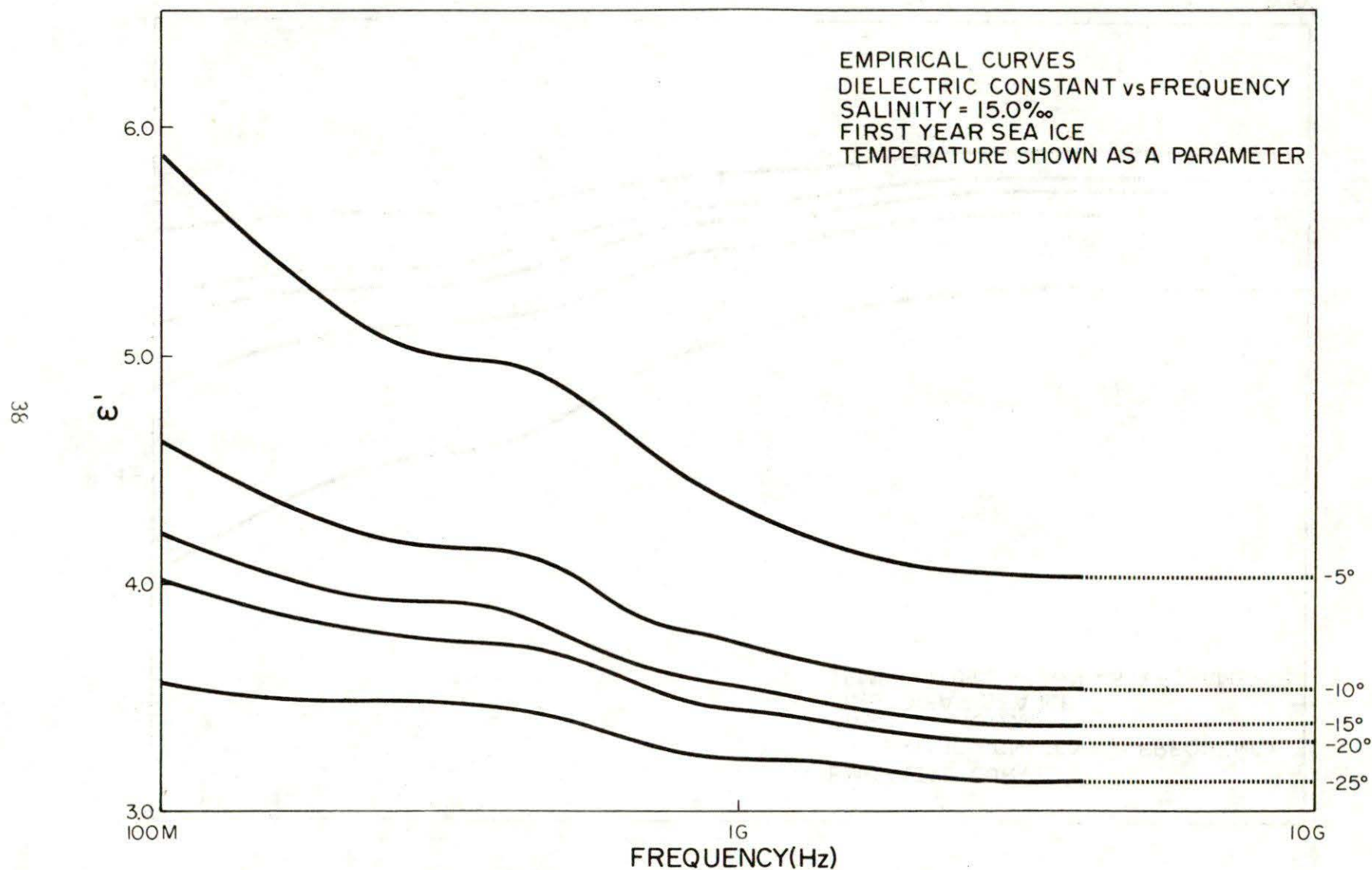


Figure 8. Empirical model for the dielectric constant of first-year sea ice, of salinity = 15.0‰ and density = 0.92 g cm⁻³.

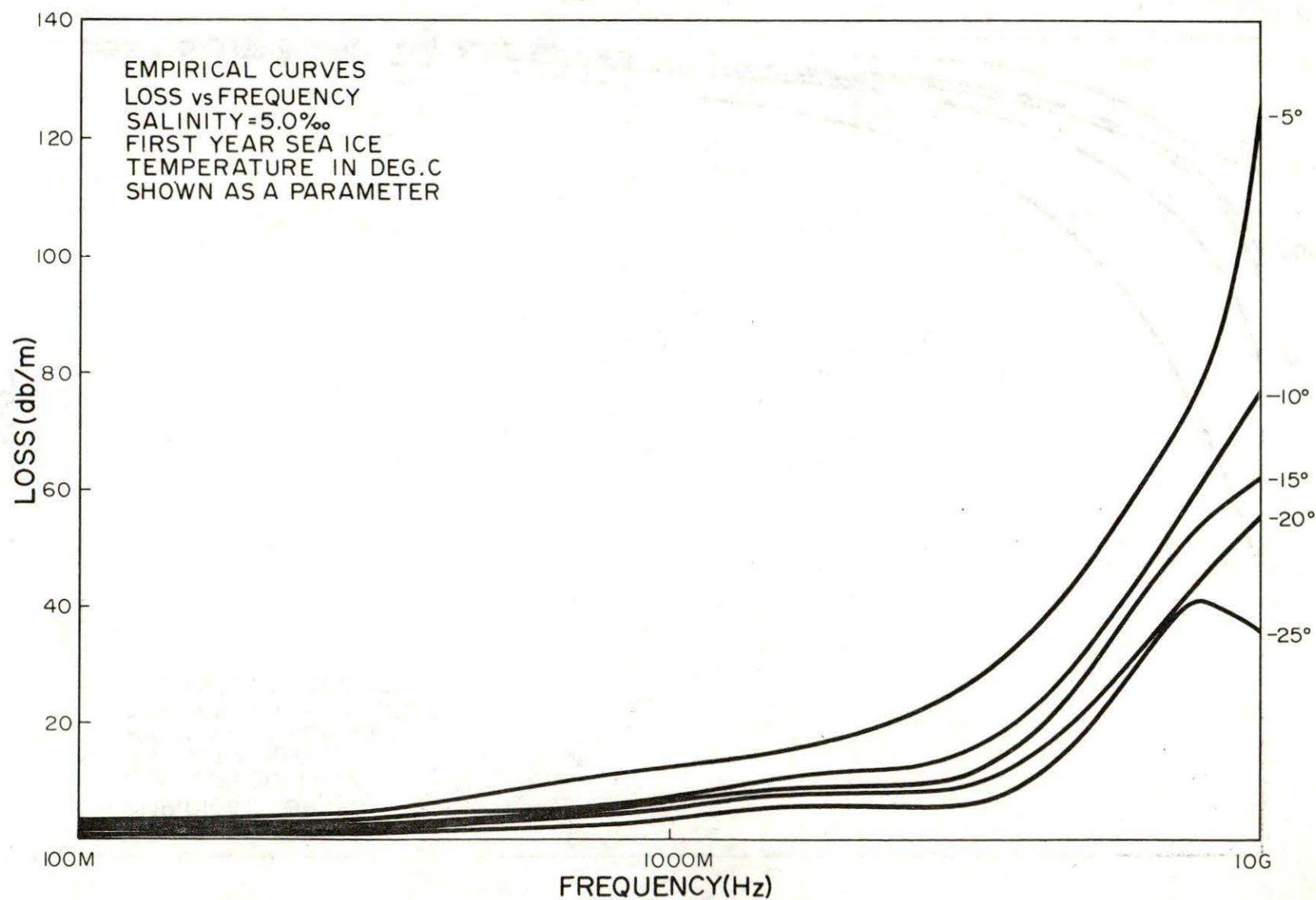


Figure 9. Empirical model for the dielectric loss in db/m of first-year sea ice, of salinity = 5.0‰ and density = 0.92 g cm⁻³.

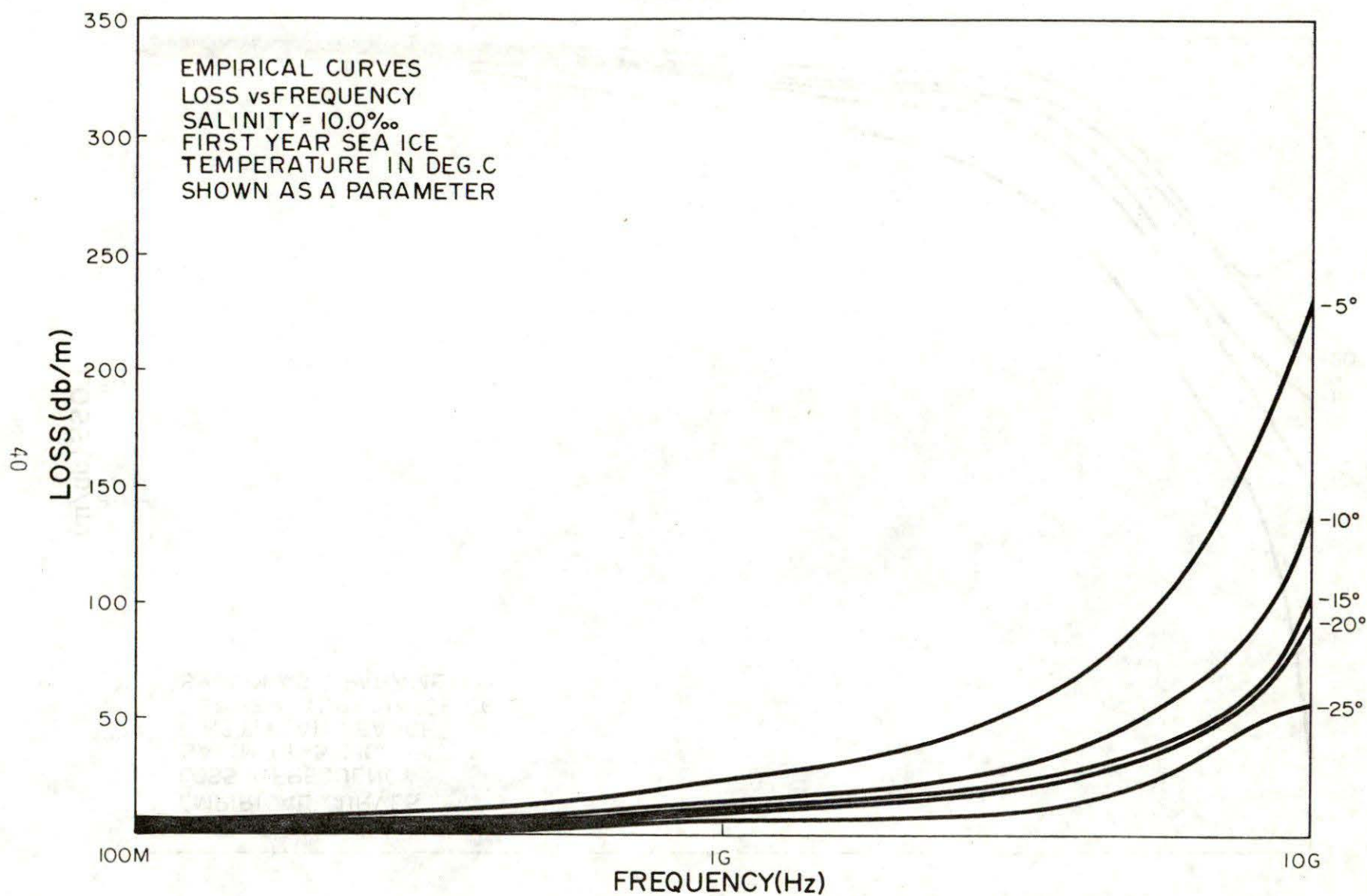


Figure 10. Empirical model for the dielectric loss in db/m of first-year sea ice, of salinity = 10.0‰ and density = 0.92 g cm⁻³.

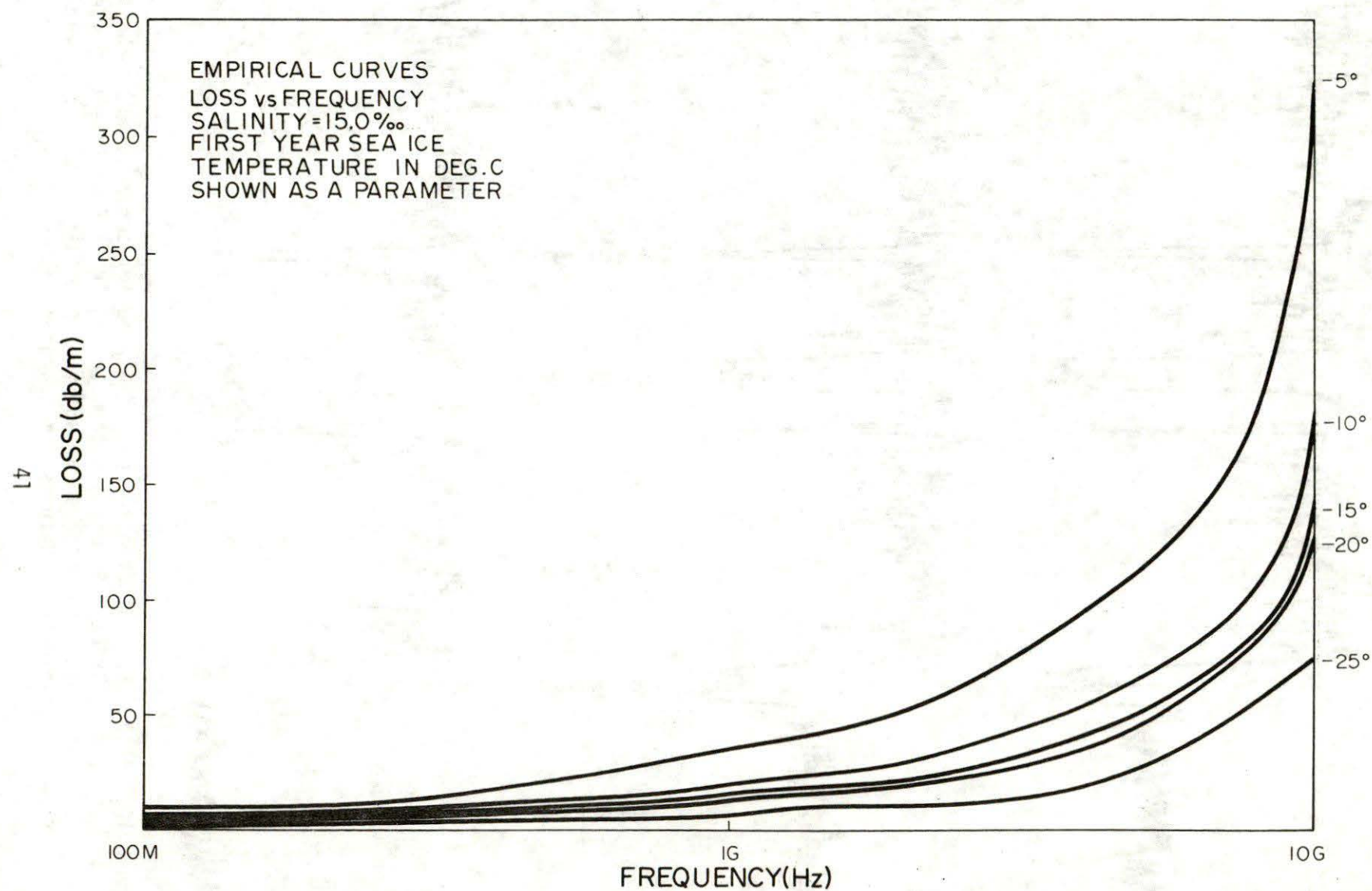


Figure 11. Empirical model for the dielectric loss in db/m of first-year sea ice, of salinity = 15.0‰ and density = 0.92 g cm⁻³.

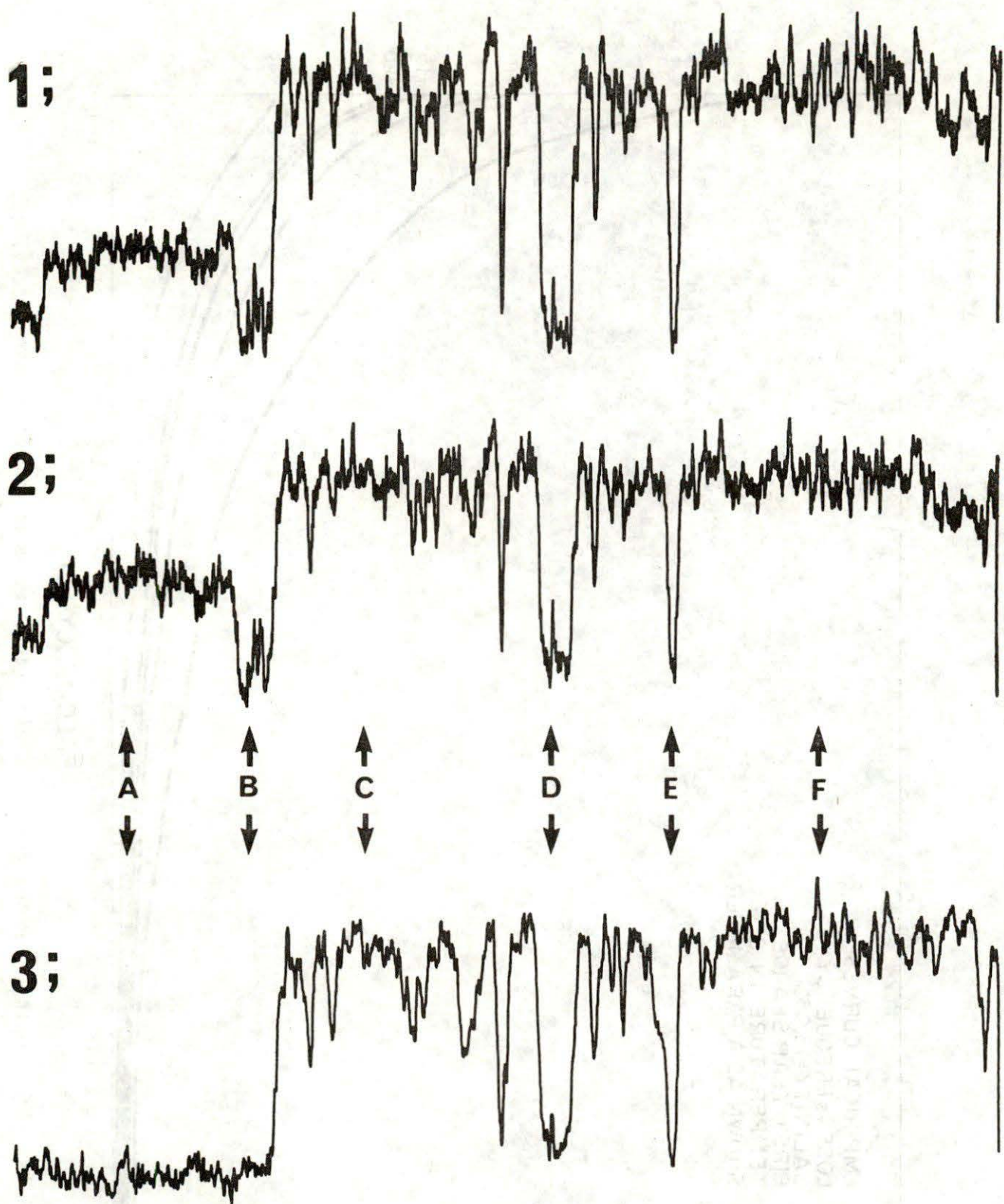


Figure 12. 13.3 GHz scatterometer and 37 GHz radiometer results at the AIDJEX site. Trace 1 is cross-polarized and Trace 2 is like-polarized backscattering observed at 45° fore of nadir. Trace 3 is variation in radiometer brightness temperatures.

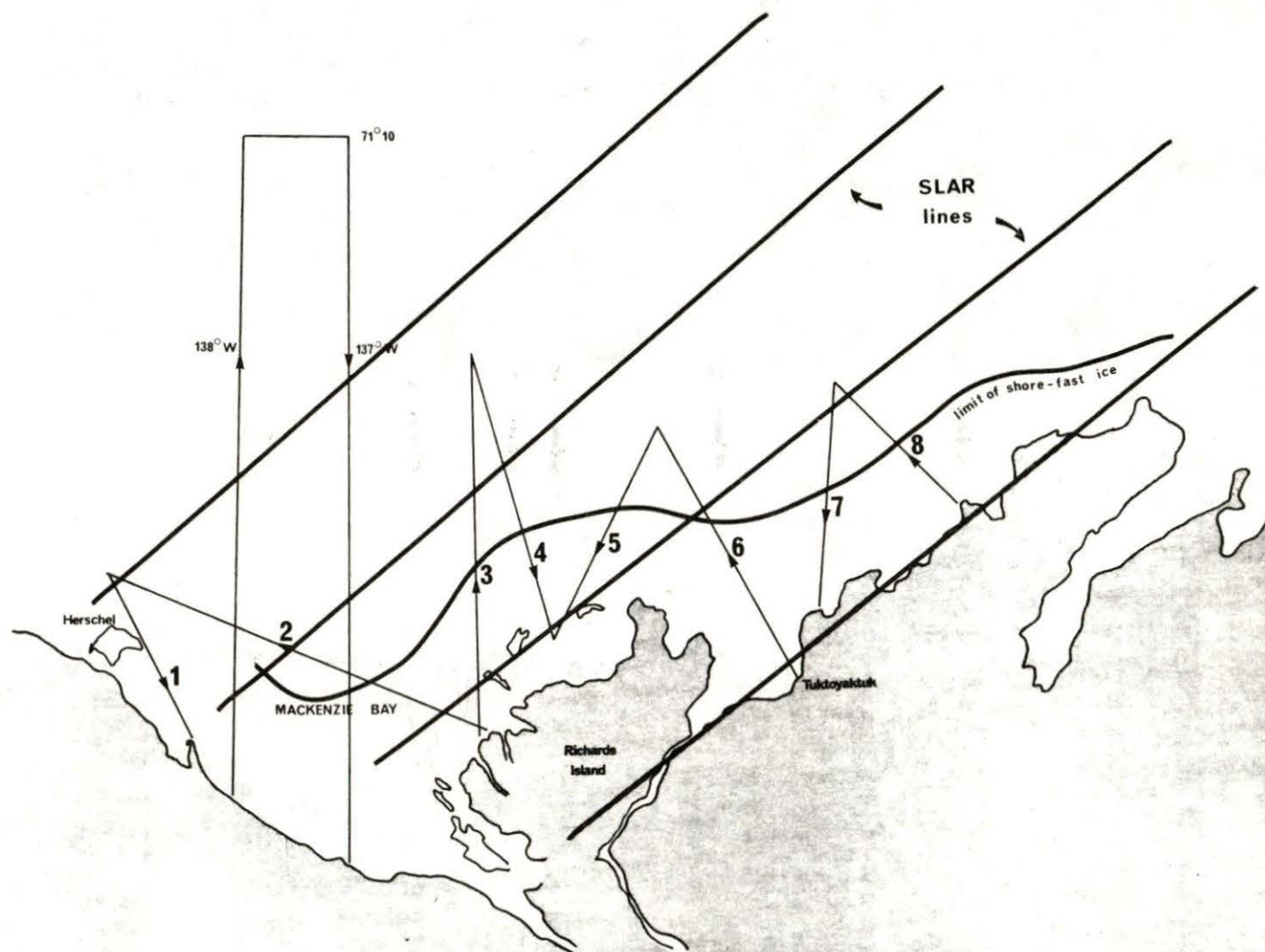


Figure 13. Beaufort Sea offshore region showing flight lines of CCRS C-47 and SLR mosaic lines of DND Argus. The approximate limit of shorefast ice is shown.

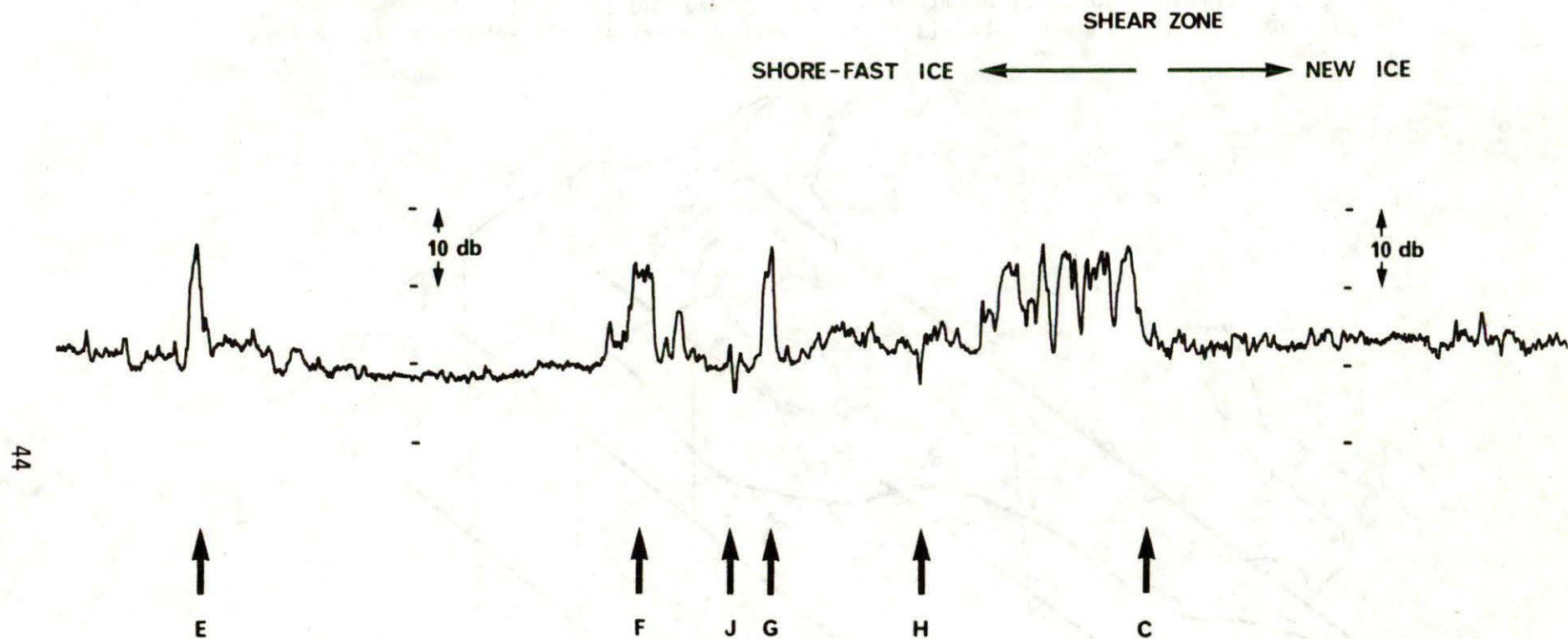


Figure 14. Variation in microwave backscatter measured at 45° to nadir for the southern part of line 3.

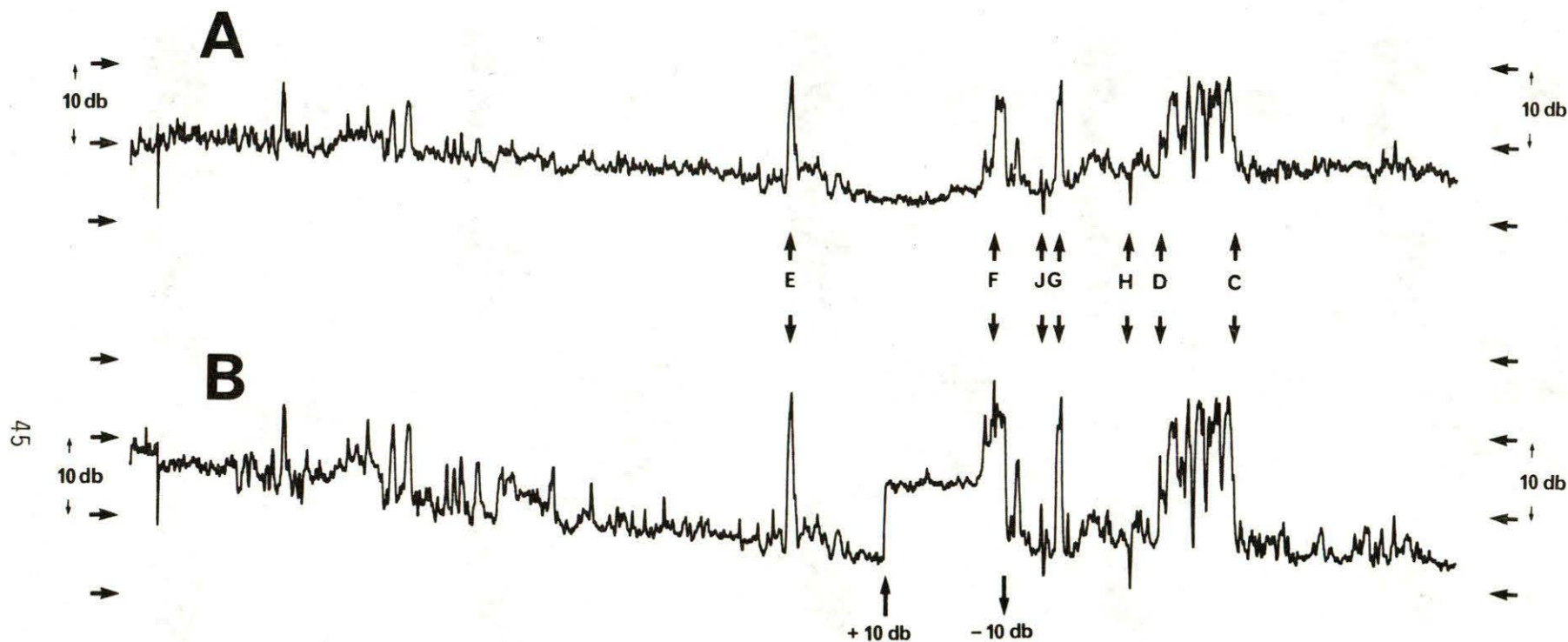


Figure 15. Comparison of like-polarized (A) and cross-polarized (B) backscatter from the southern part of line 3, at 45° to nadir.

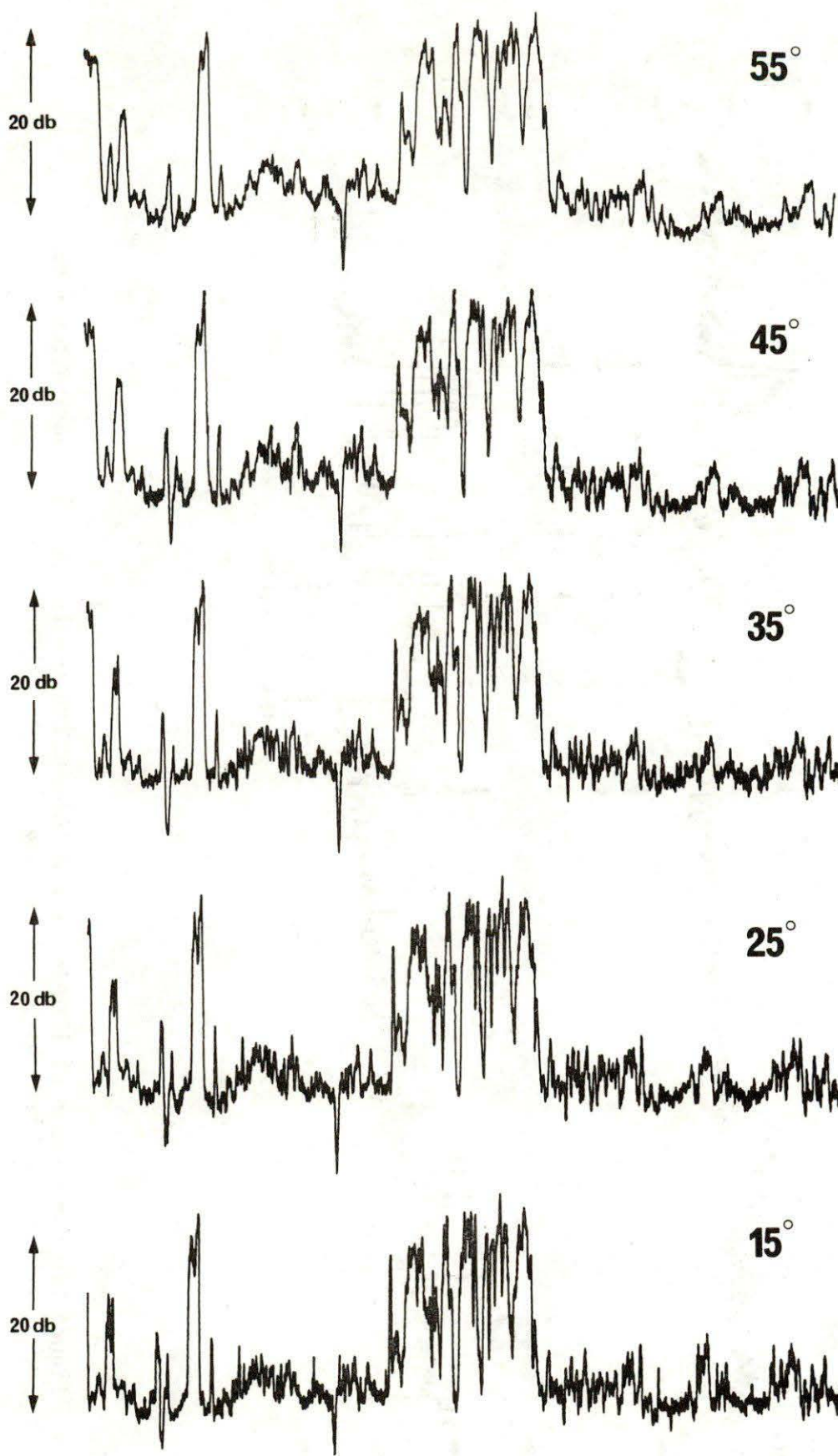


Figure 16. Variation in cross-polarized backscatter for angles between 15° and 55° to nadir.

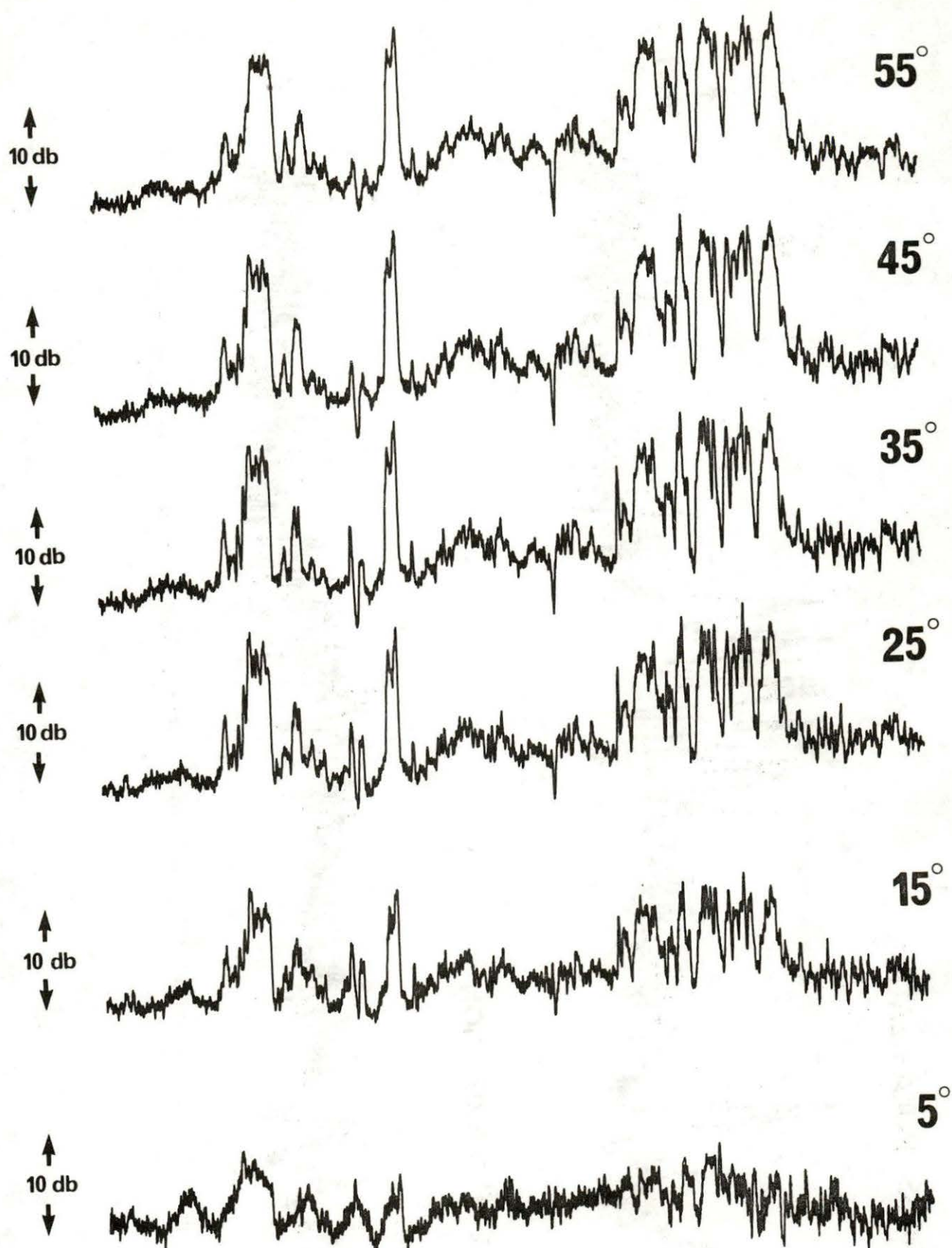


Figure 17. Variation in like-polarized backscatter for angles between 5° and 55° to nadir.

CROSS POLARIZATION



LIKE POLARIZATION

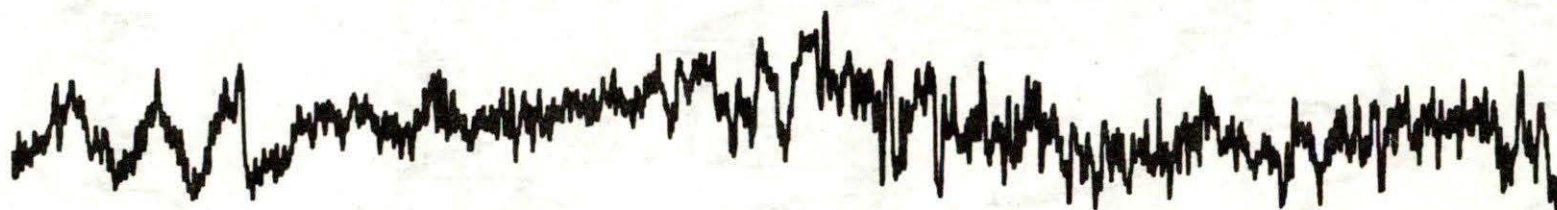


Figure 18. Comparison of like- and cross-polarized returns measured at 5° to nadir.



Figure 19. SLR image of AIDJEX area, April 1975. Light areas indicate low returns and dark areas indicate high returns.

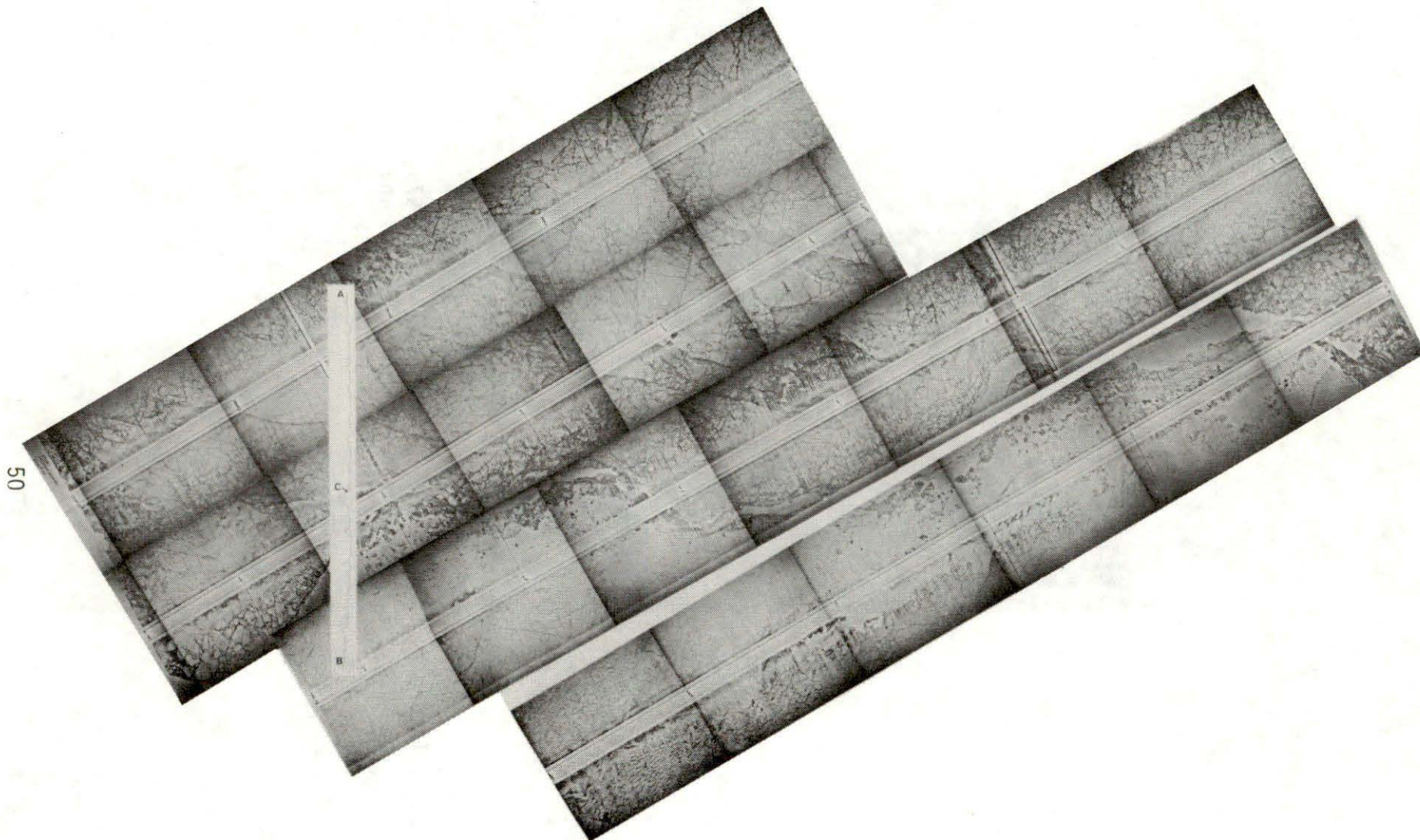


Figure 20. SLR image of Beaufort Sea, April 1975, with scatterometer track A - B (shown in Figure 14) superimposed.

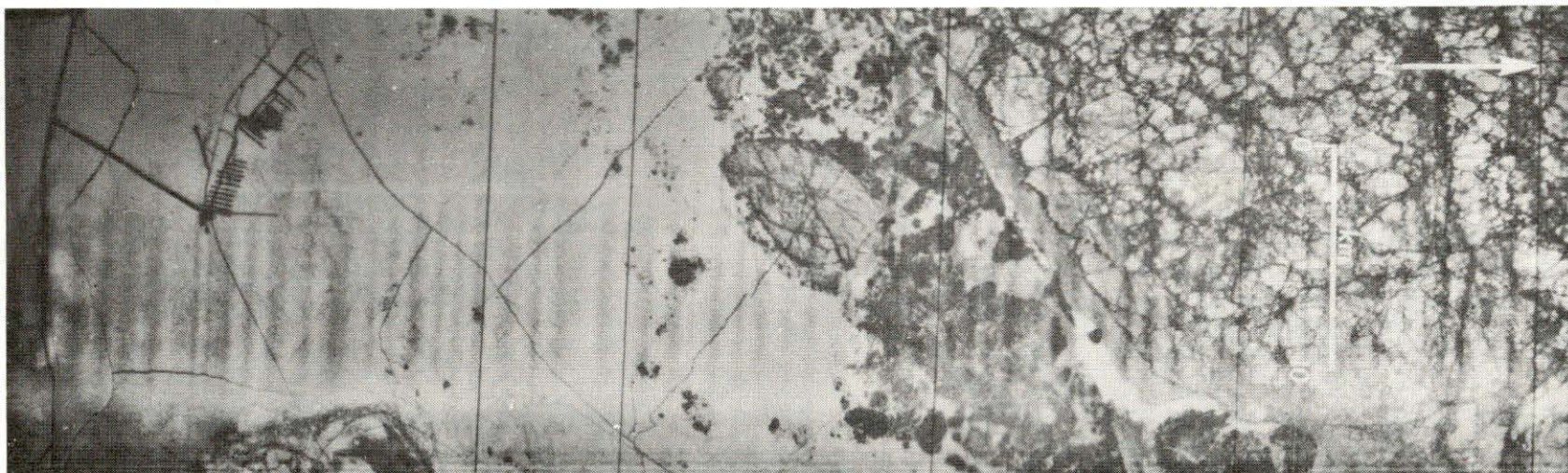


Figure 21. SLR image of Beaufort Sea offshore area near Mackenzie Delta, April 1975.

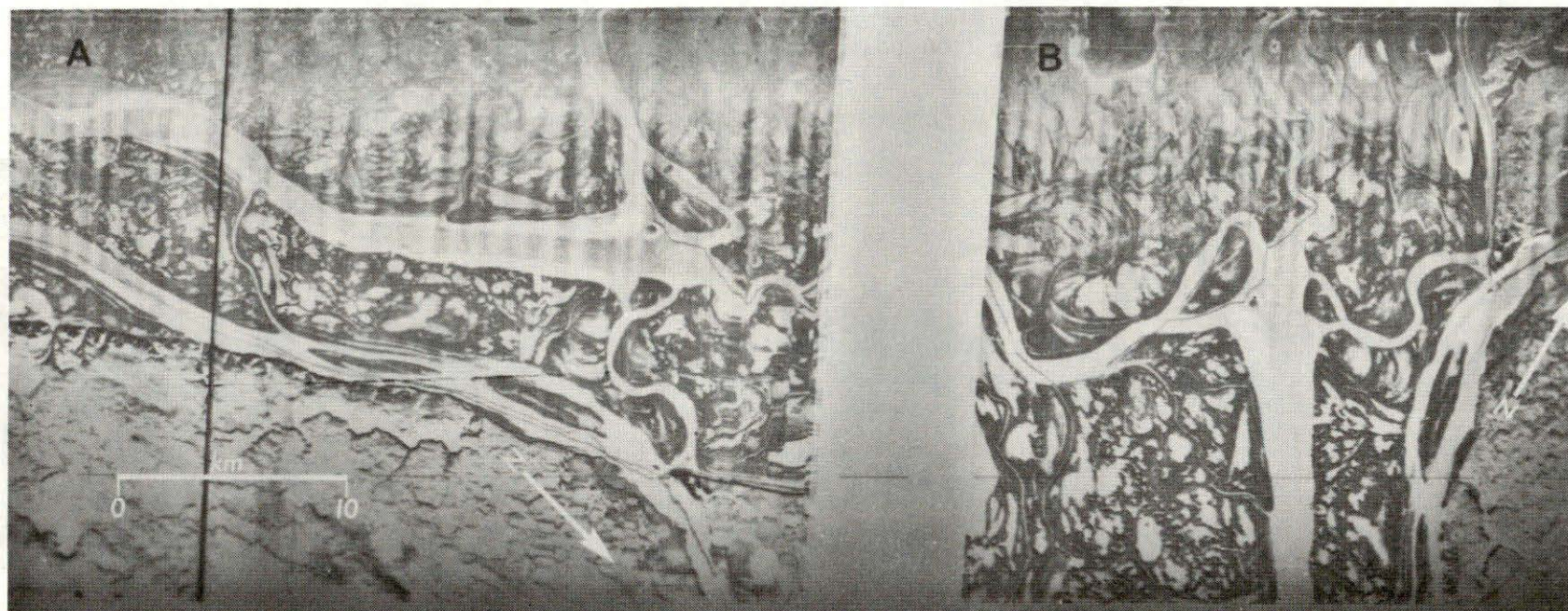


Figure 22. SLR images of Mackenzie Delta channels, April 1975, taken at 90° to each other.

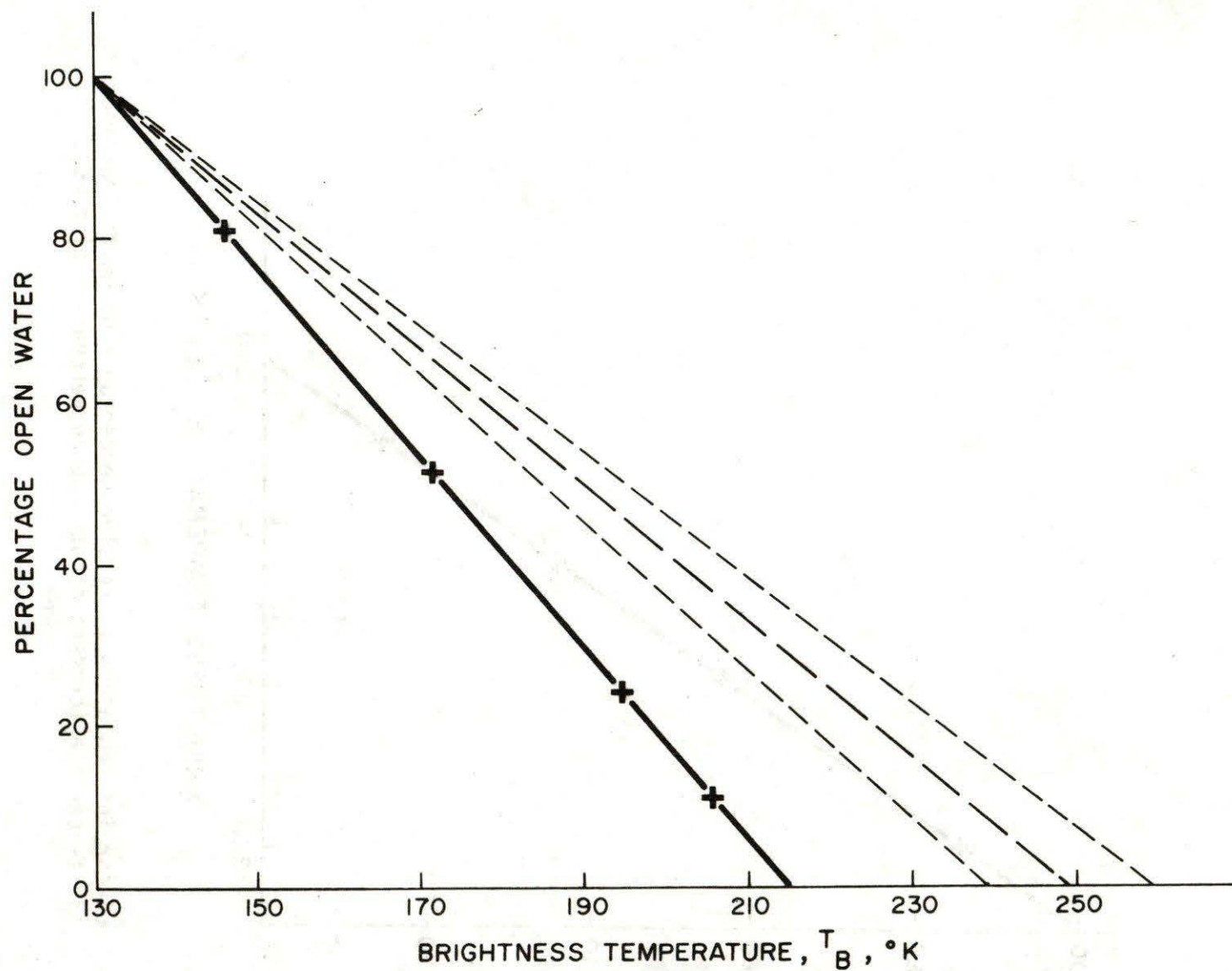


Figure 23. Linear interpolation to resolve percentage of open water in areas of first-year sea ice (dashed lines after Gloersen et al 1975) and in areas of multi-year sea ice (solid line, crosses denote mapped percentage classes).

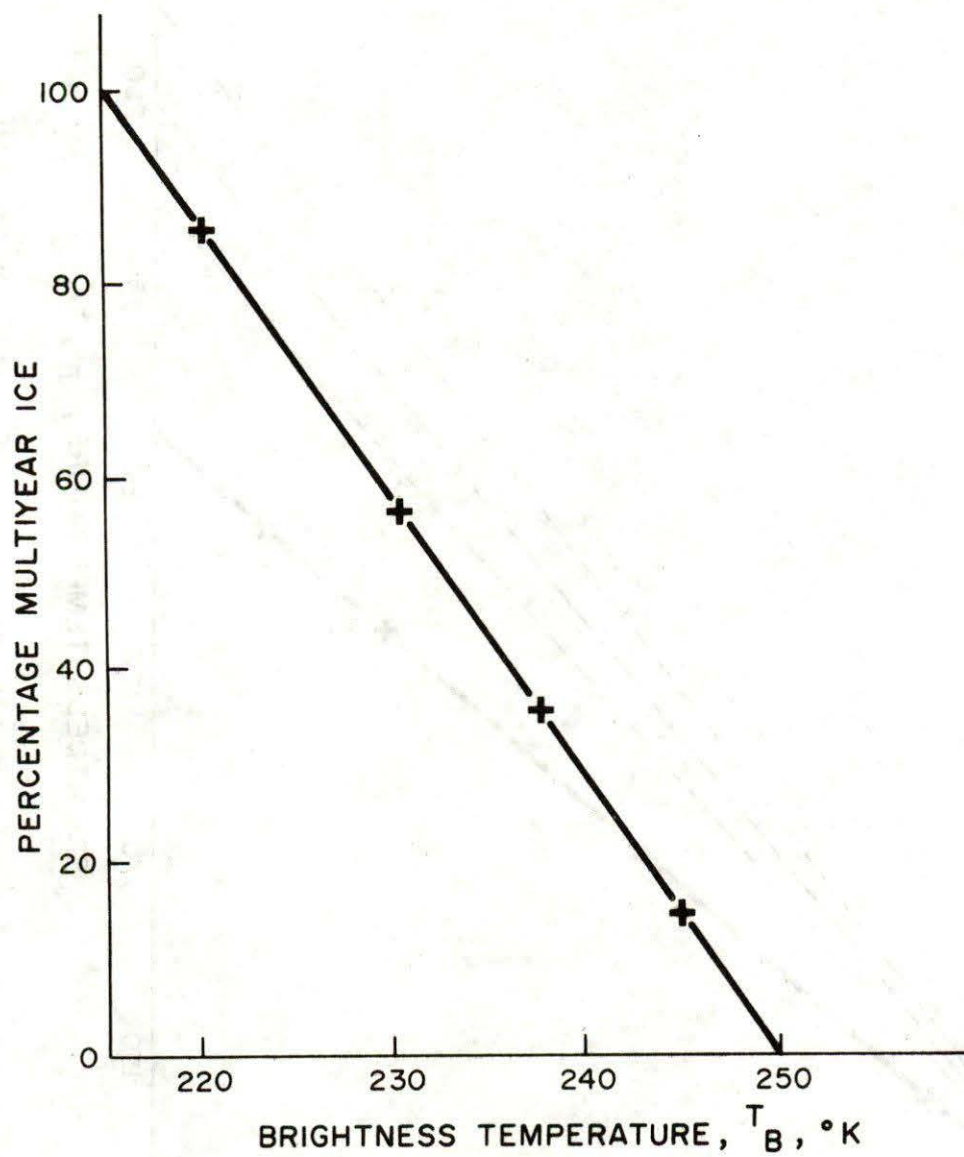


Figure 24. Linear interpolation to resolve percentages of multi-year and first-year ice (crosses denote mapped percentage classes).

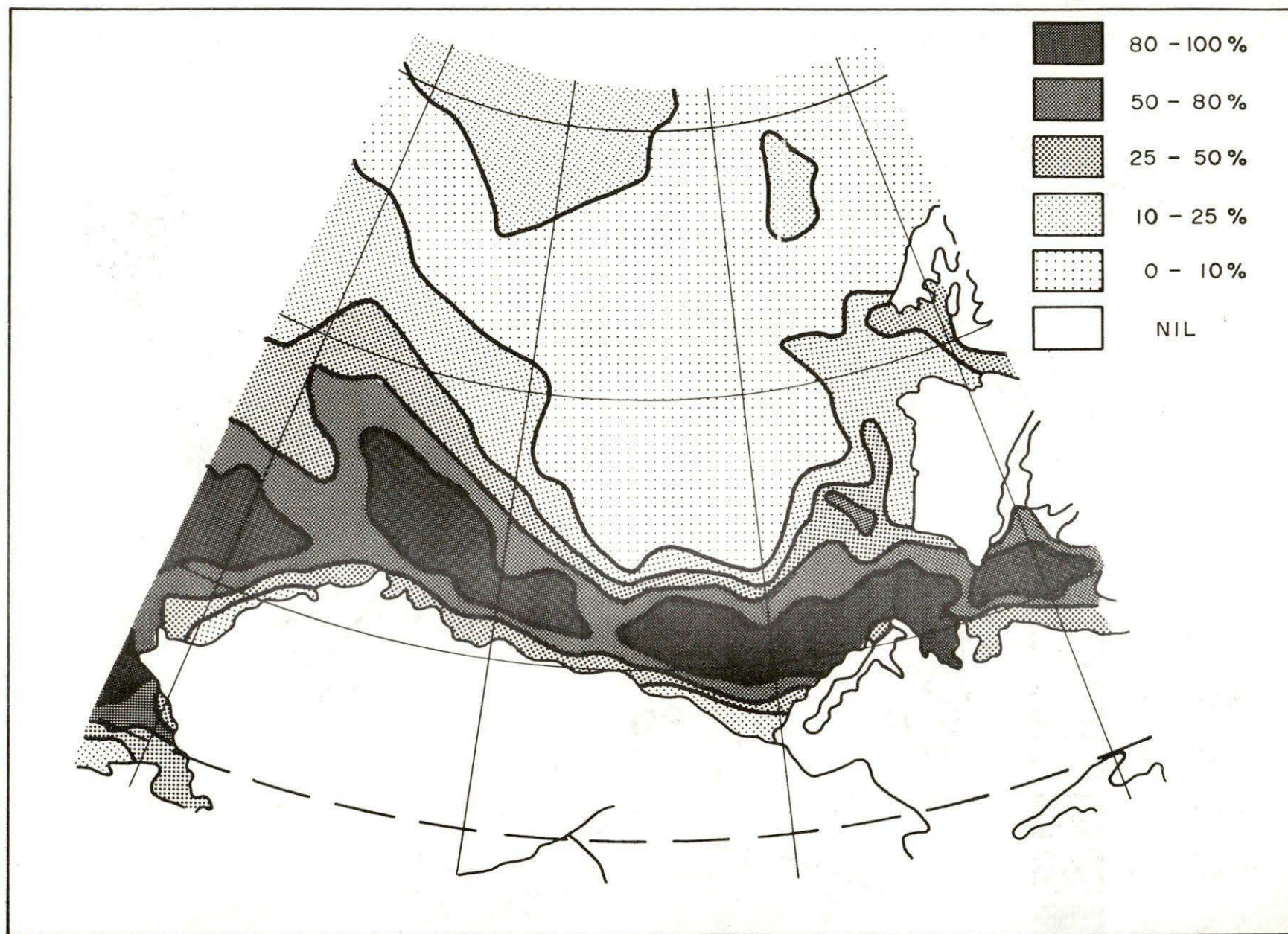


Figure 25. Percentage of open water, remainder is multi-year ice, 9 - 11 September 1973.

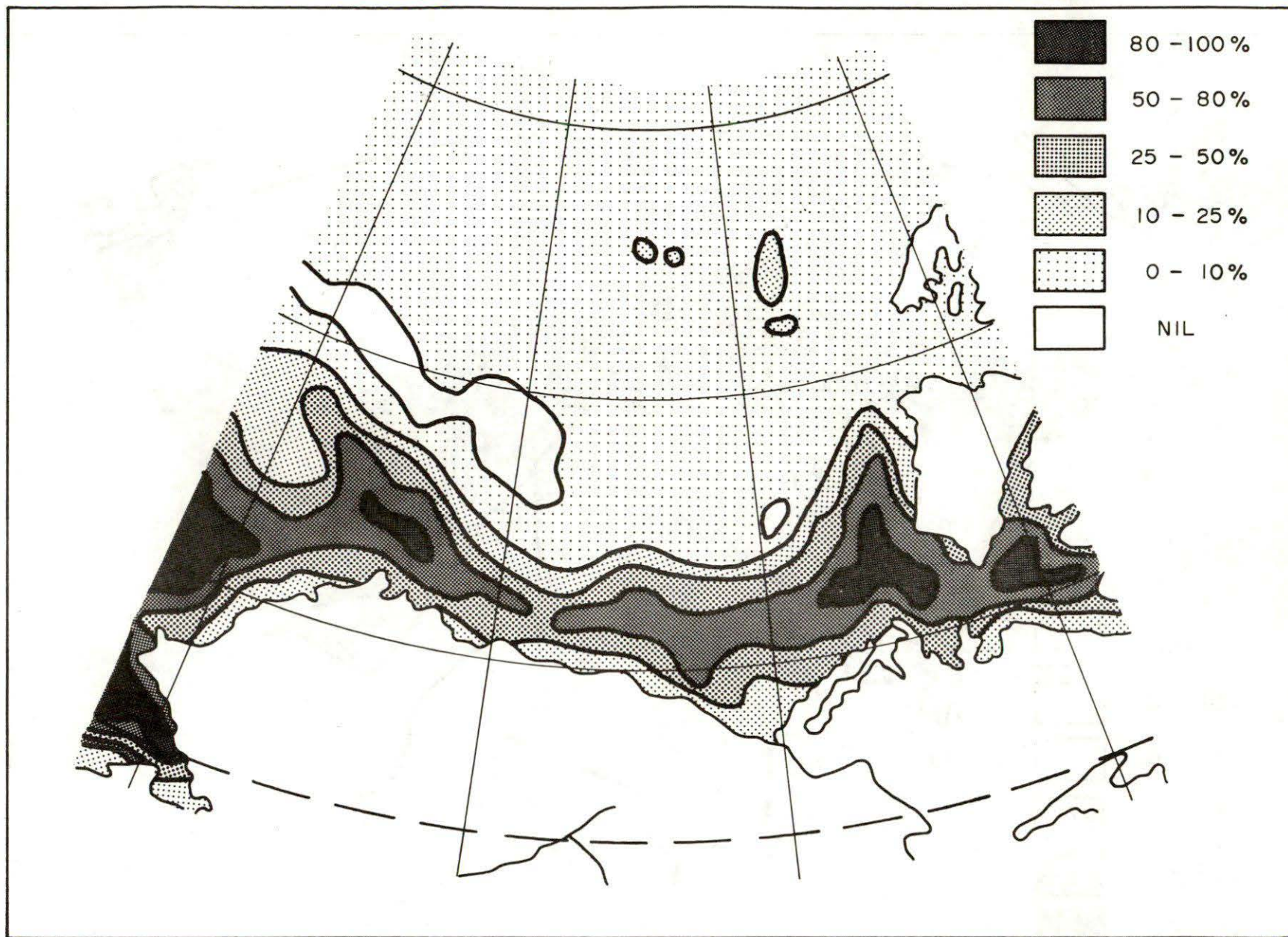


Figure 26. Percentage of open water, remainder is multi-year ice, 7 - 9 October 1975.

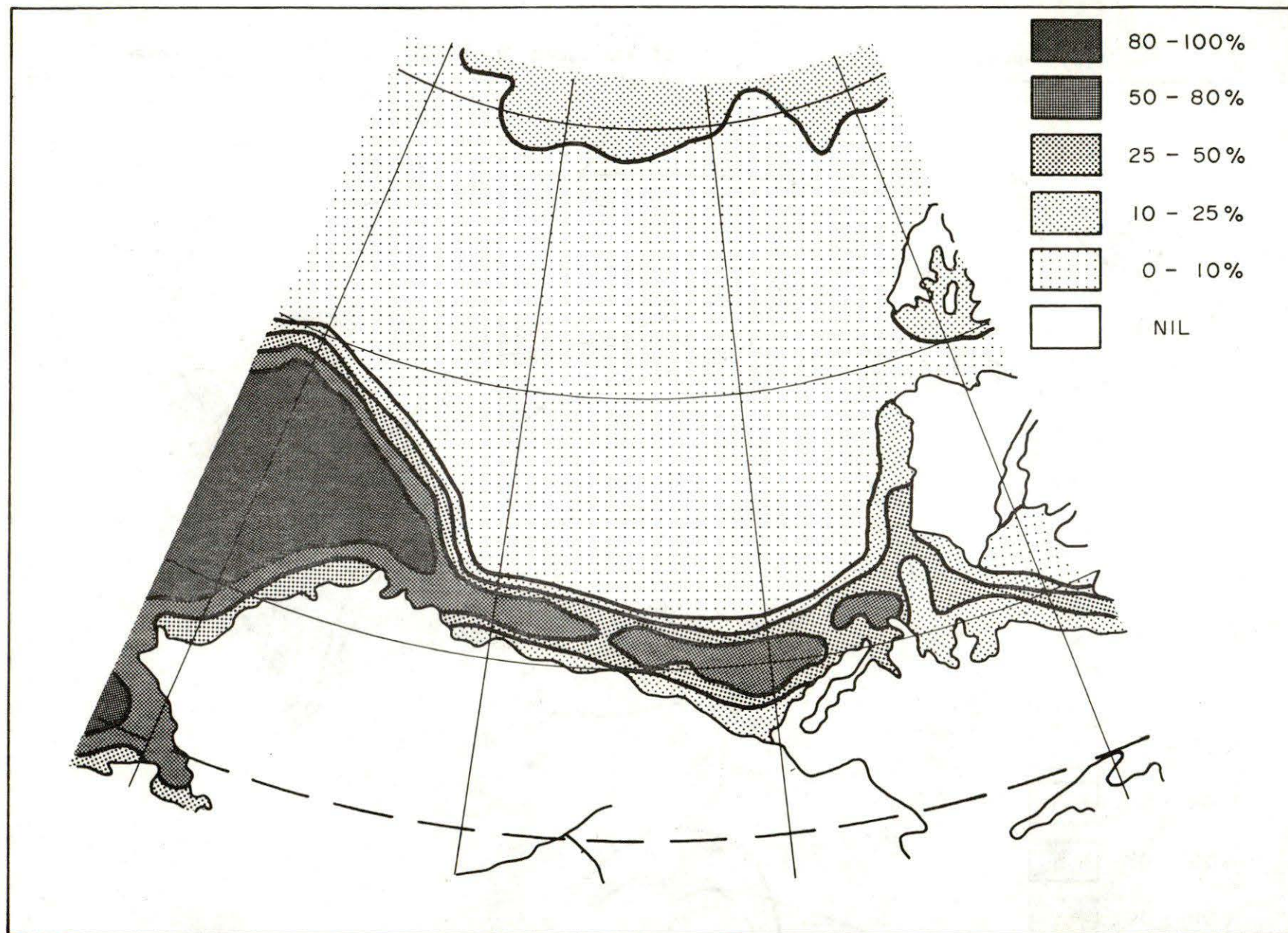


Figure 27. Percentage of open water, remainder is multi-year ice, 7 - 9 September 1974.

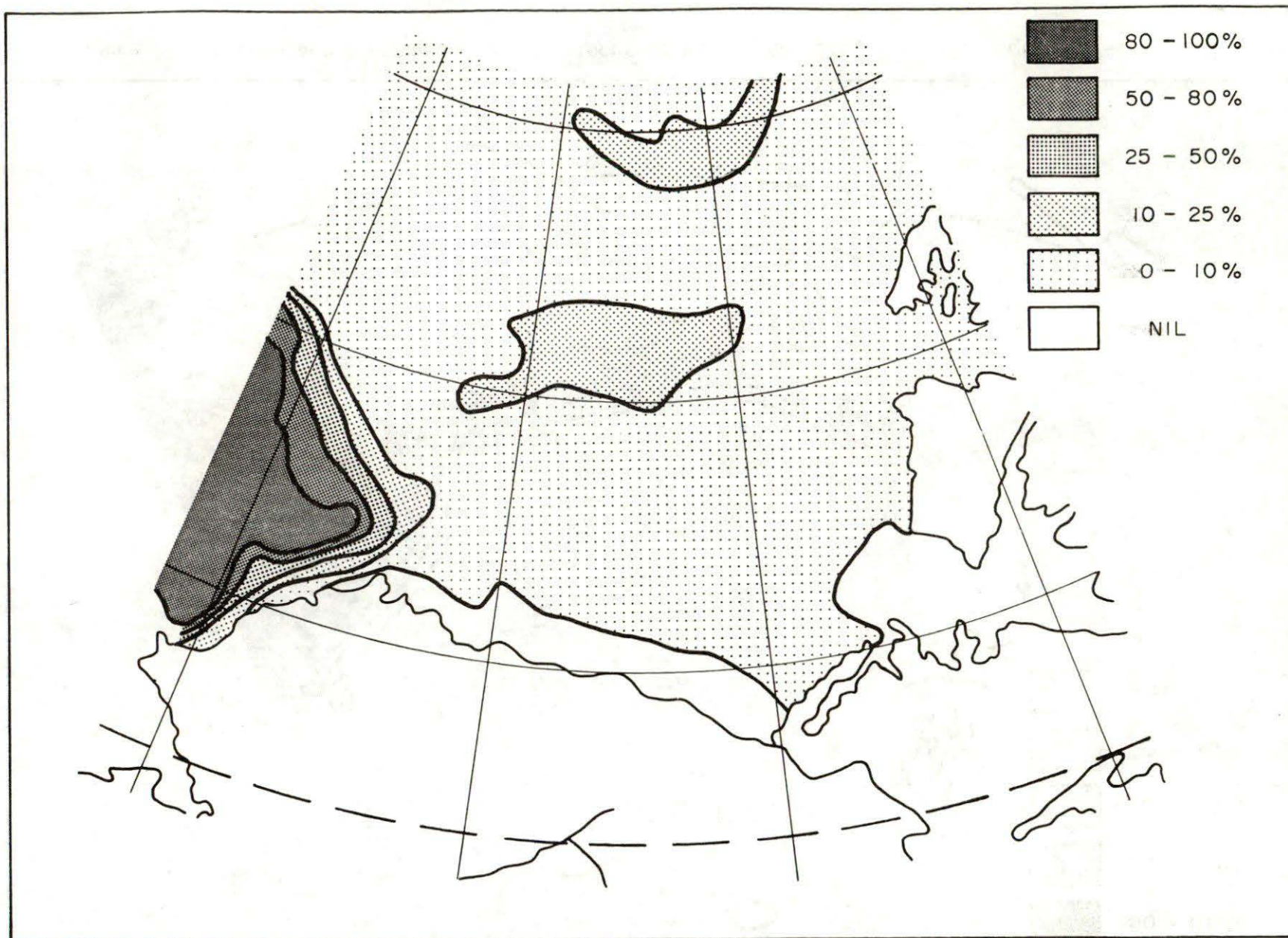


Figure 28. Percentage of open water, remainder is multi-year ice, 7 - 9 October, 1974.

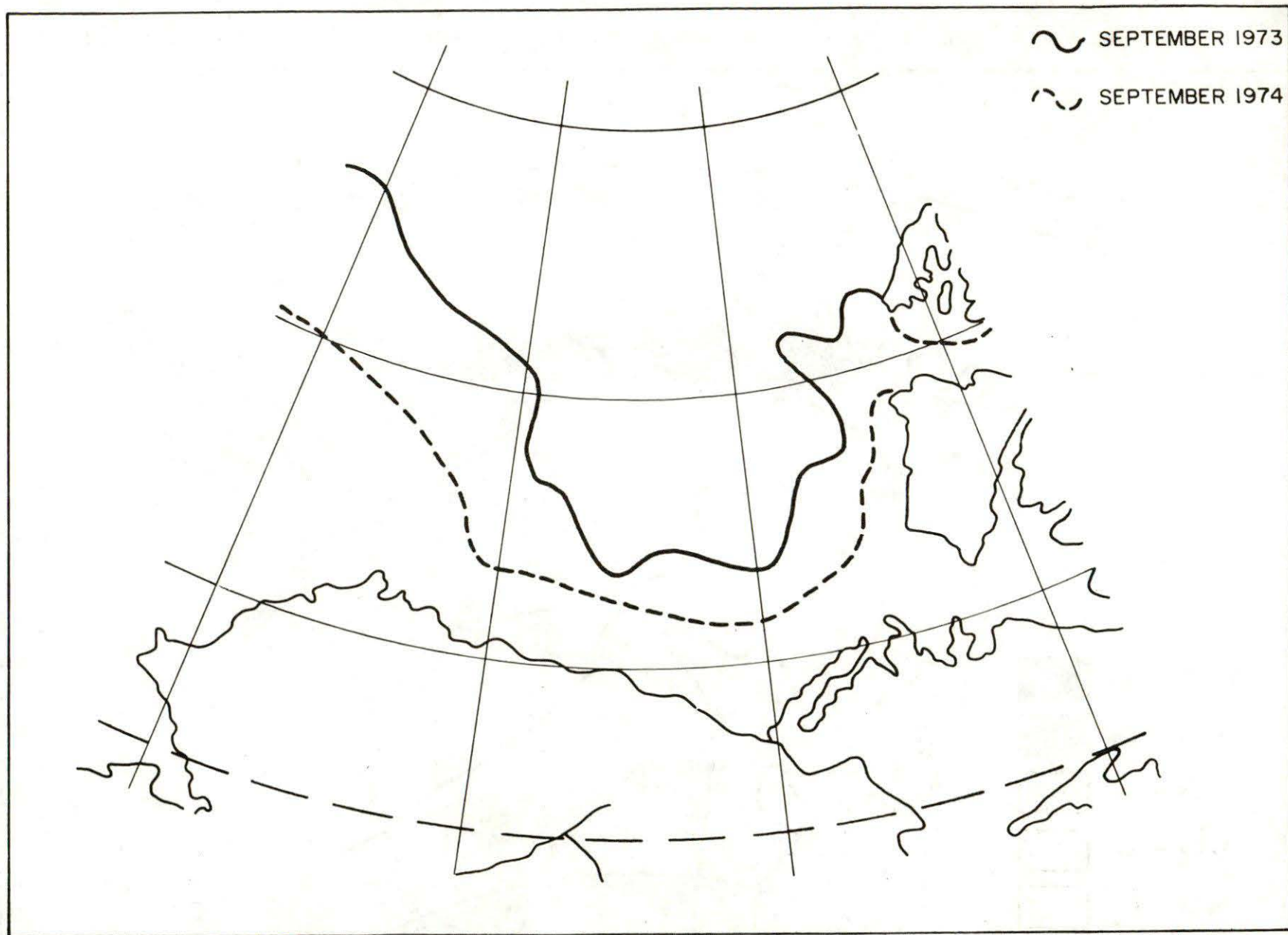


Figure 29. Minimum extent of pack ice in September, 1973 and 1974.

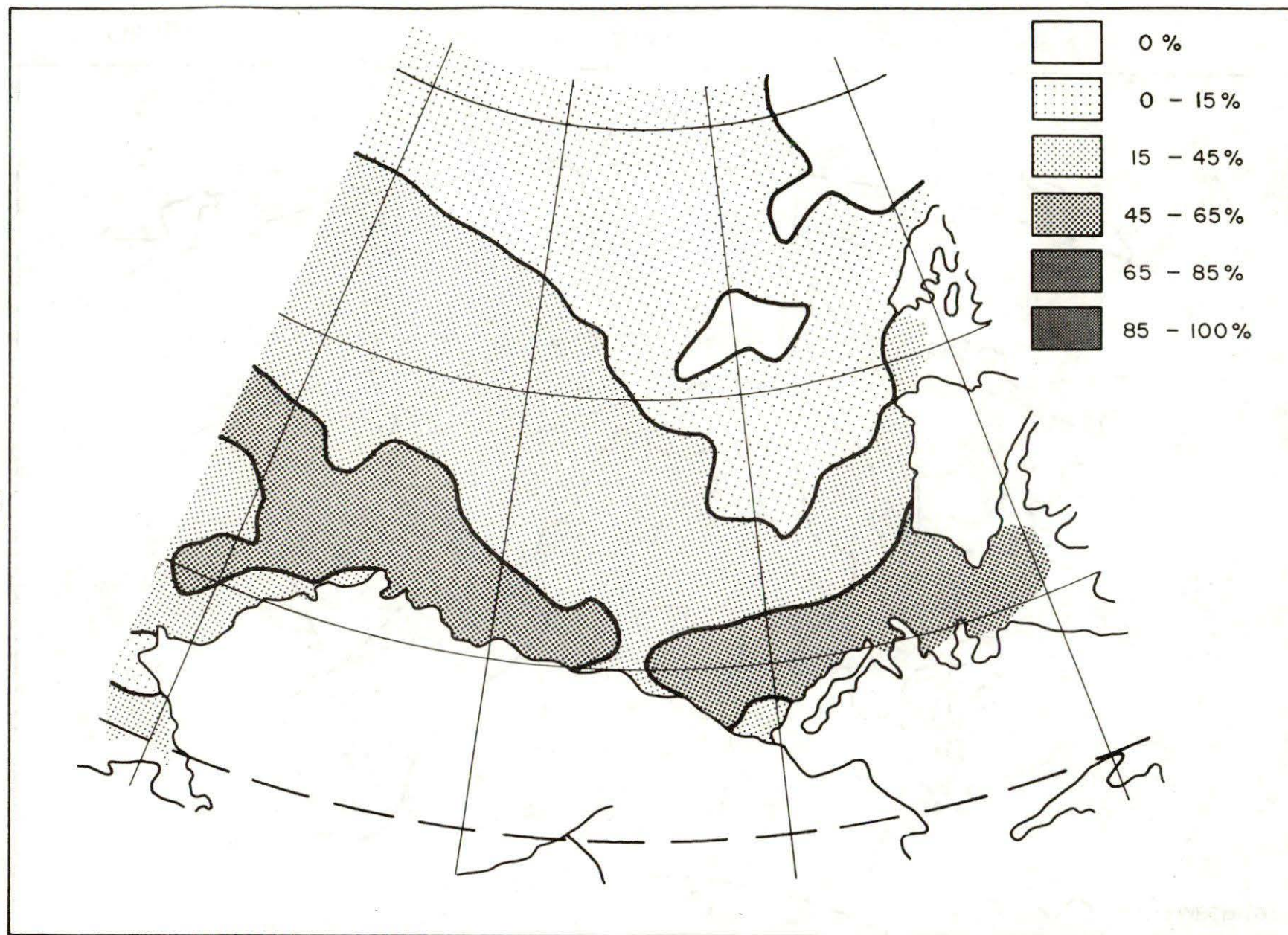


Figure 30. Percentage of first-year ice, remainder is multi-year ice, 20 - 22 December 1972.

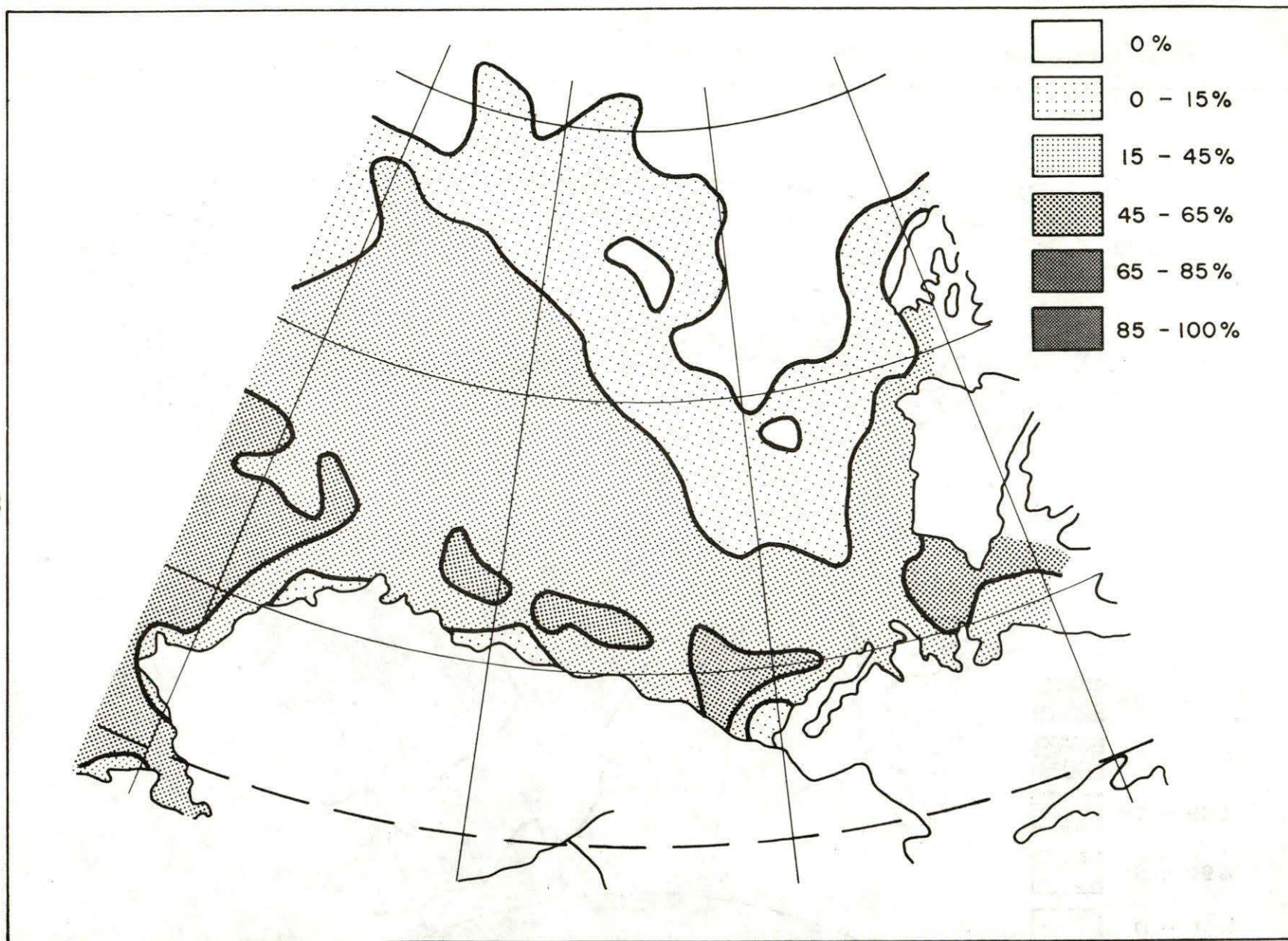


Figure 31. Percentage of first-year ice, remainder is multi-year ice, 15 - 17 January 1973.

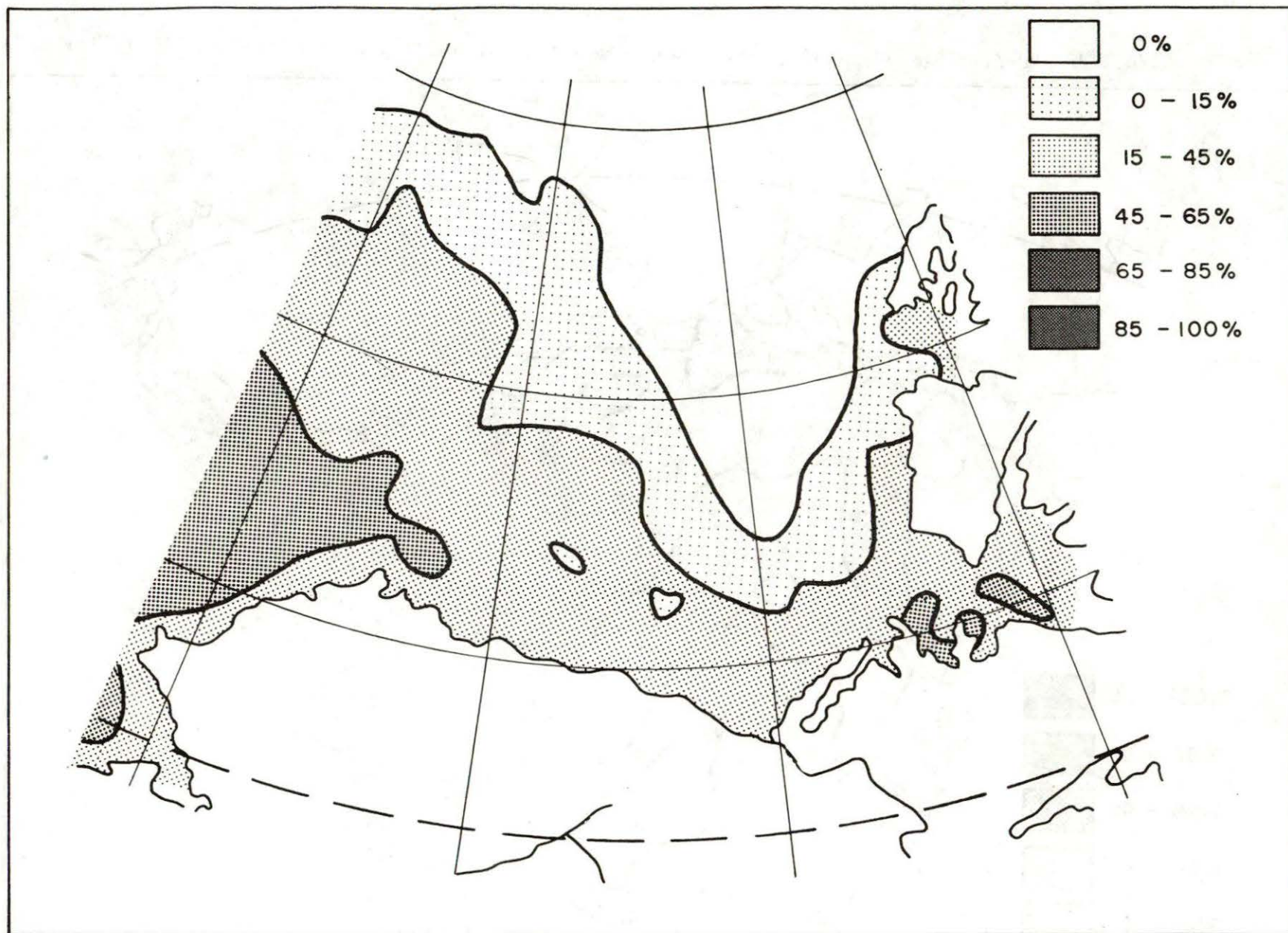


Figure 32. Percentage of first-year ice, remainder if multi-year ice, 14 - 16 February 1973.

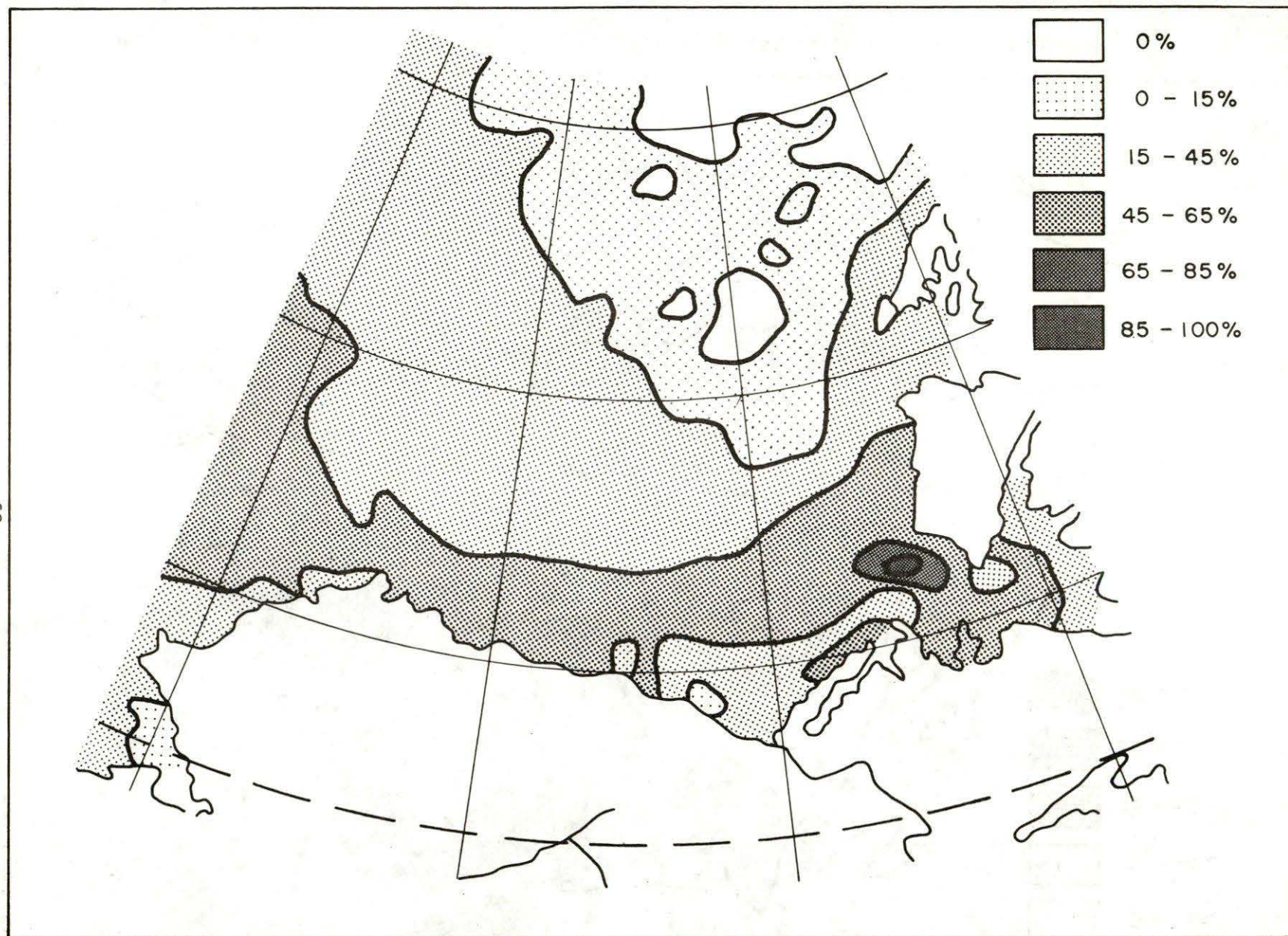


Figure 33. Percentage of first-year ice, remainder is multi-year ice, 10 - 12 December, 1973.

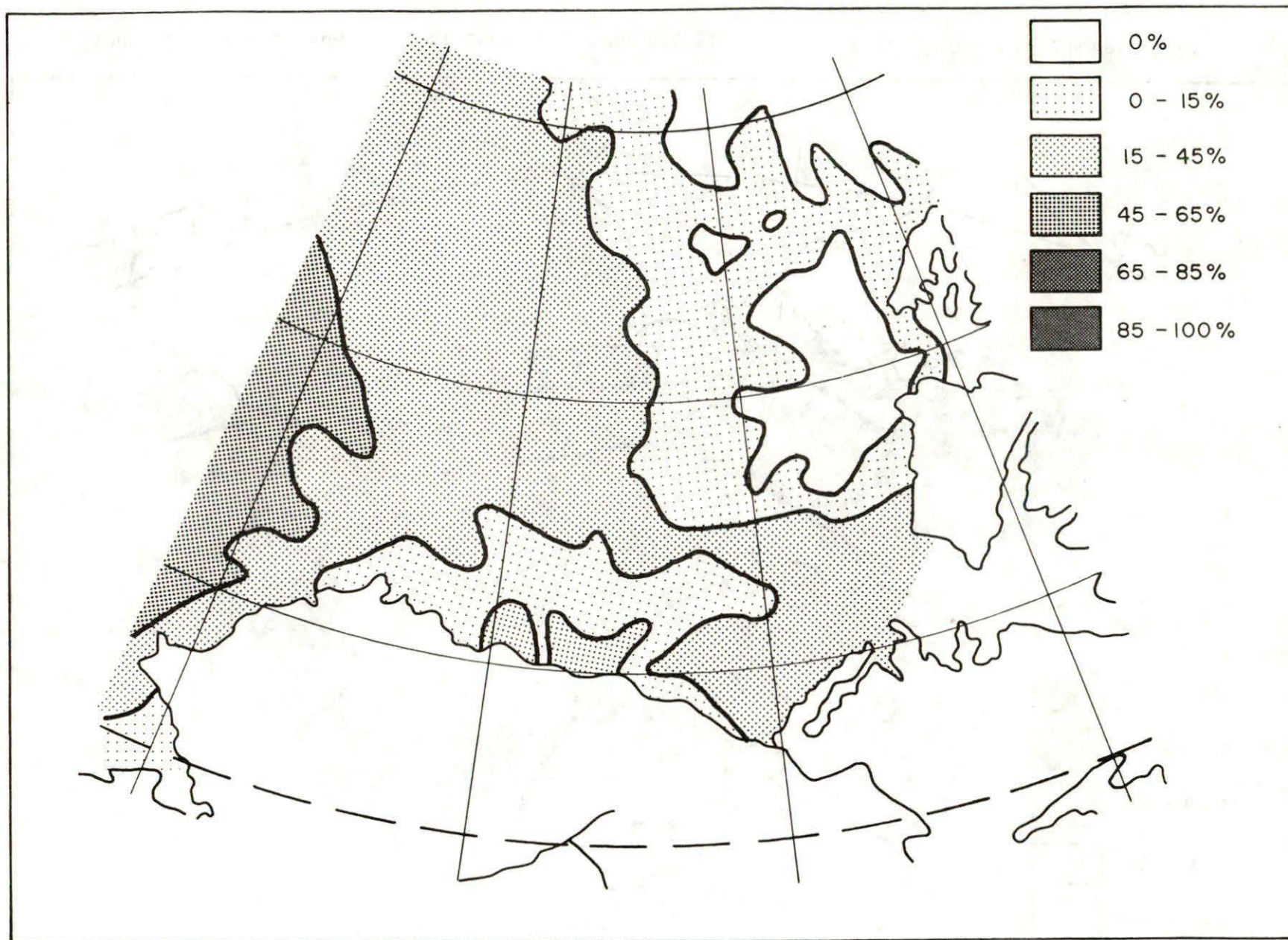


Figure 34. Percentage of first-year ice, remainder is multi-year ice, 10 - 12 January 1974.

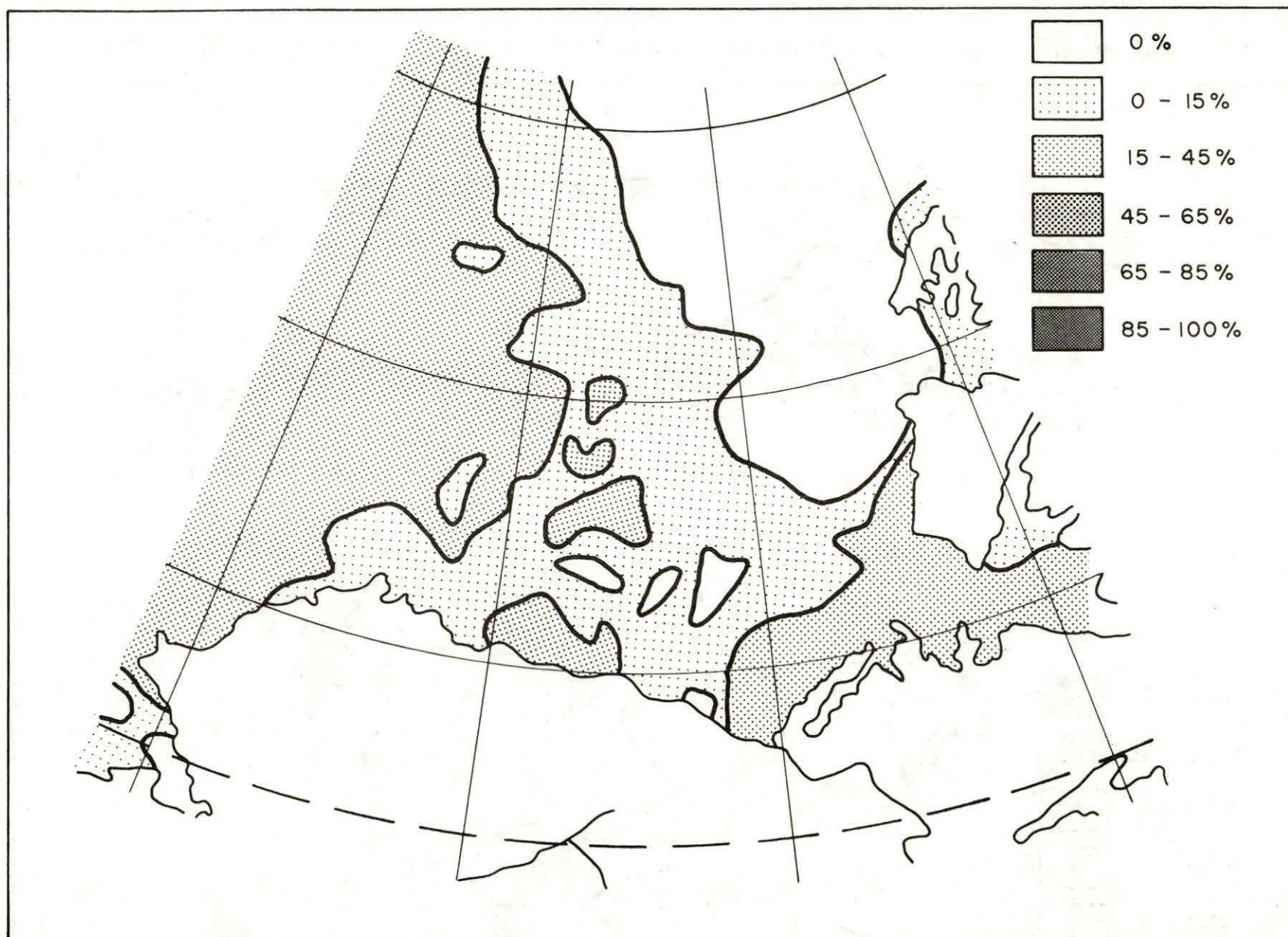


Figure 35. Percentage of first-year ice, remainder is multi-year ice, 6 - 8 February 1974.

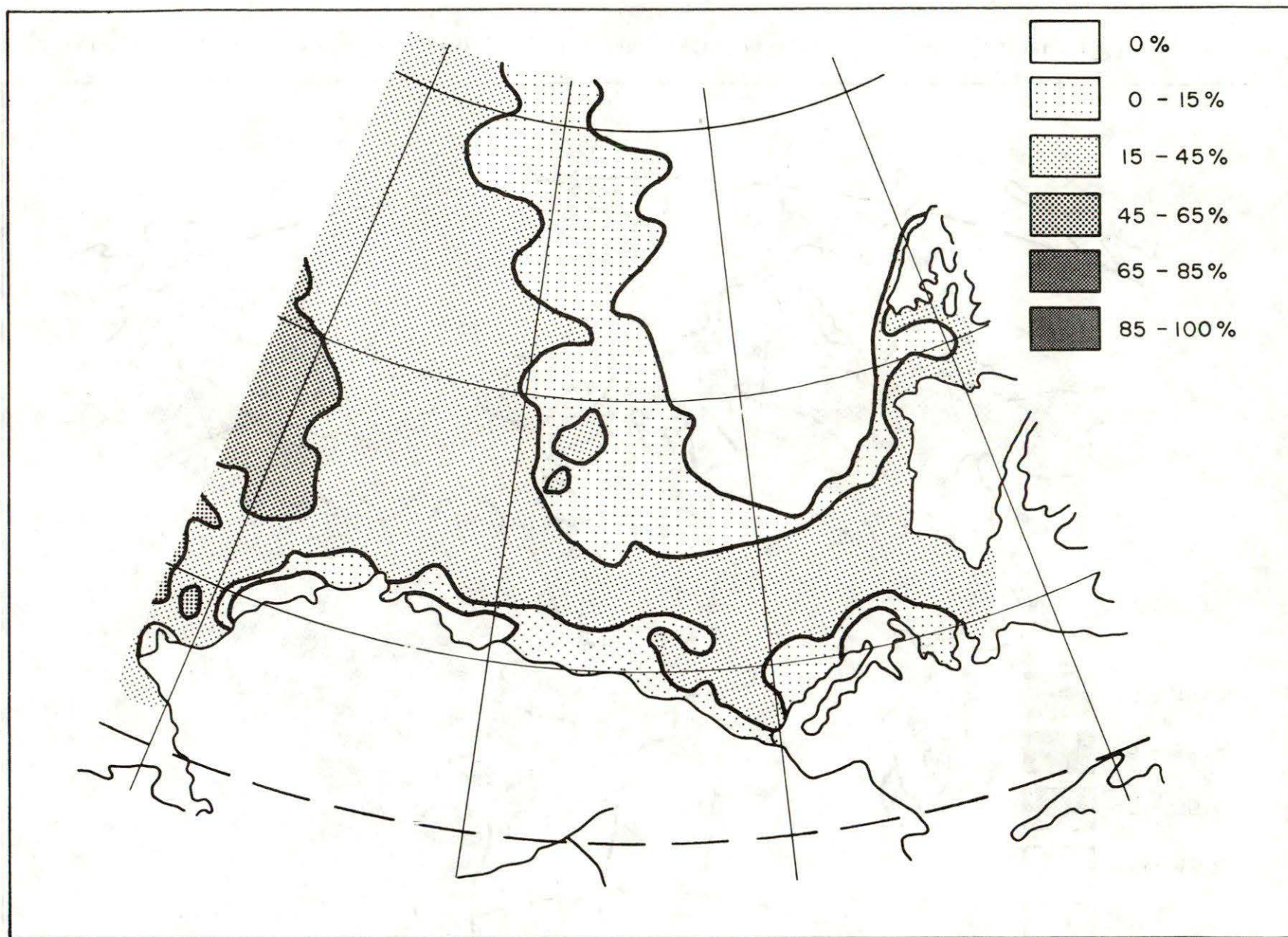


Figure 36. Percentage of first-year ice, remainder is multi-year ice, 11 - 13 March 1974.

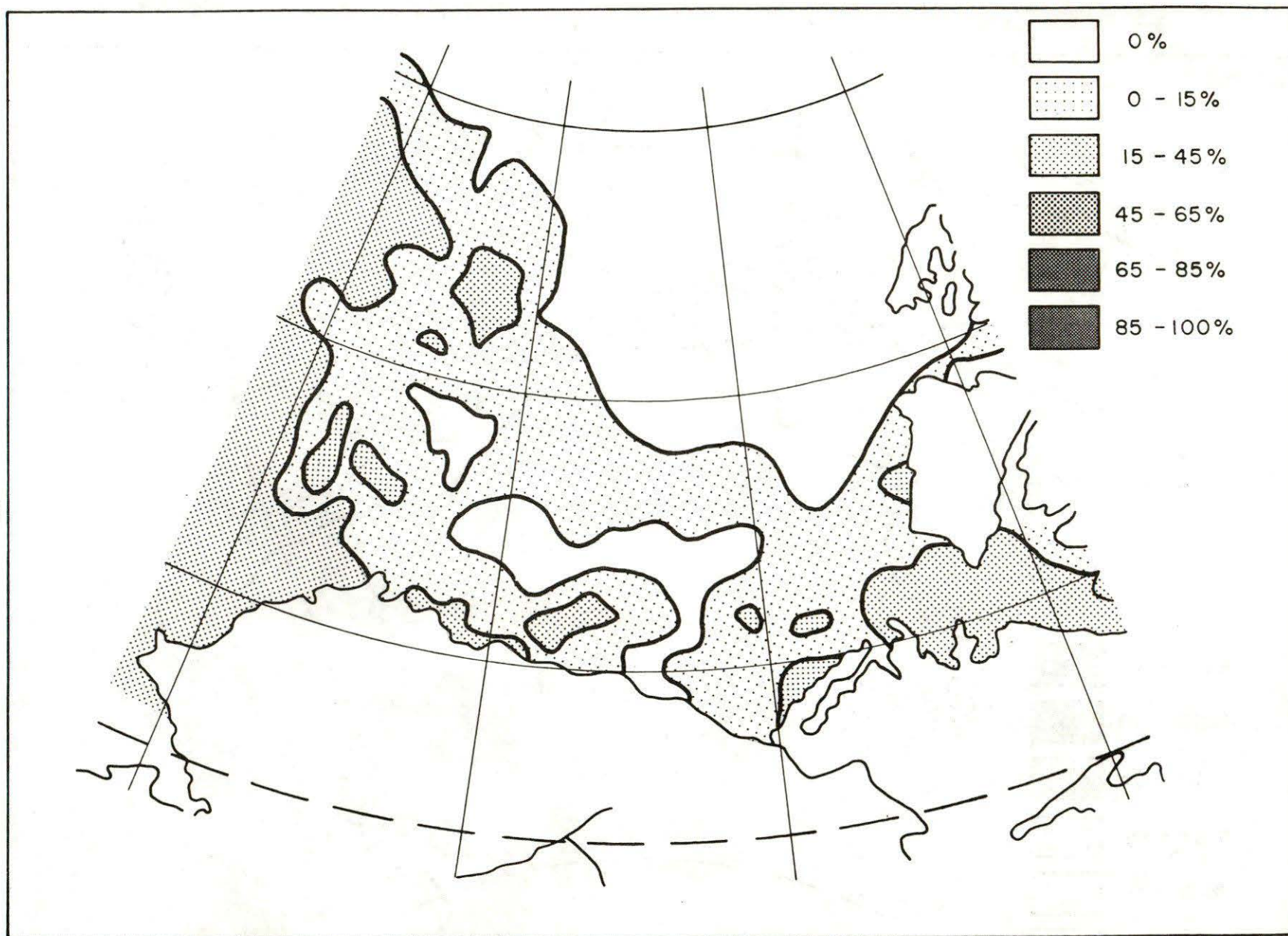


Figure 37. Percentage of first-year ice, remainder is multi-year ice, 6 - 8 December 1974.

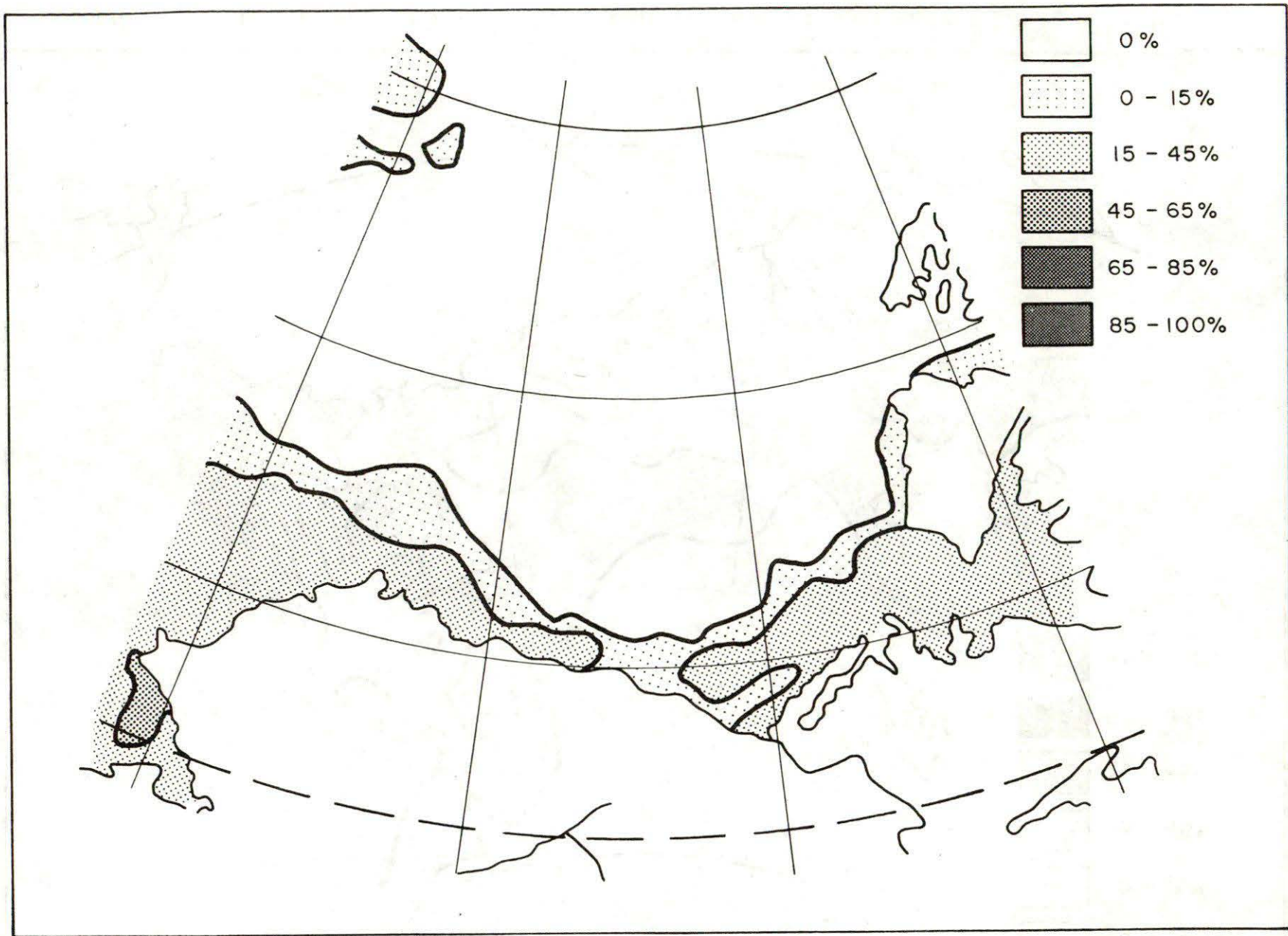


Figure 38. Percentage of first-year ice, remainder is multi-year ice, 5 - 7 January 1975.

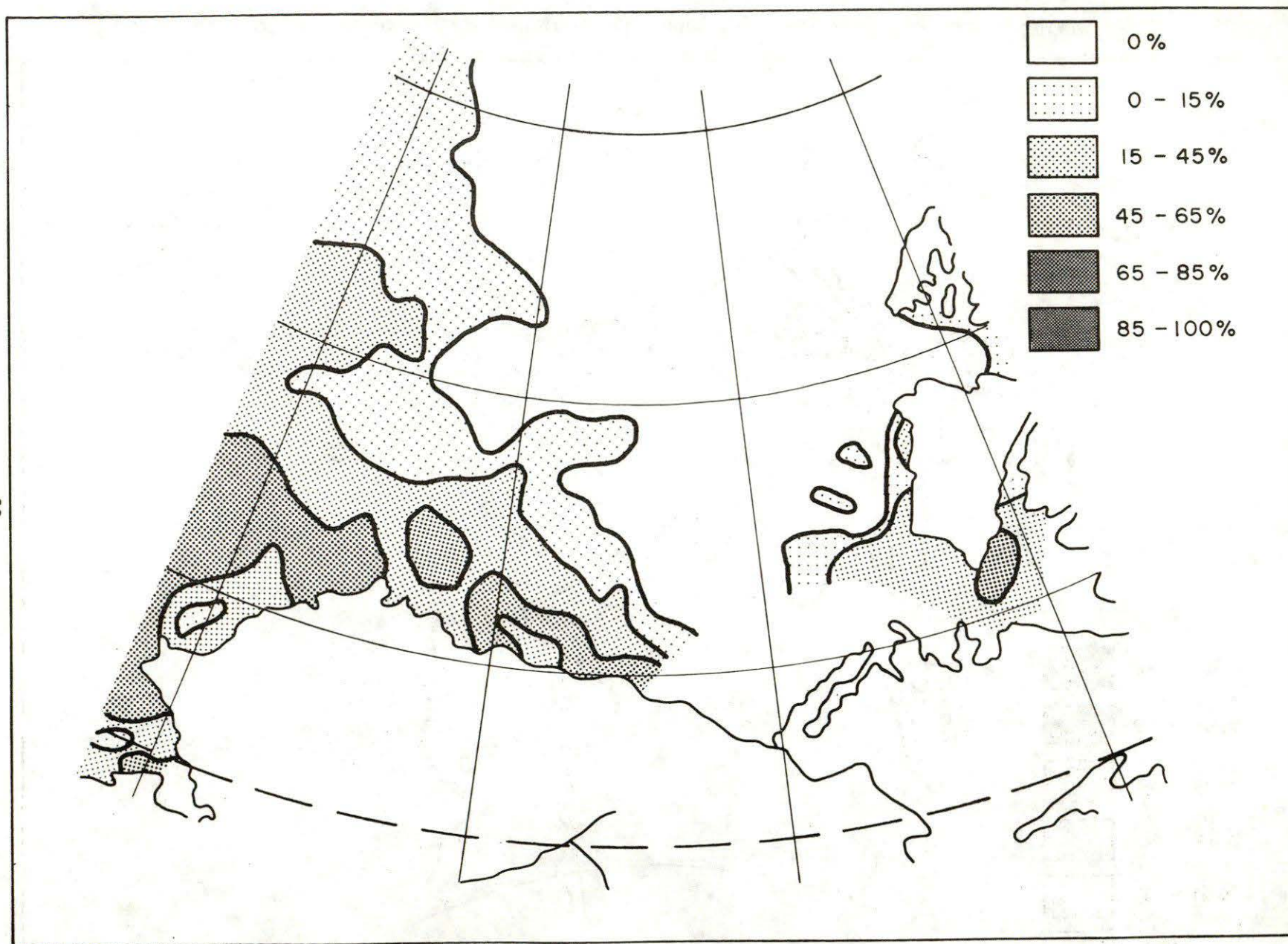


Figure 39. Percentage of first-year ice, remainder is multi-year ice, 4 - 6 February 1975.

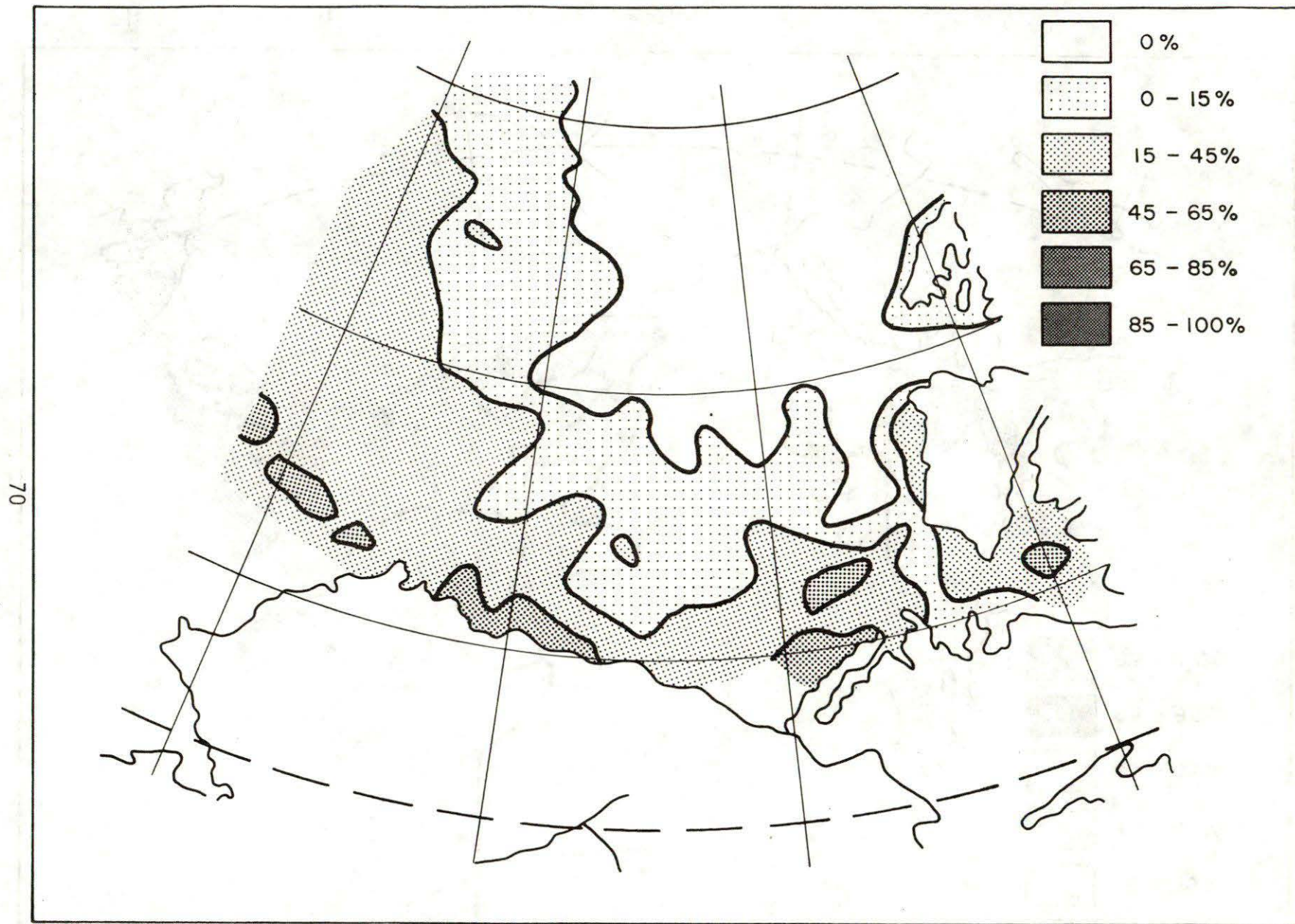


Figure 40. Percentage of first-year ice, remainder is multi-year ice, 6 - 8 March 1975.

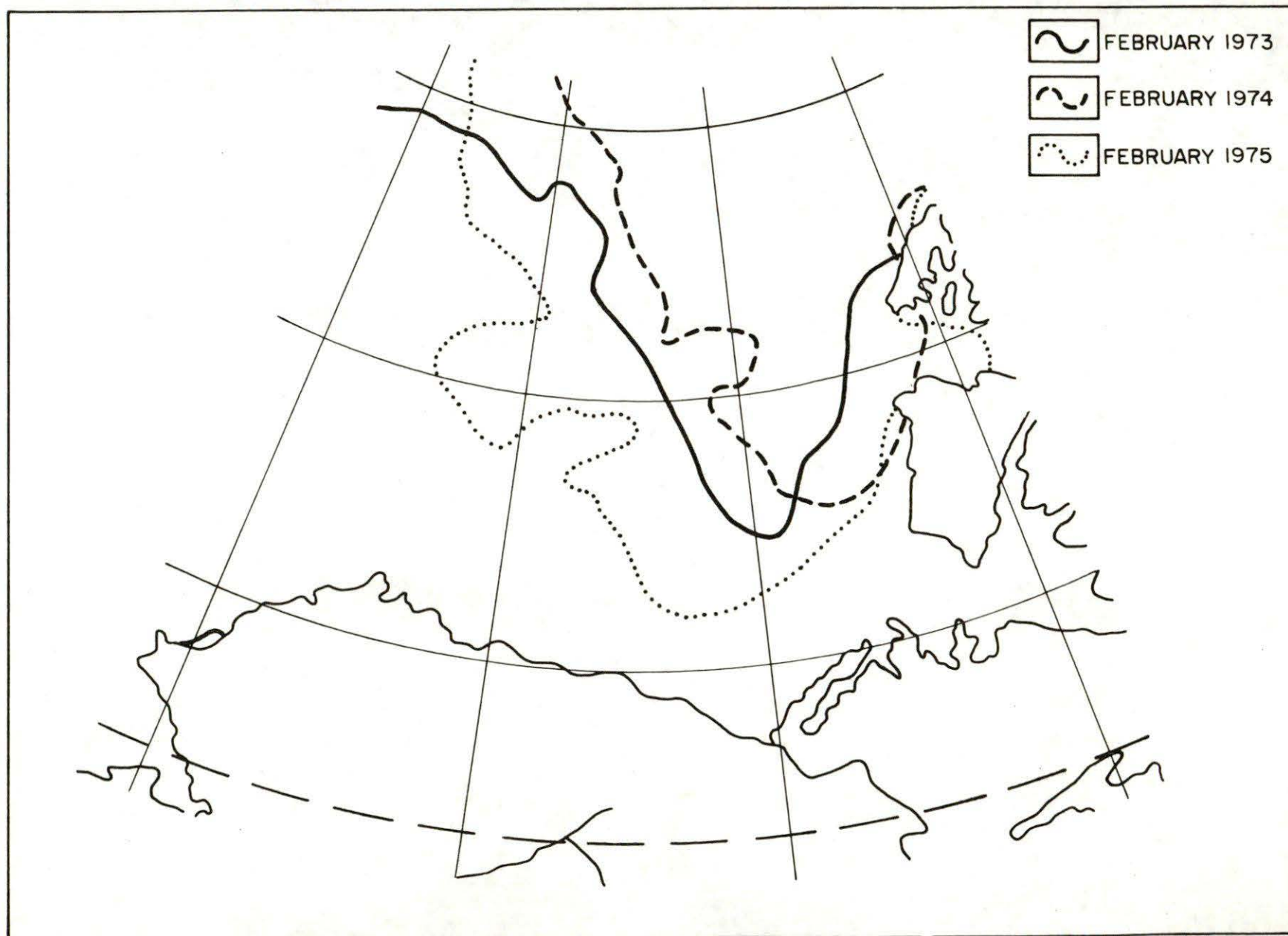


Figure 41. Maximum extent of multi-year ice in February 1973 - 1975.

156-96/00337

FINAL

ADDRESS



APPENDIX A

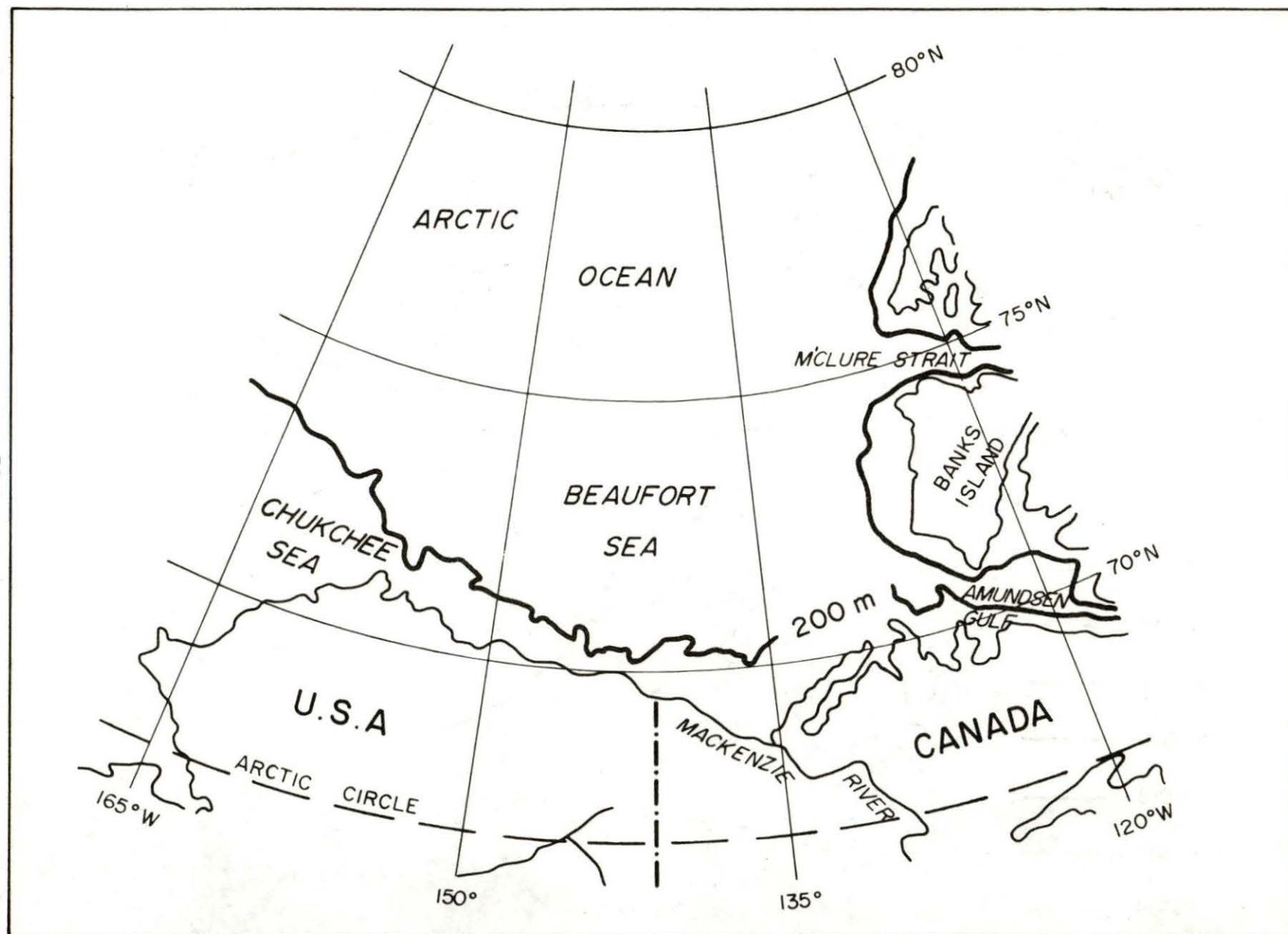


Figure A1. Study area for ESMR data.

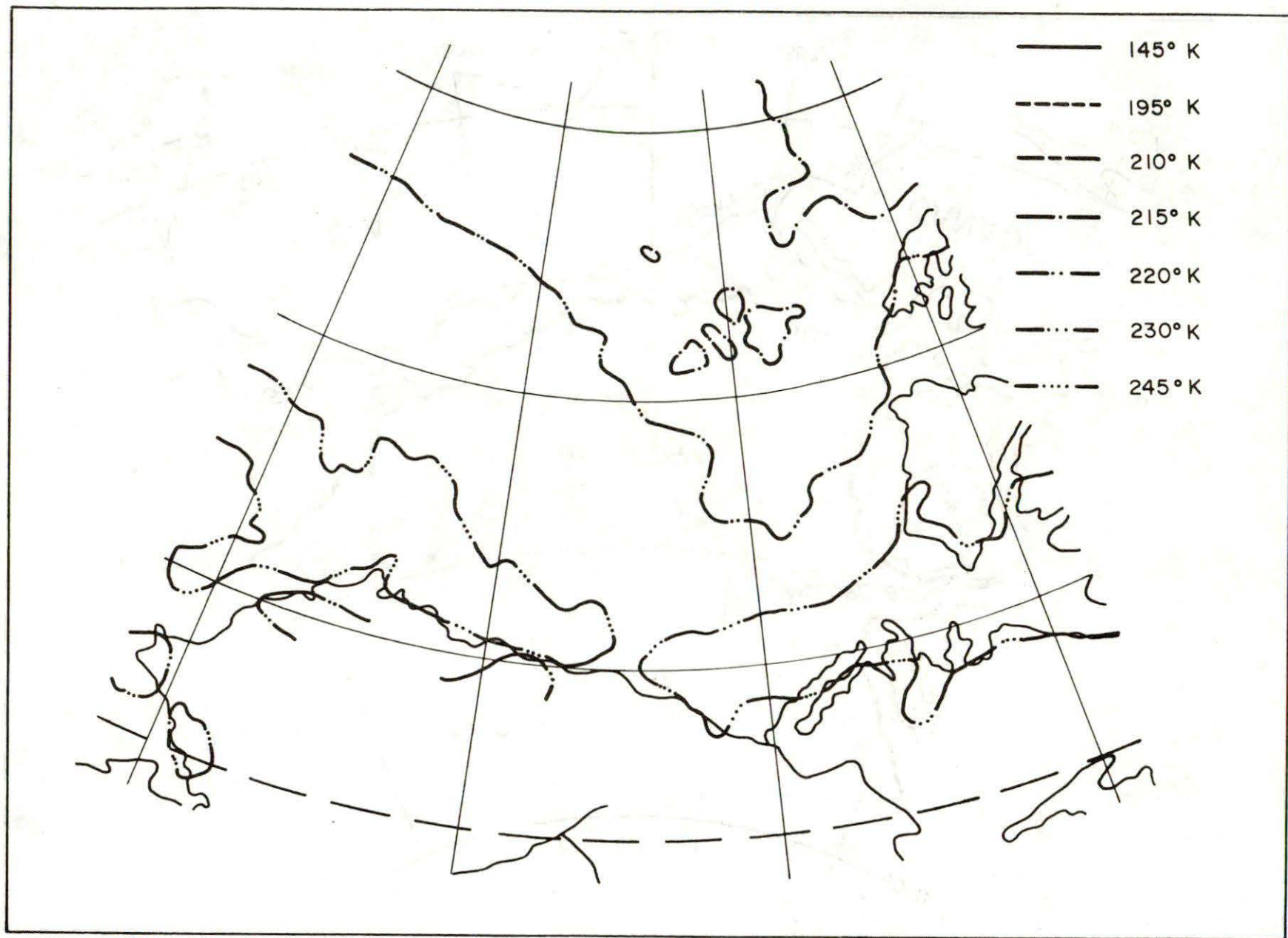


Figure A2. Monthly map of brightness temperature contours, December 1972.

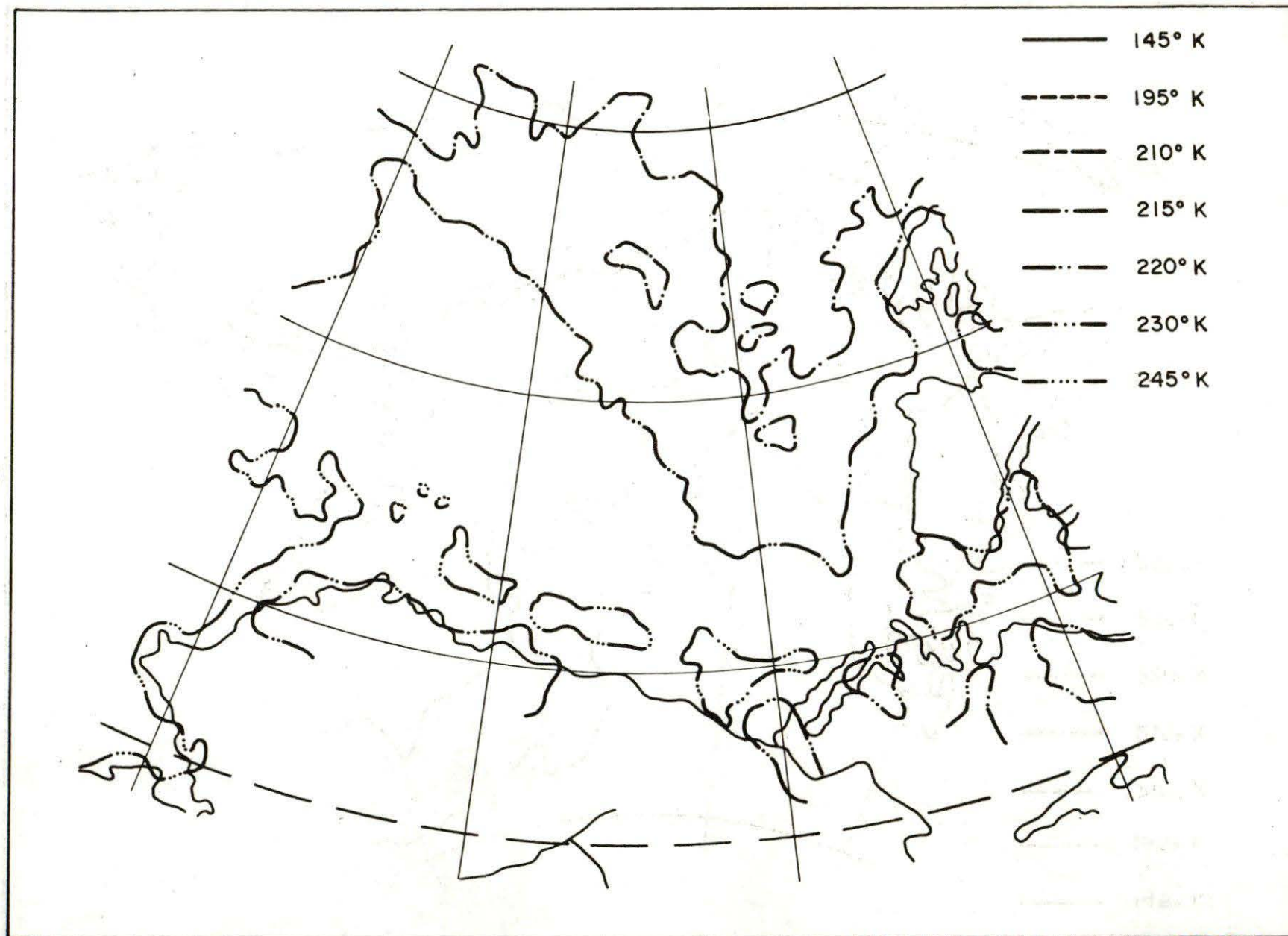


Figure A3. Monthly map of brightness temperature contours, January 1973.

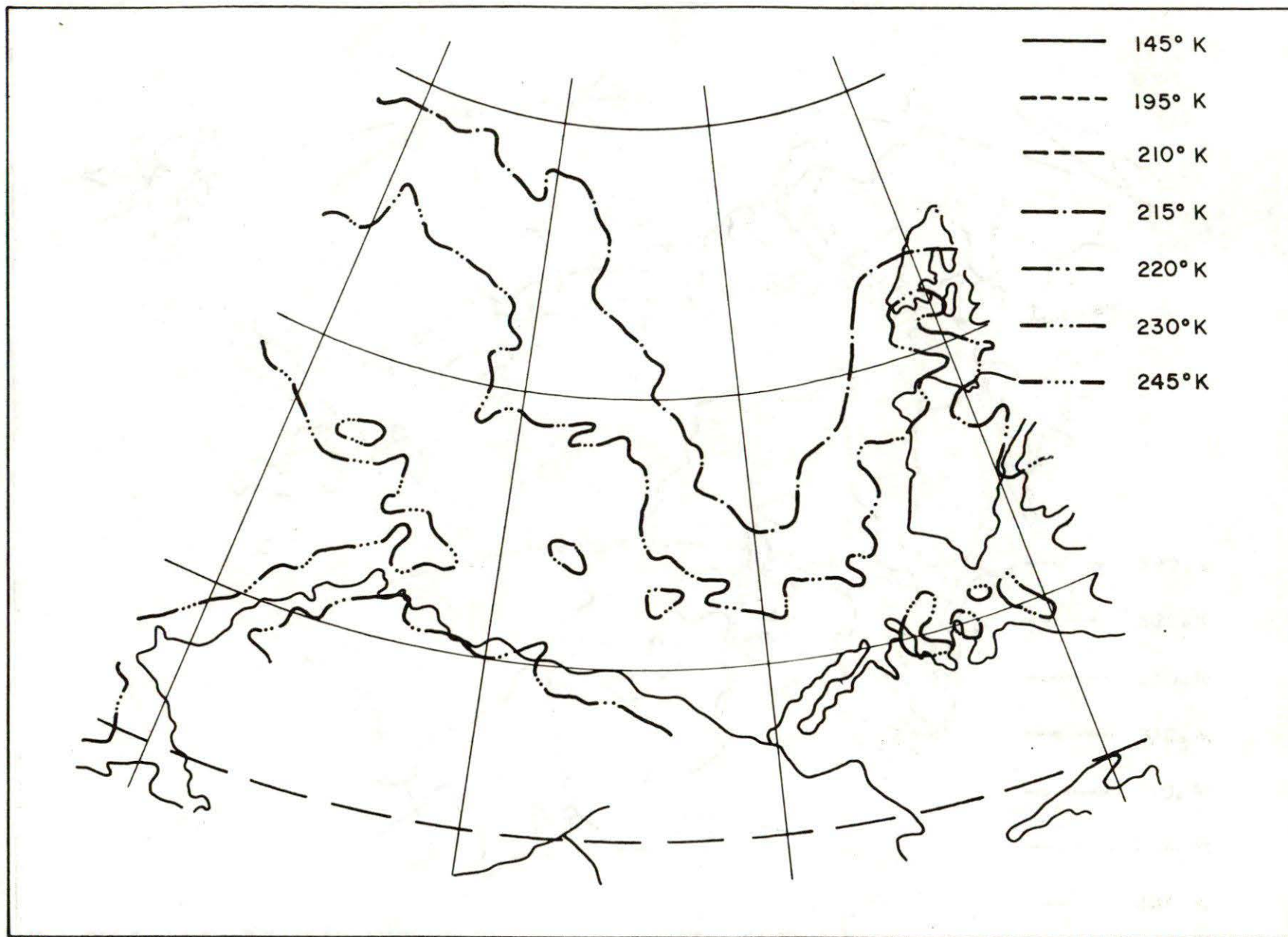


Figure A4. Monthly map of brightness temperature contours, February 1973.

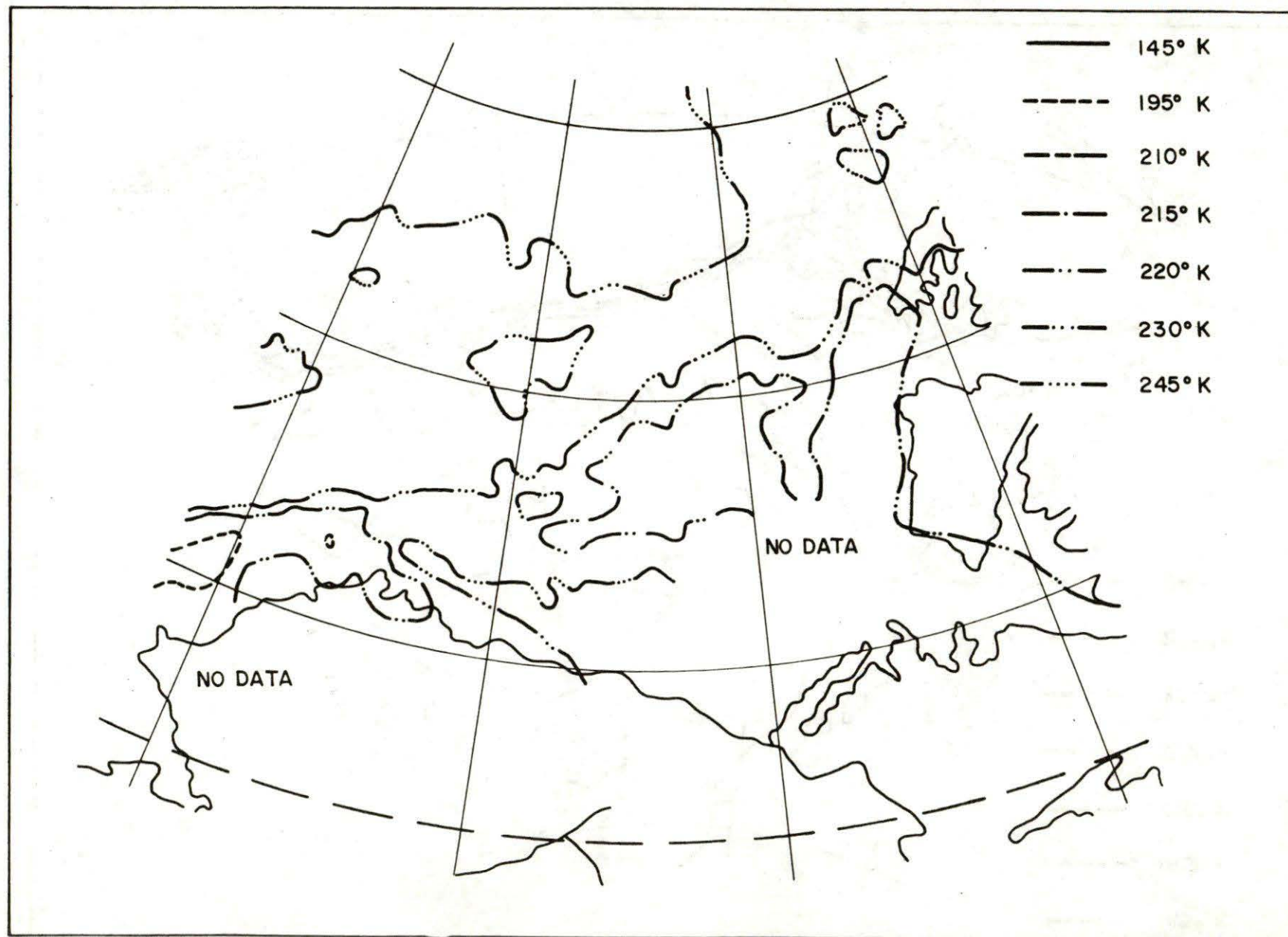


Figure A5. Monthly map of brightness temperature contours, June 1973.

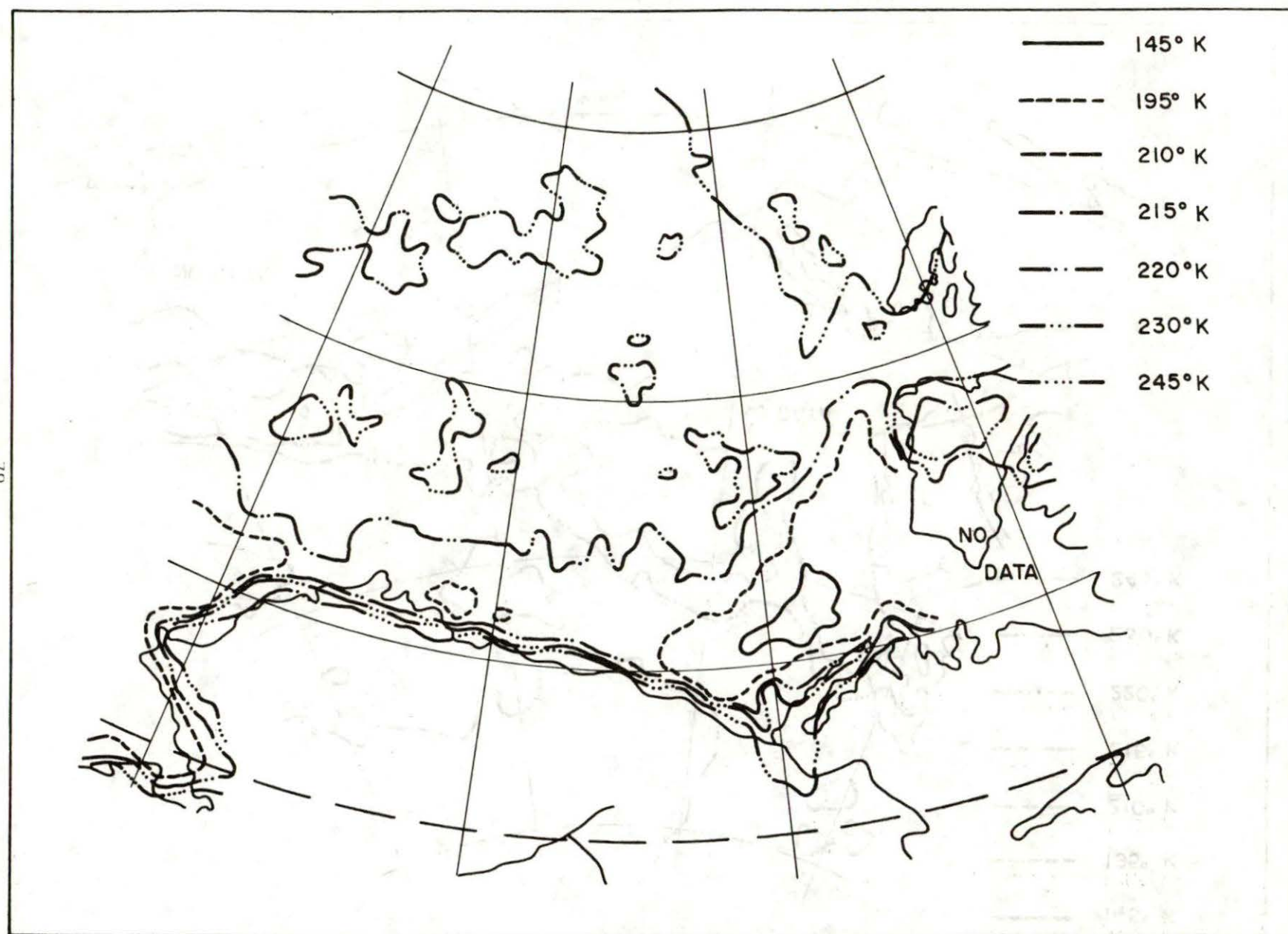


Figure A6. Monthly map of brightness temperature contours, July 1973.

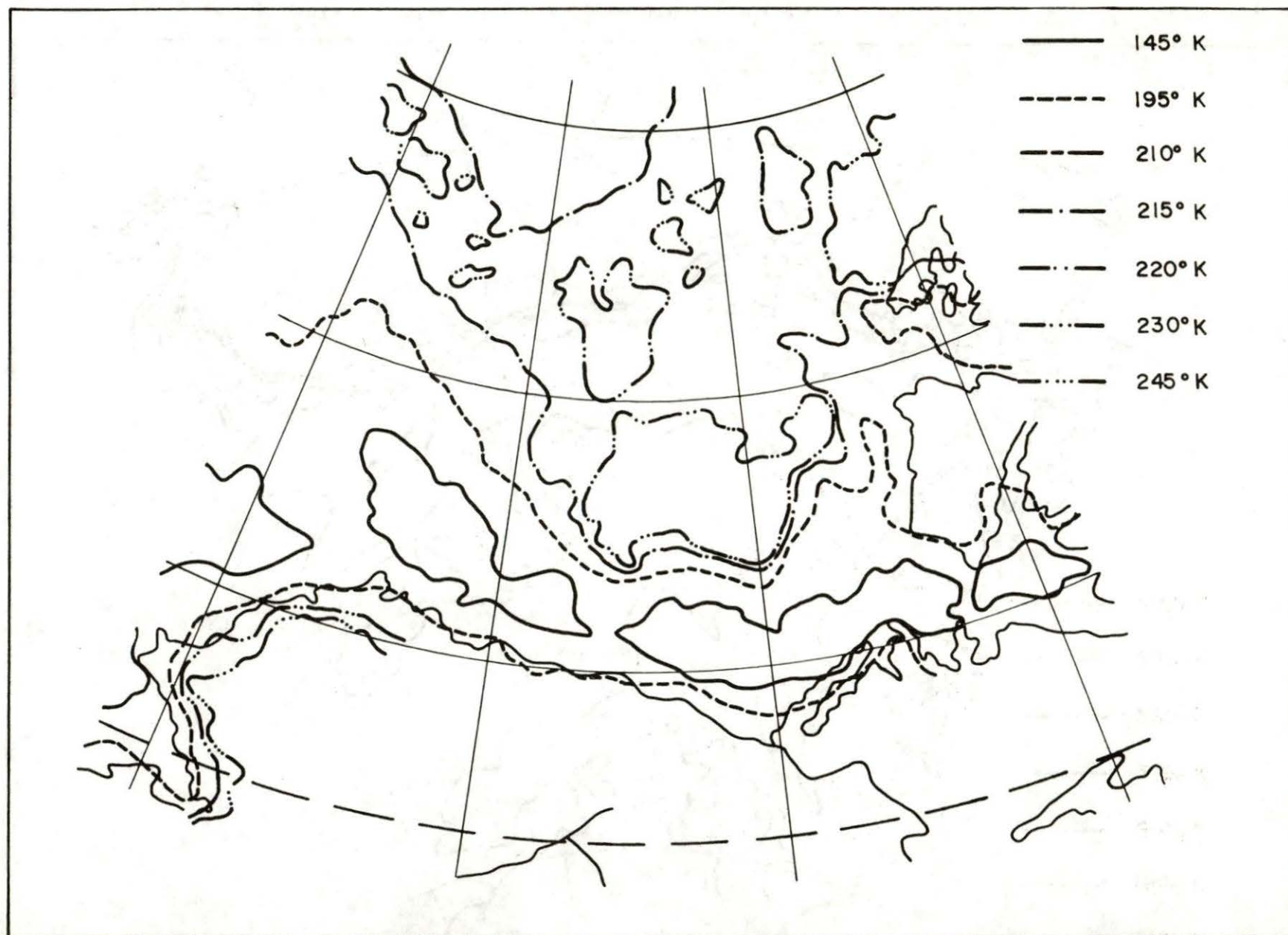


Figure A7. Monthly map of brightness temperature contours, September 1973.

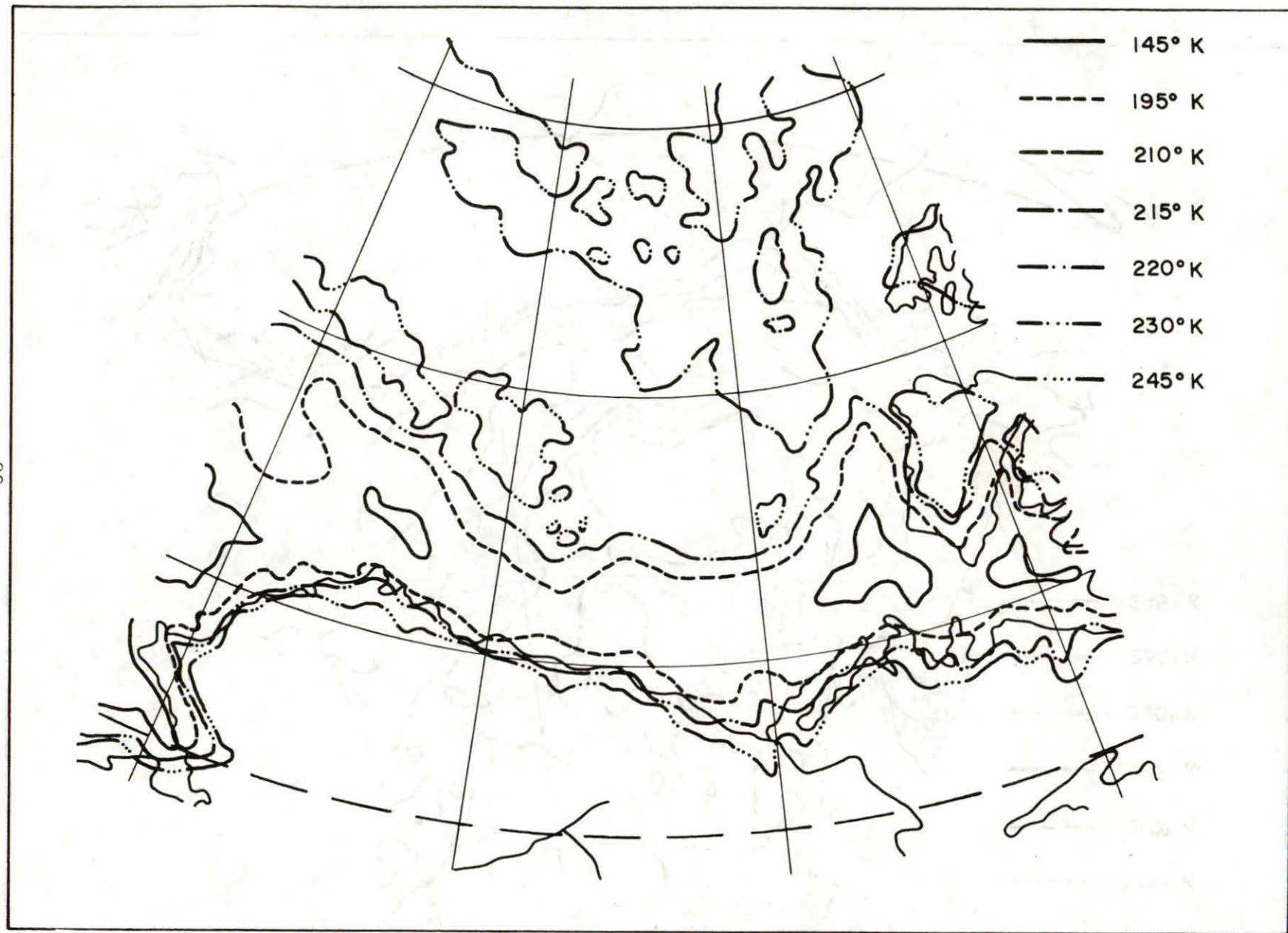


Figure A8. Monthly map of brightness temperature contours, October 1973.

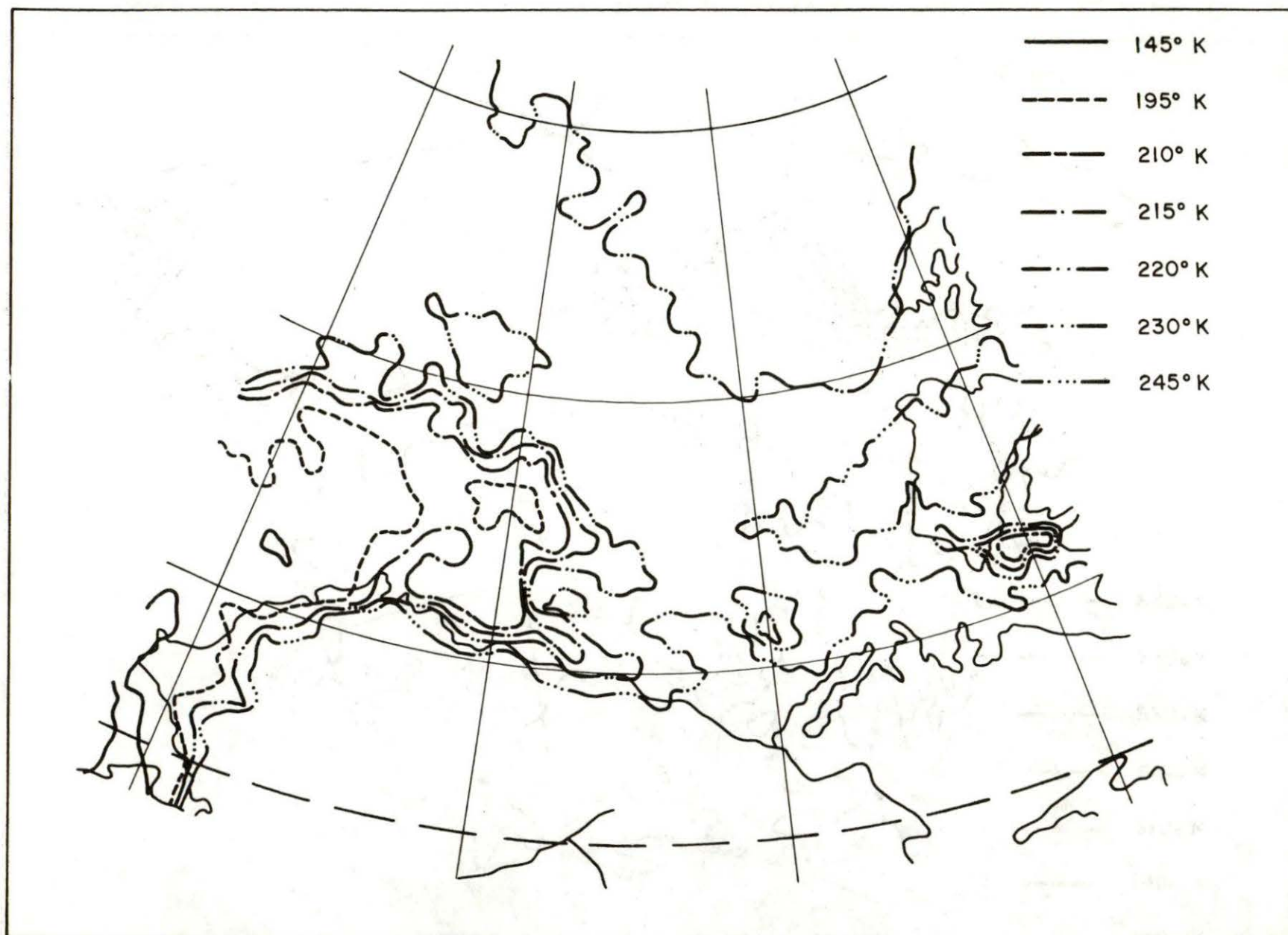


Figure A9. Monthly map of brightness temperature contours, November 1973.

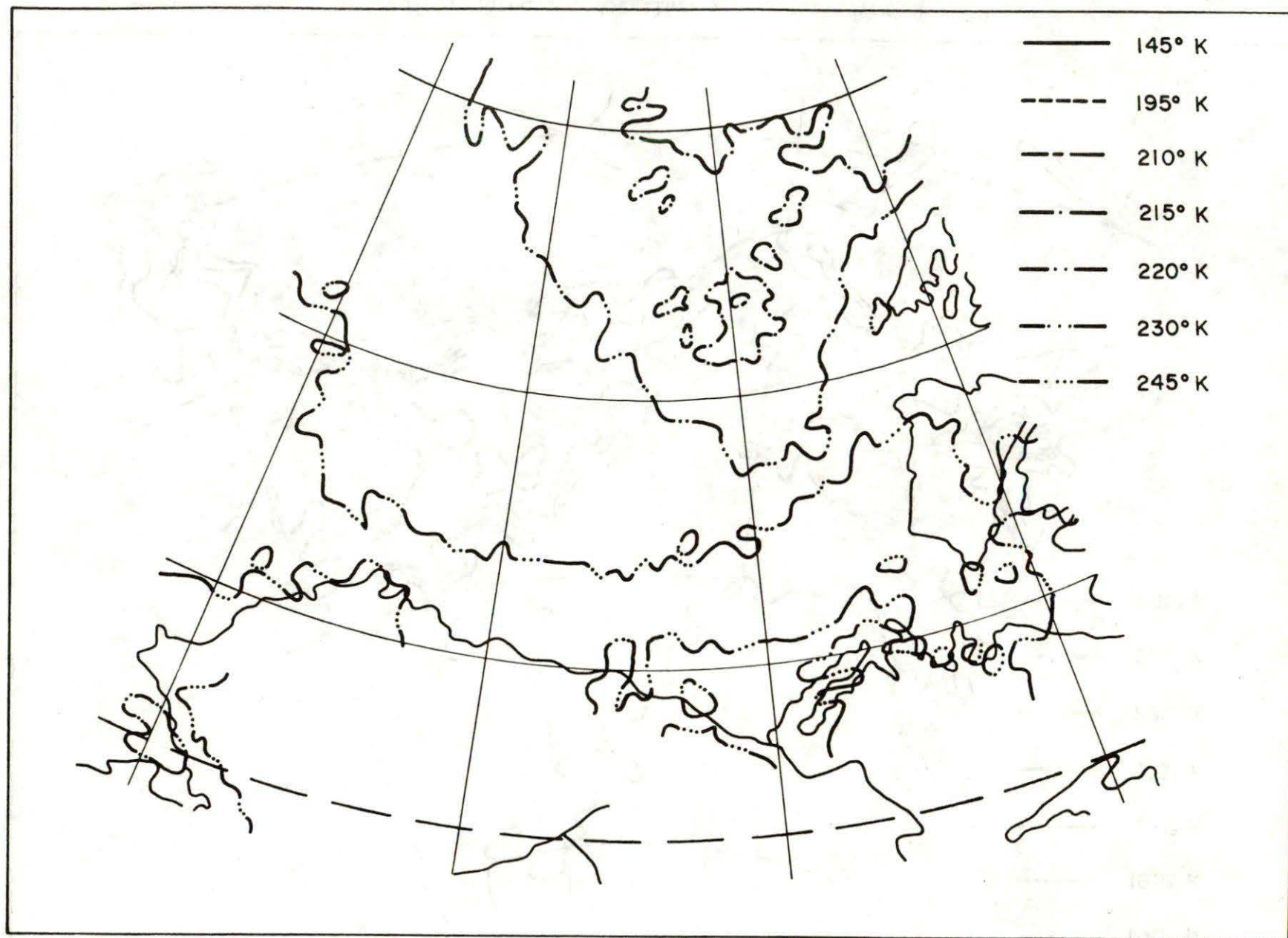


Figure A10. Monthly map of brightness temperature contours, December 1973.

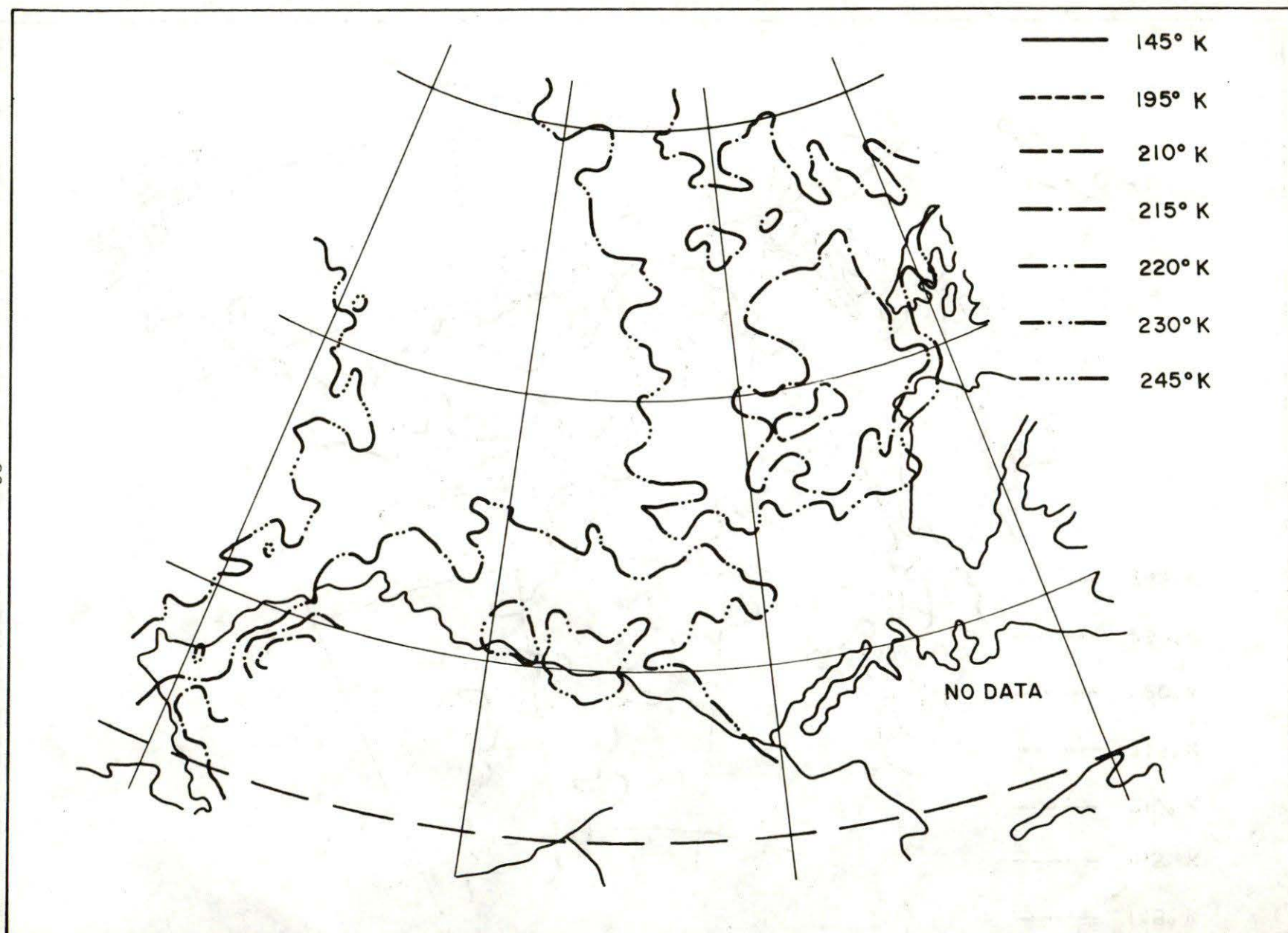


Figure A11. Monthly map of brightness temperature contours, January 1974.

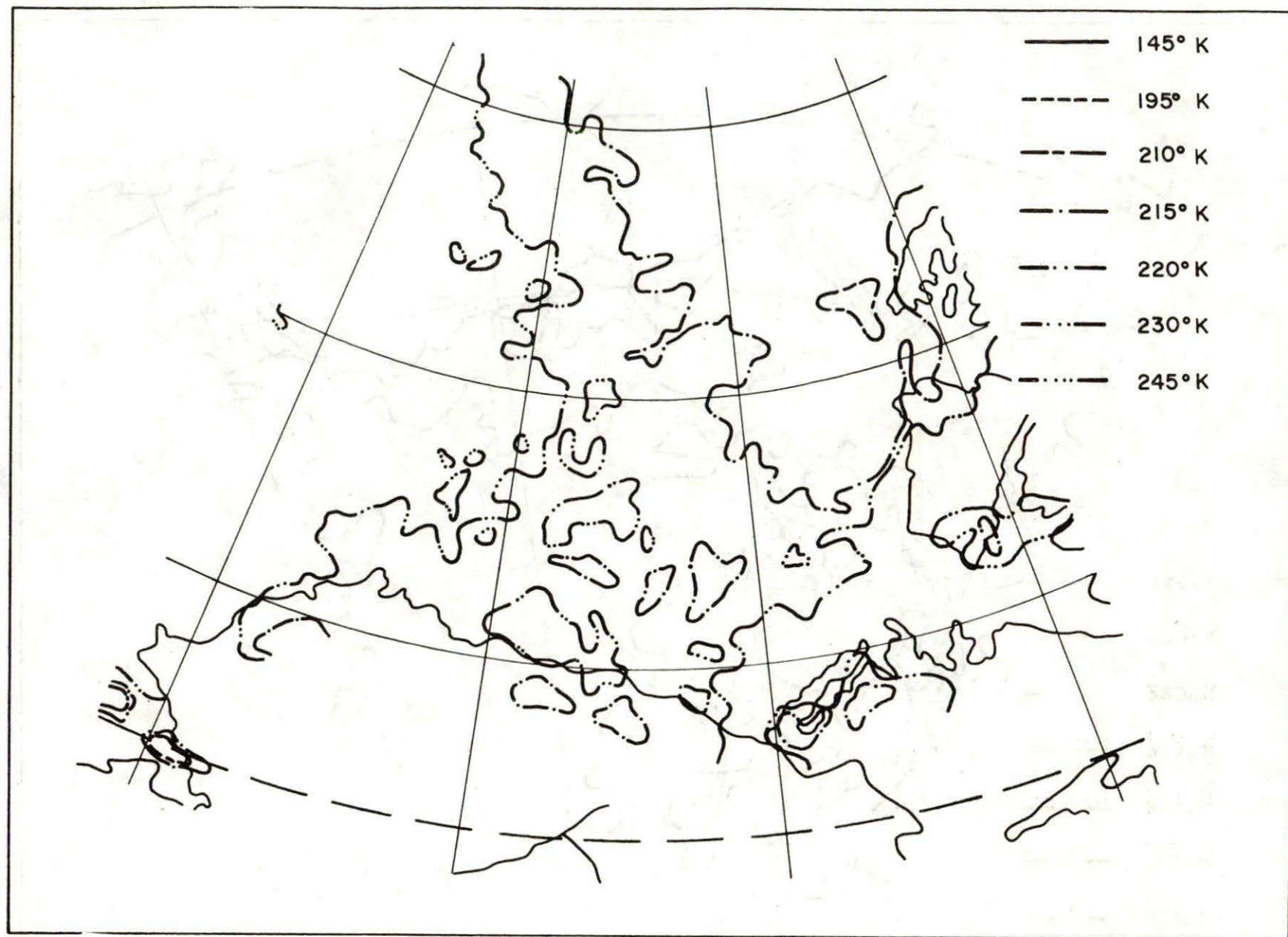


Figure A12. Monthly map of brightness temperature contours, February 1974.

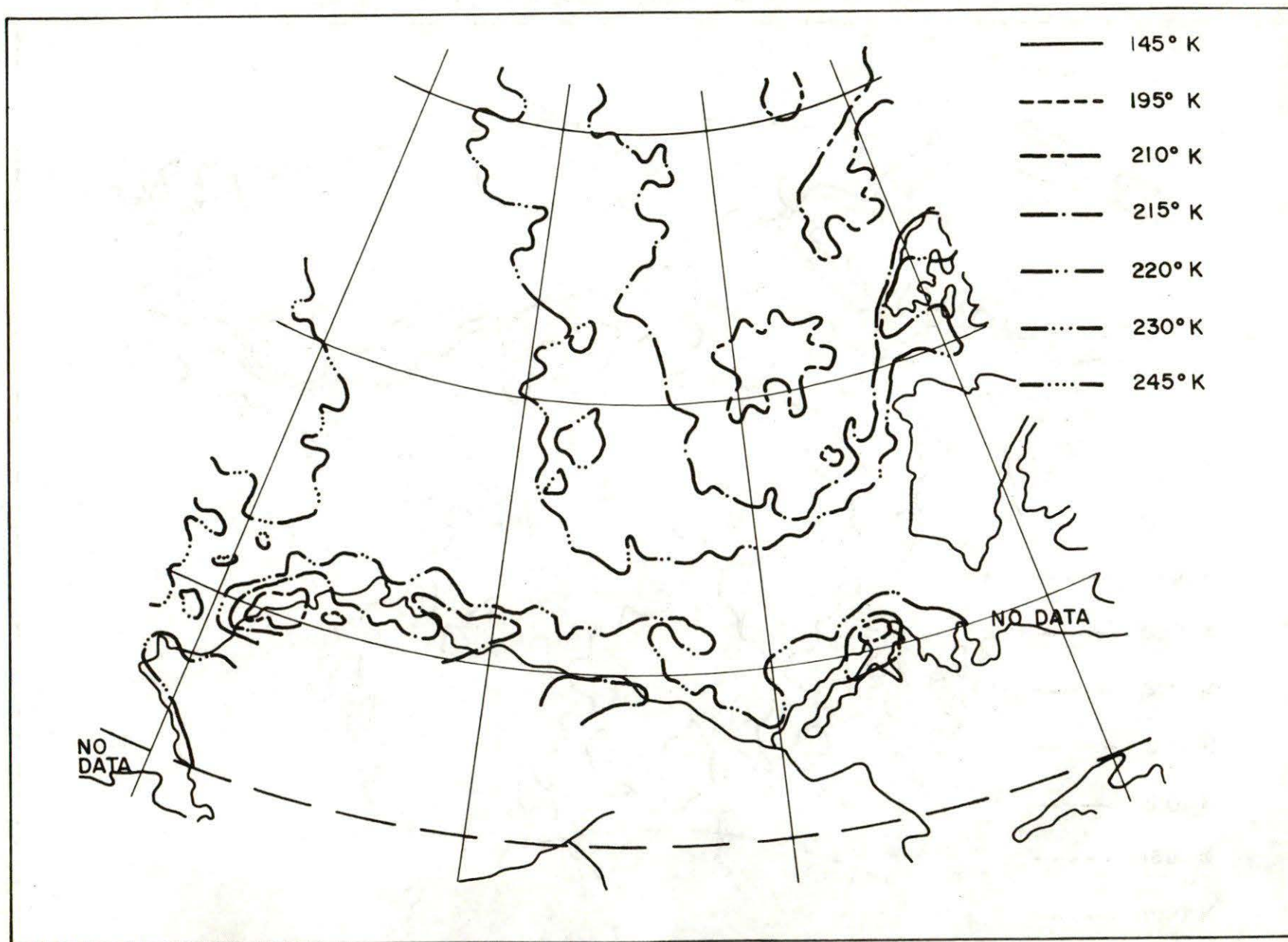


Figure A13. Monthly map of brightness temperature contours, March 1974.

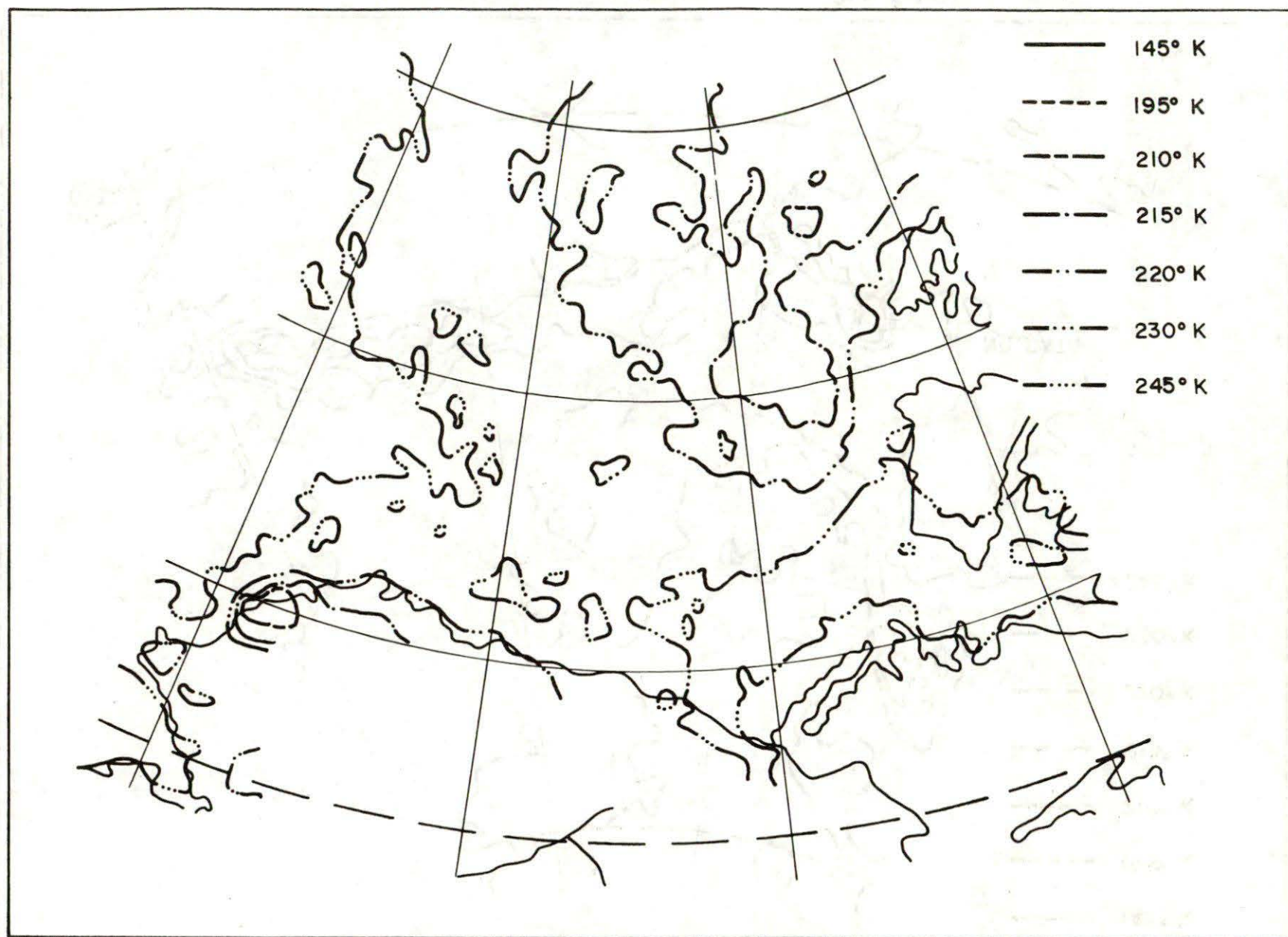


Figure A14. Monthly map of brightness temperature contours, April 1974.

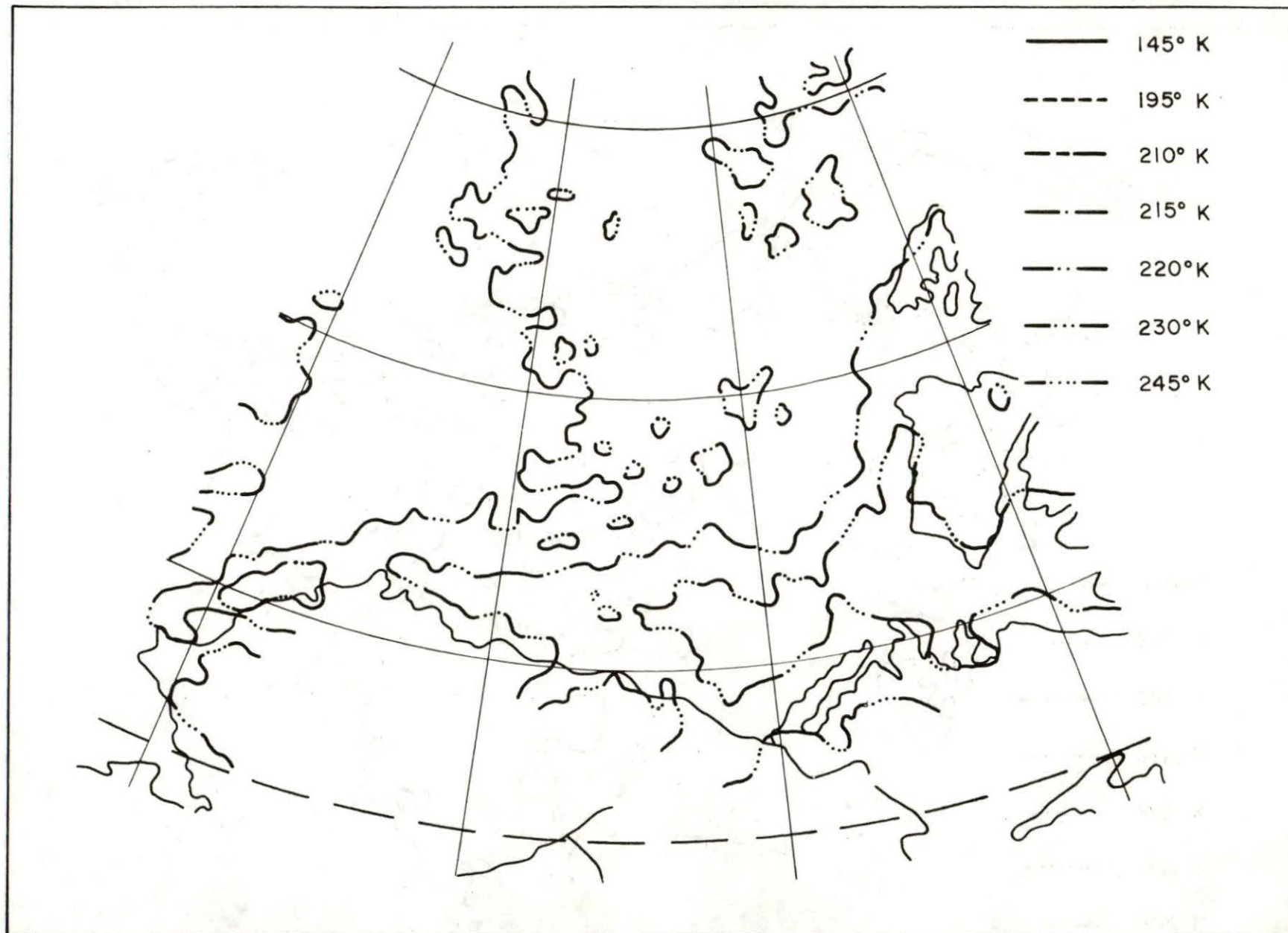


Figure A15. Monthly map of brightness temperature contours, May 1974.

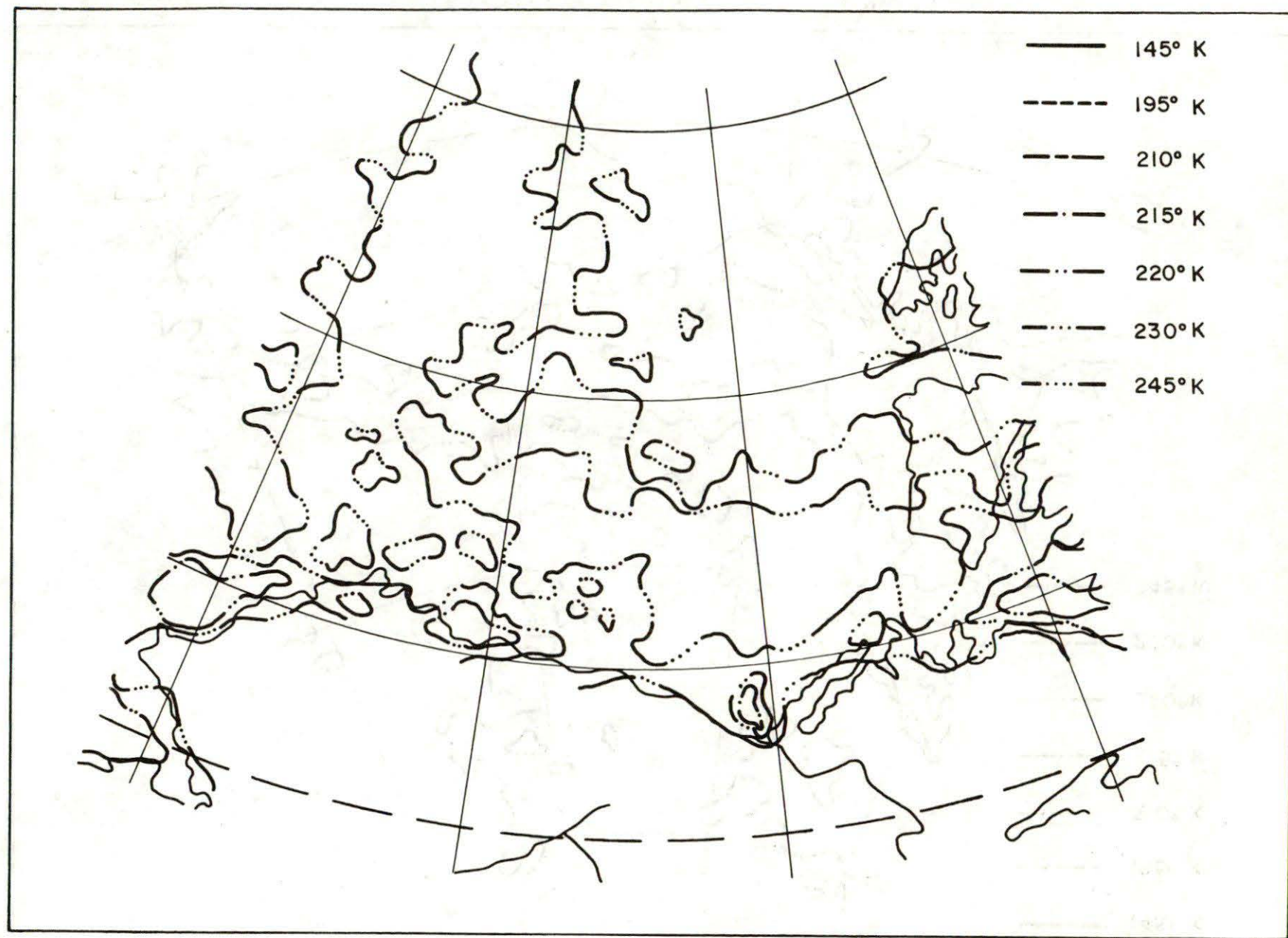


Figure A16. Monthly map of brightness temperature contours, June 1974.



Figure A17. Monthly map of brightness temperature contours, July 1974.

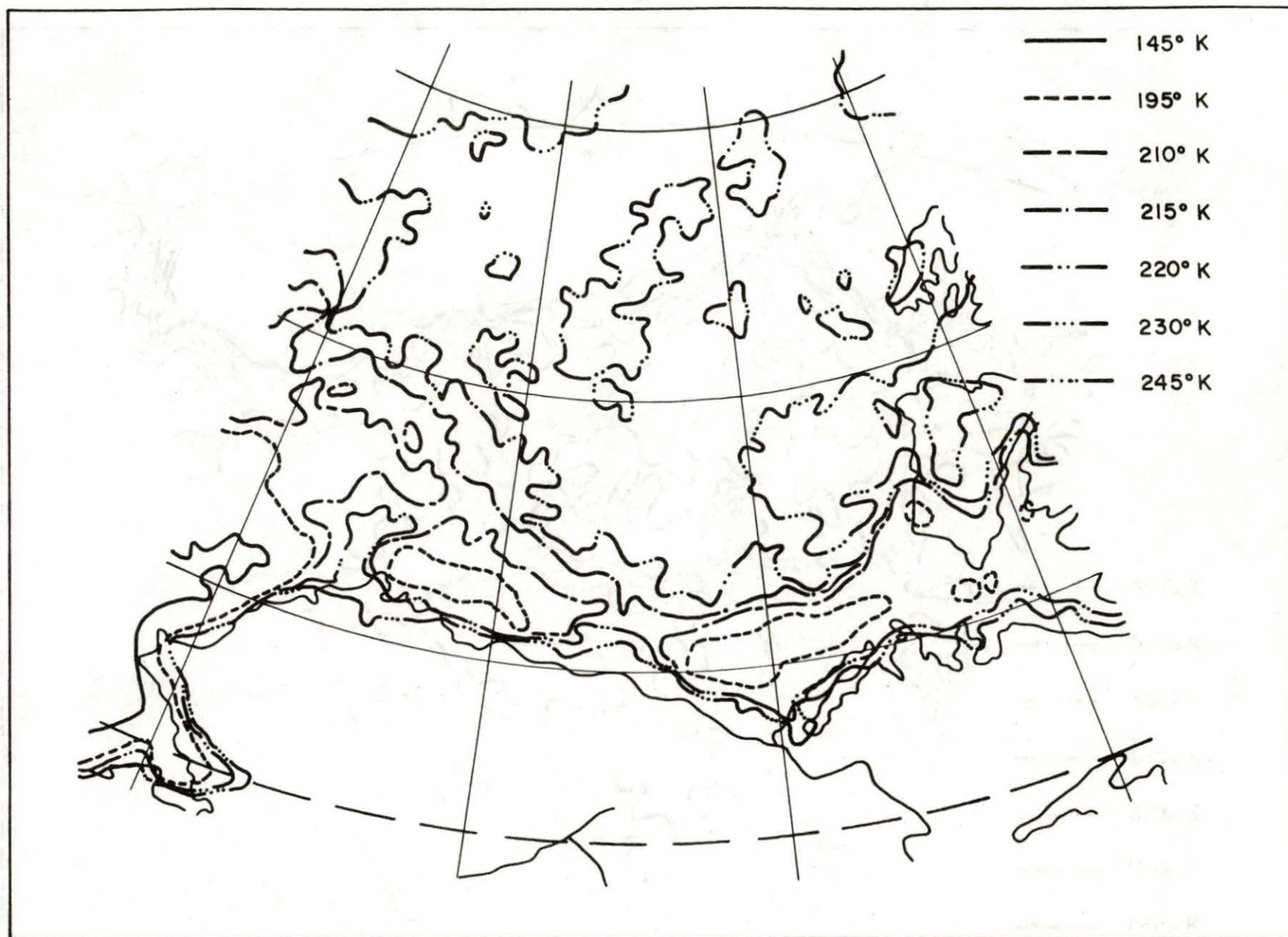


Figure A18. Monthly map of brightness temperature contours, August 1974.

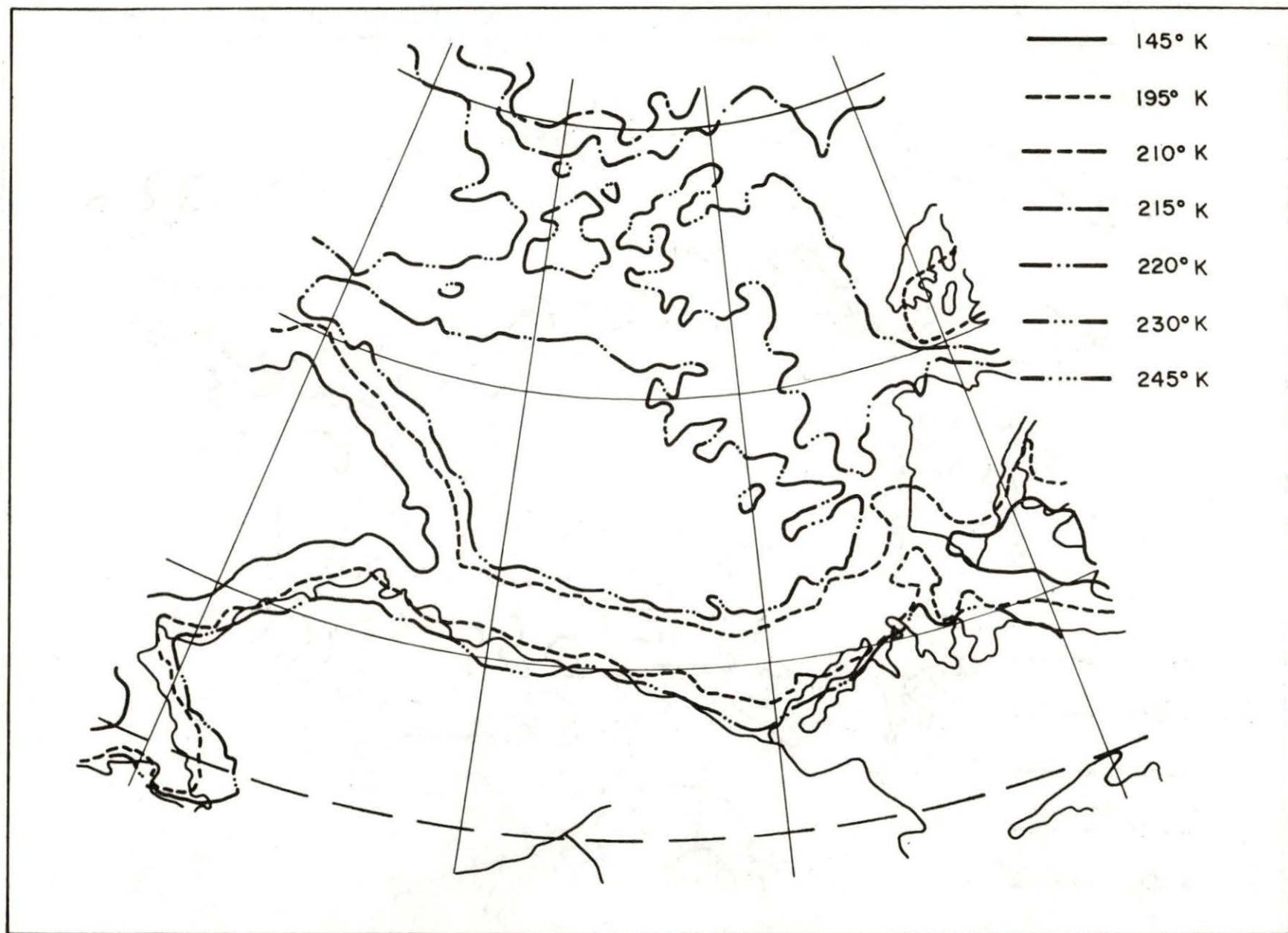


Figure A19. Monthly map of brightness temperature contours, September 1974.

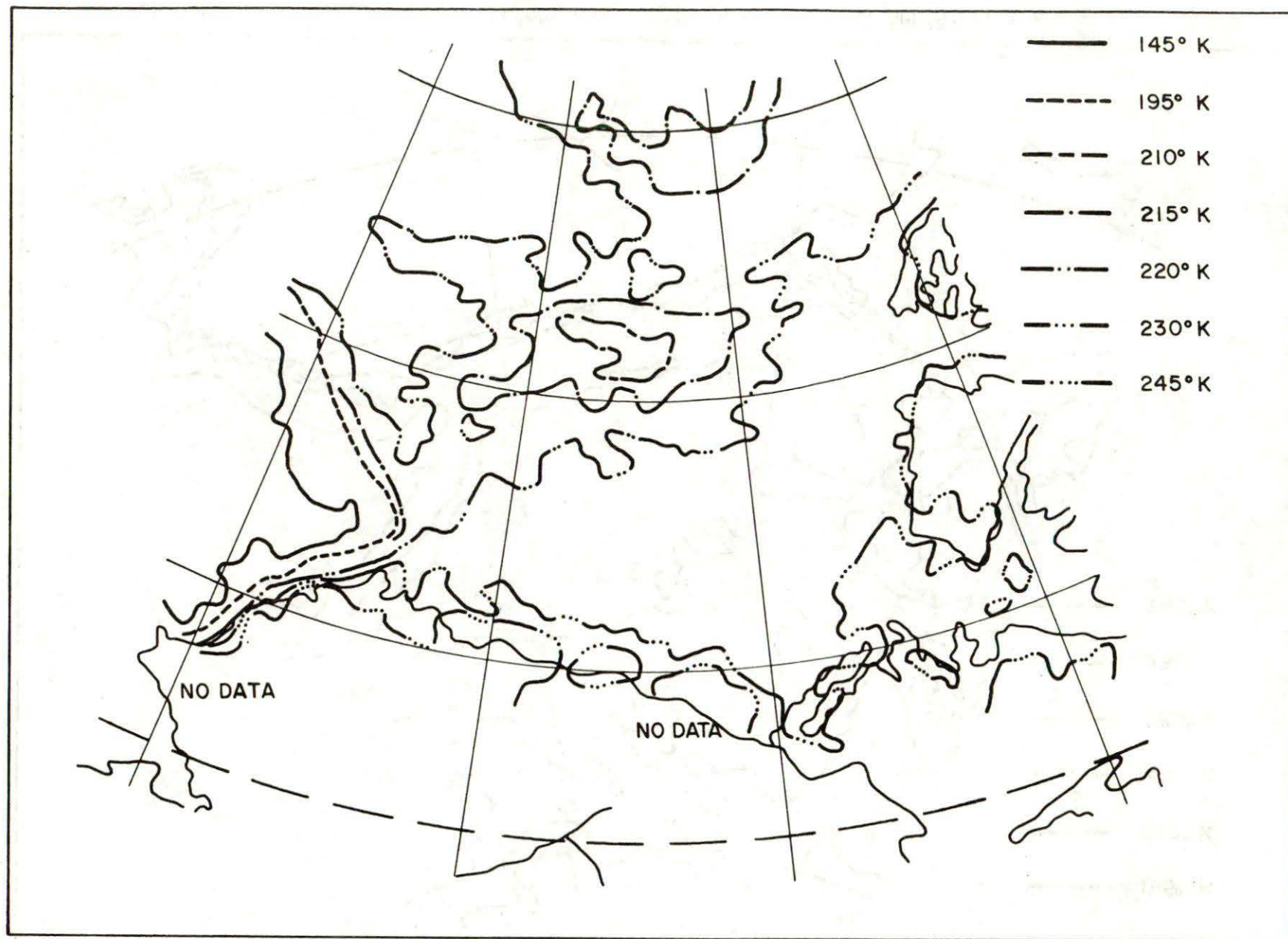


Figure A20. Monthly map of brightness temperature contours, October 1974.

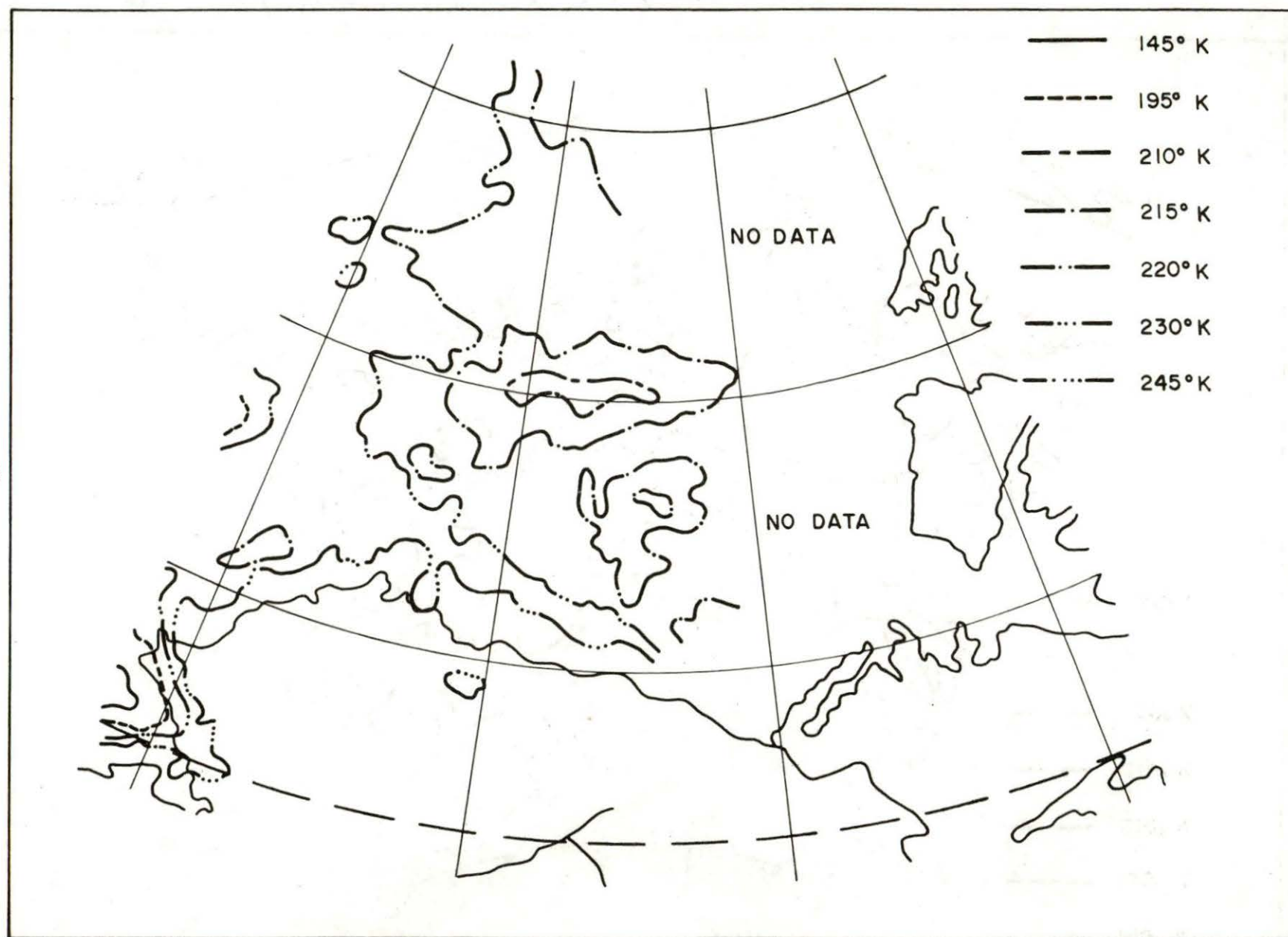


Figure A21. Monthly map of brightness temperature contours, November 1974.

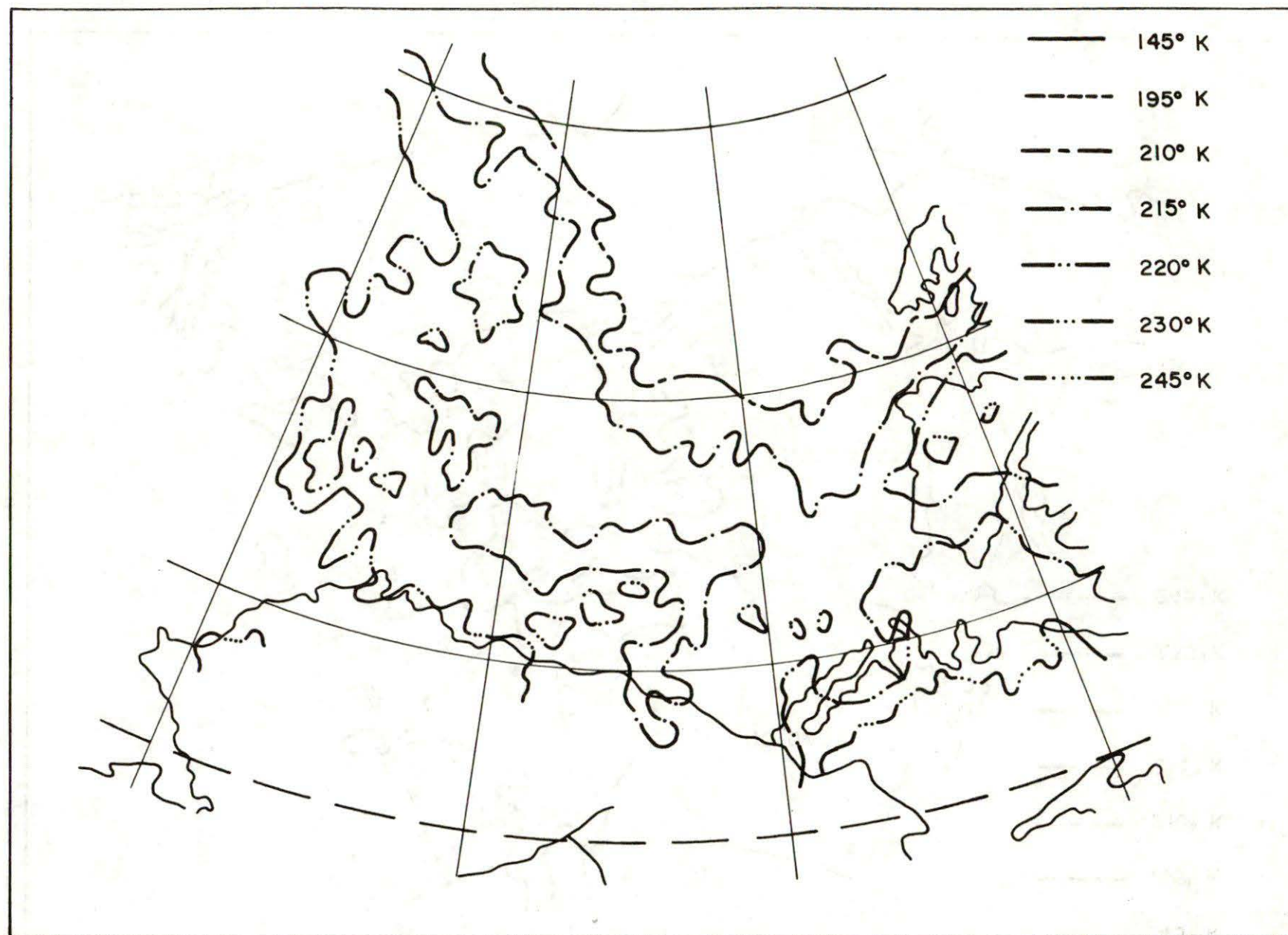


Figure A22. Monthly map of brightness temperature contours, December 1974.

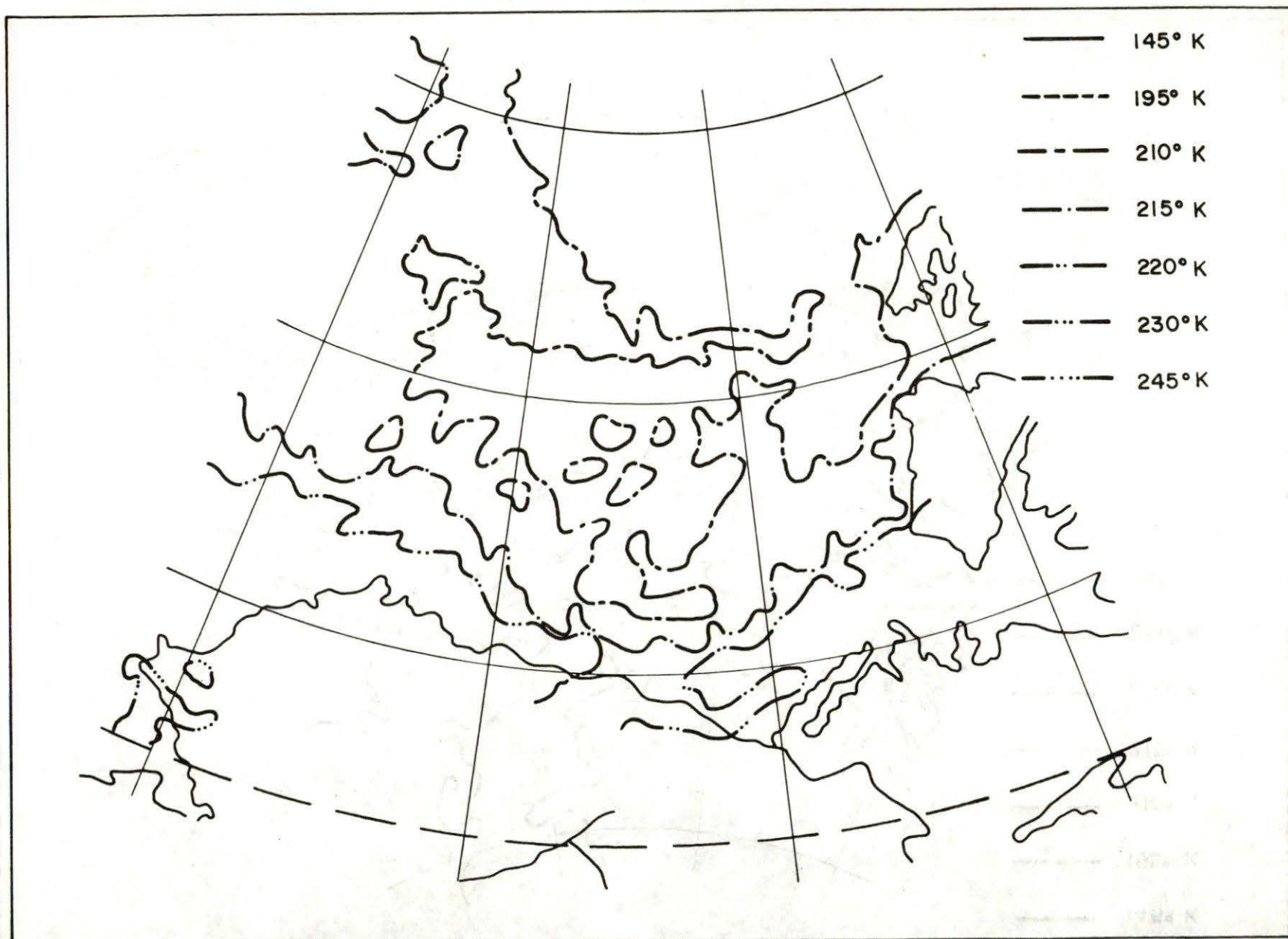


Figure A23. Monthly map of brightness temperature contours, January 1975.

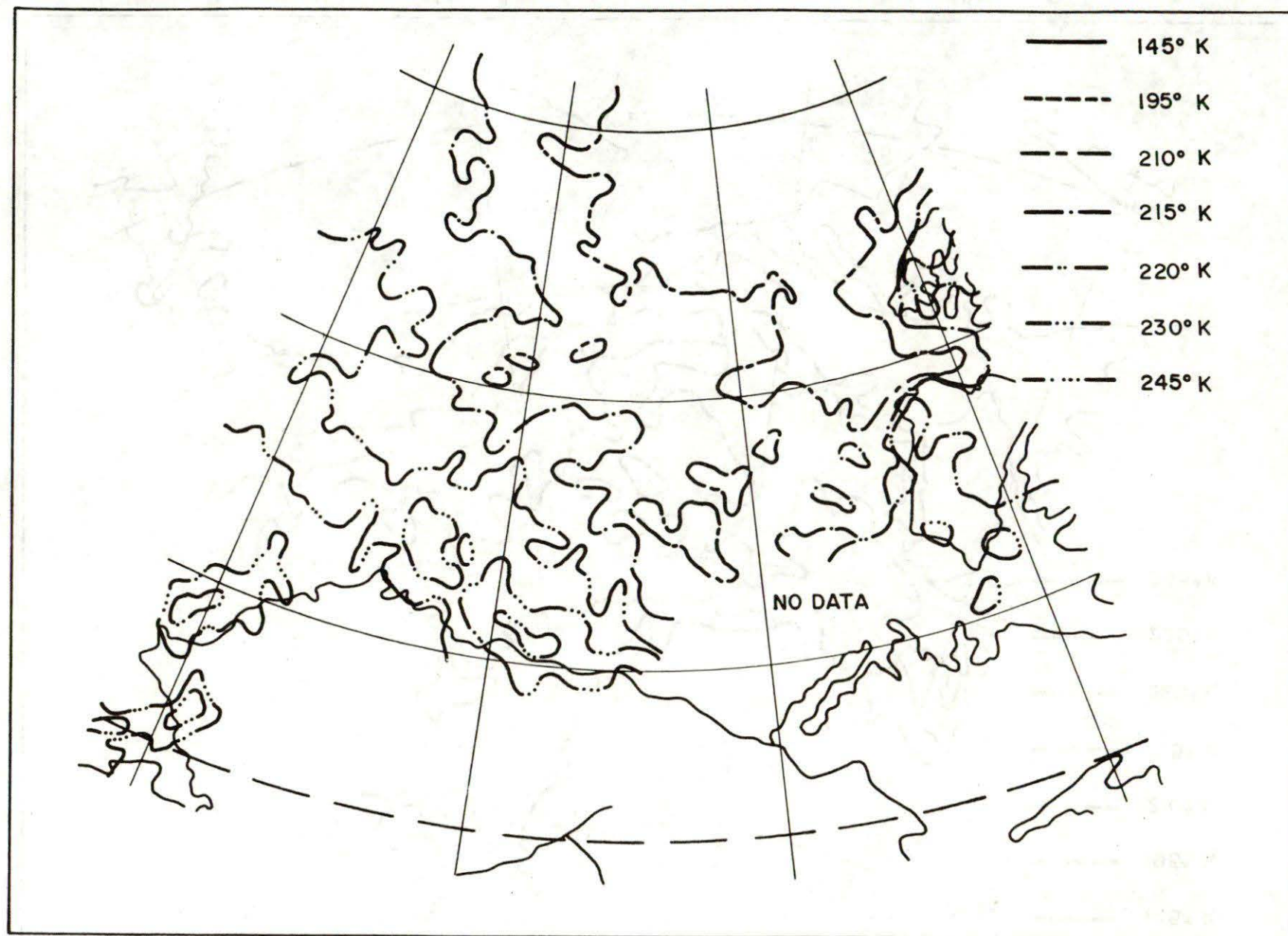


Figure A24. Monthly map of brightness temperature contours, February 1975.

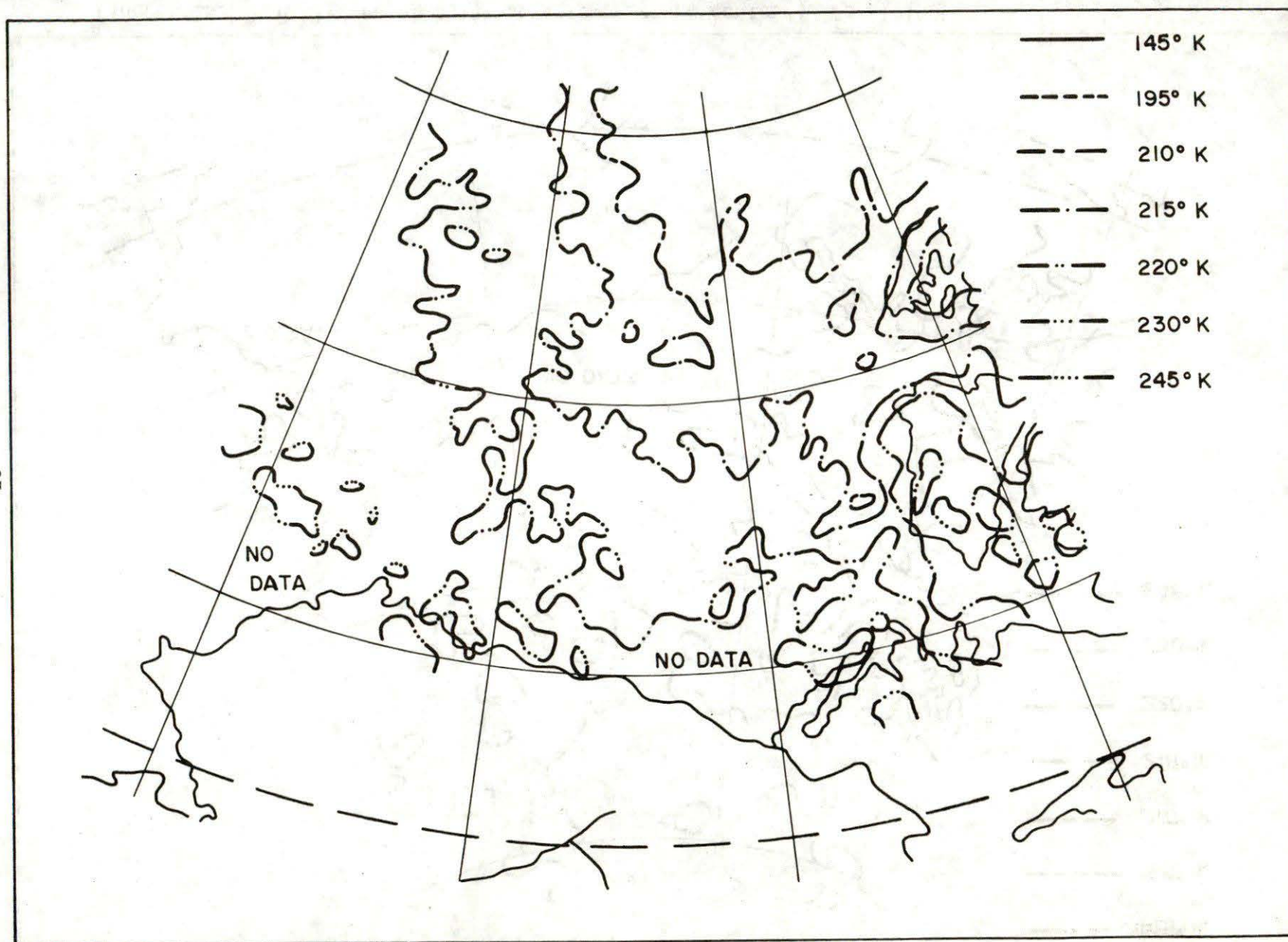


Figure A25. Monthly map of brightness temperature contours, March 1975.

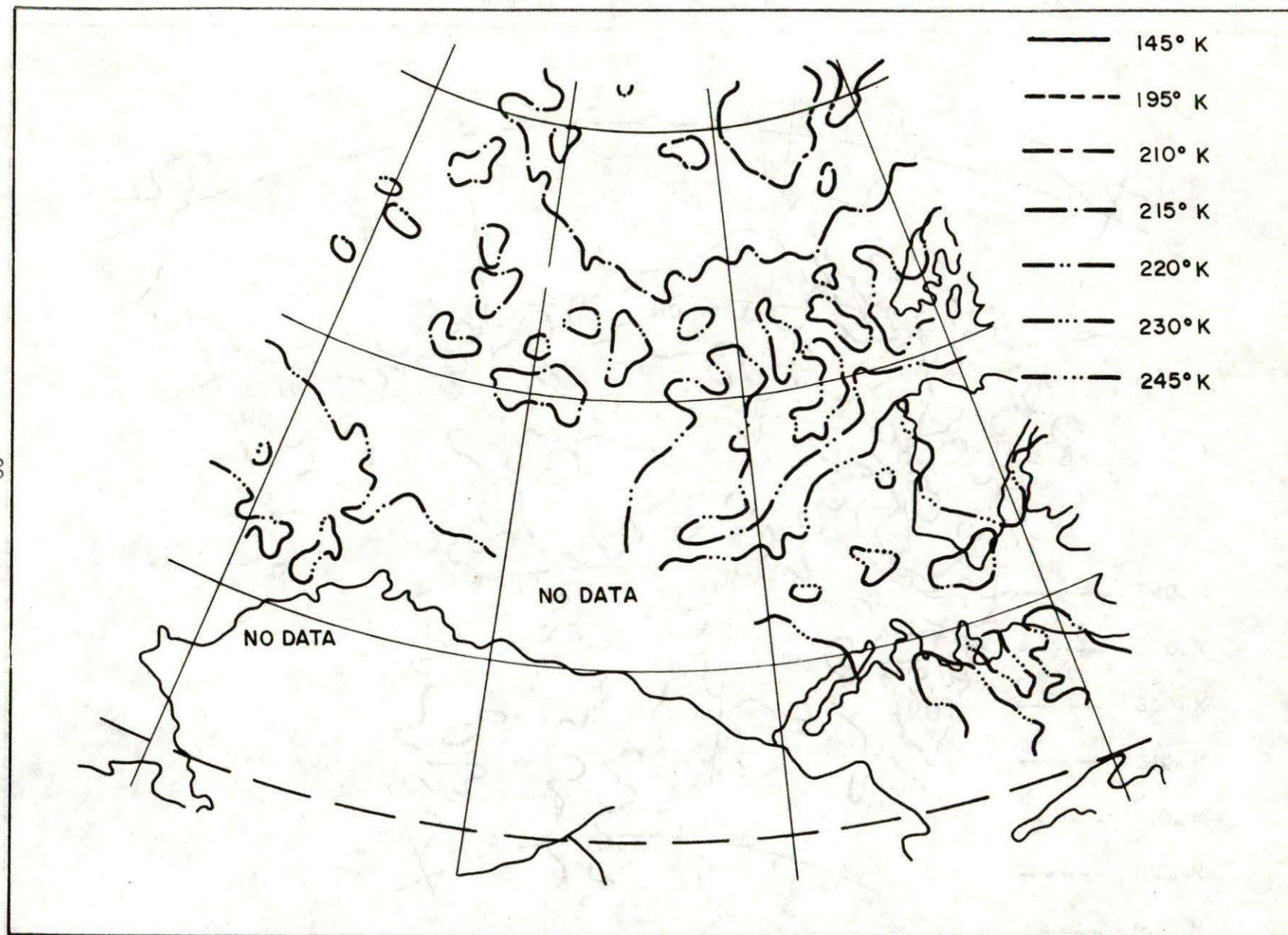


Figure A26. Monthly map of brightness temperature contours, April 1975.